

Lecture Notes in Offshore Pipeline Technology

Svein Sævik

25/4/2015

Preface

This lecture note was originally written during Spring 2011 to support lectures given in *Pipeline Technology*. These lectures were introduced first time in 2010 as part of the course *TMR 4120 Underwater Technology*, an introduction course meant for 3rd class students at the Department of Marine Technology, NTNU.

Later on, additional topics have been added related to finite element technology for slender marine structures and mechanical behaviour of flexible pipes to support lectures given in *TMR 4225 Marine Operations*, *TMR 4505 Advanced Structural Analysis of Marine Structures* and *TMR8208 Dynamic Analysis of Slender Structures*.

The author has 20 year experience in pipeline engineering covering most aspects of design analysis of slender structures including offshore steel pipelines and flexible riser systems.

Trondheim, April, 2015,

Svein Sævik

Contents

1	Introduction	7
1.1	General remarks	8
1.2	The design process	12
1.3	Engineering phases	14
1.3.1	Steel pipelines	14
1.3.2	Flexible pipes	15
2	Design principles	17
2.1	General remarks	18
2.2	Design formats	19
2.3	Discussion of loads of relevance for pipelines and flexibles	23
2.4	Discussion of failure modes	29
2.4.1	Mechanical failure modes for steel pipelines	29
2.4.2	Mechanical failure modes for flexible pipes	33
2.5	Cross-section design	35
3	Heat transfer and thermal insulation	37
3.1	General remarks	38
3.2	The heat transferr coefficient	39
3.2.1	Conduction	39
3.2.2	Convection	41
3.2.3	Influence of soil burial	41
3.3	The temperature profile	42
3.4	Time to reach critical temperature	42
4	Pipeline Design	47
4.1	General remarks	48
4.2	Stress and strain components	48
4.3	Wall thickness design	51
4.3.1	The hoop stress (bursting) criteria	51
4.3.2	External pressure collapse	51
4.4	Design against other relevant failure modes in steel pipelines	54
4.4.1	Buckling due to combined loads	54

4.4.2	Fatigue	55
4.4.3	Other mechanical failure modes	55
5	Material selection and welding	57
5.1	General remarks	58
5.2	Material selection	59
5.3	Pipeline welding	60
5.3.1	General	60
5.3.2	Welding processes	61
5.3.3	Non destructive testing	62
6	Pipeline installation	65
6.1	General remarks	66
6.2	Pipeline installation methods	66
6.2.1	Controlled Depth Tow Method	67
6.2.2	J-lay	67
6.2.3	S-lay	68
6.2.4	Selection of method	69
6.3	Pipeline installation analysis	70
6.3.1	The effective tension concept and Archimedes law	71
6.3.2	The catenary equation	76
6.3.3	Minimum horisontal radius	78
6.3.4	Residual radius and roll	79
7	Global buckling	85
7.1	General remarks	86
7.2	The process of buckling	86
7.3	Analytical global buckling model	88
8	Mechanical behaviour of flexible pipes	93
8.1	General remarks	94
8.2	Governing stress components	95
8.3	Wire geometries	98
8.4	Behaviour due to axisymmetric loads	100
8.4.1	General	100
8.4.2	Axial loading	101
8.4.3	Torsion	109
8.4.4	Internal and external pressure	110
8.5	Behaviour in bending	111
8.5.1	General	111
8.5.2	Minimum bend radius	112
8.5.3	Stresses and stress resultants related to the tensile armour	113
8.5.4	Stresses related to the pressure armour	120

8.6	Buckling	123
8.6.1	Collapse	123
8.6.2	Tensile armour buckling	127
9	Global finite element analysis	135
9.1	General	136
9.2	Basics of the finite element method	137
9.3	Non-linear effects	140
9.4	Strain and stress measures	142
9.5	Non-linear finite element methods	147
9.5.1	Equilibrium equation	147
9.5.2	Non-linear Finite Element Formulations	147
9.5.3	Material law - Plasticity for metals	149
9.5.4	Solution techniques	155
9.5.5	Example non-linear static analysis algorithm	161
9.6	Description of important finite elements for pipeline structural analysis	163
9.6.1	Pipe Elements	163
9.6.2	Seabed contact element	164
9.6.3	Roller contact element	166
9.6.4	3 Noded Pipe-In-Pipe Contact Element	169
9.7	The Pipeline Installation Case	172
9.7.1	General	172
9.7.2	Modelling	172
9.7.3	Example of results	174
10	References	175

Chapter 1

Introduction

1.1 General remarks

Offshore pipelines are used for oil and gas transport worldwide. Depending on application, pipelines can be classified into:

- *Export pipelines*, large diameter lines exporting processed oil and gas from the offshore installation to the onshore processing plant or to the market.
- *Flowlines*, small diameter lines transporting the unprocessed well flow from the well-head to the offshore processing plant.
- *Intra-field lines*, for transport between offshore installations.
- *Chemical injection lines*, providing anti-freeze and corrosion inhibitors that are injected into the pipeline/flowline wellstream to control hydrate (hydrocarbon crystallization) formation and corrosion.
- *Water injection lines*, for pumping water into the reservoir too keep the reservoir pressure and improve the production rate.
- *Bundles*, normally based on installing the flowline, umbilical and injection lines into one pipe cross-section, a *carrier* pipe that provides mechanical protection and installation buoyancy.

If not otherwise noted, the term *pipeline* may refer to all the above applications whereas the term *flexible* will refer to non-bonded flexible pipe cross-sections. Non-bonded flexible pipes cannot be manufactured for large diameters and is therefore mostly used in flowline and riser applications.

Many oil & gas field developments include an offshore platform to process the incoming fluid from the reservoir. Depending on the water depth, this may be either a fixed platform (up to about 300 m water depth) or floaters in the form of semi-submersibles or ship shaped vessels. An example is shown in Figure 1.1. In this case a satellite template is used to tie a distant well into the floater infrastructure by means of a flowline and a riser section. The flowline is installed separately and include flowline end terminations (FLET) at both ends. At the template the flowline is connected to the wellhead piping by a spool piece in steel or a flexible jumper (a short length of flexible pipe). At the floater end, the pipeline is connected to the floater by either a catenary riser or a wave configuration riser. In addition to the sagging section, the wave configuration includes a hogging section with buoyancy elements that gives more flexibility. This is to avoid dynamic compressive forces at the touch down point (TDP) as a result of the vessel motions. Depending on water depth and environmental conditions, the latter requires compliant flexible risers to allow the motion envelope of the floater without over-stressing the pipe in bending. The flexibility requirement depends on the motion amplitude versus the water depth. Therefore, steel catenary risers or steel wave configuration risers might become an alternative at large water depths. Under North Sea conditions, the flexible riser would be the only alternative at 300

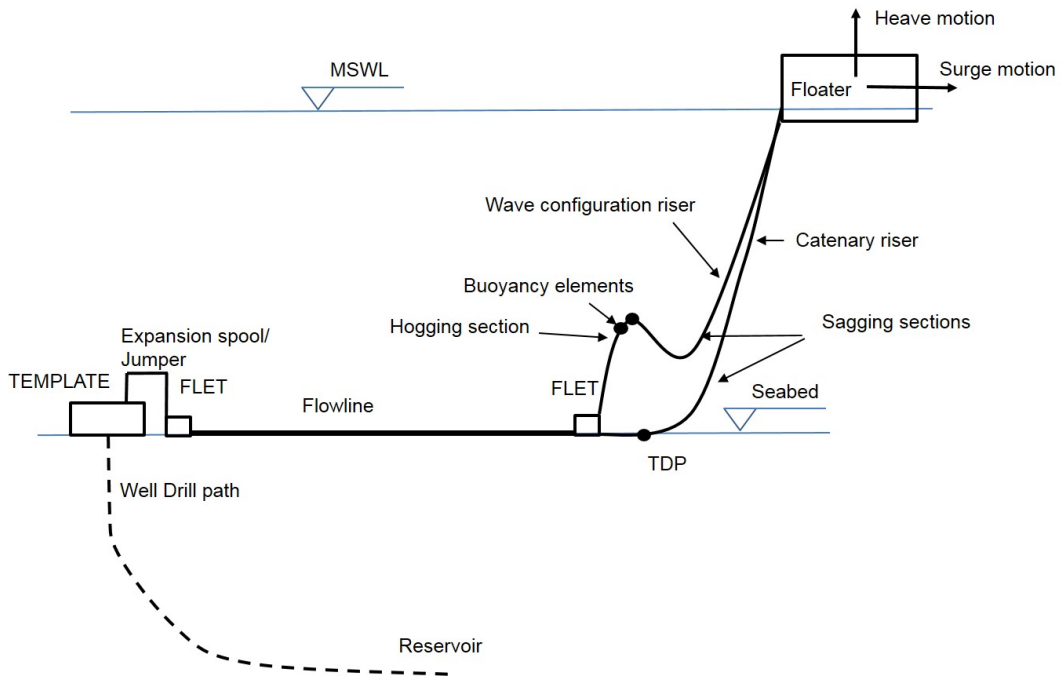


Figure 1.1: Example field lay-out with flowline and riser

m water depth. However, at a water depth of 1300 m as applicable for the AAsta-Hansteen field, steel wave configuration risers may be applied [Subsea7, 2013]. In the Gulf of Mexico, the environmental conditions are somewhat calmer as compared to North Sea conditions and several field developments use steel catenary risers at more shallow waters, e.g the Auger field at 872 m water depth [Phifer et al., 1994].

In order to control the template infrastructure (e.g. valves, instrumentation etc.) electrical and hydraulic power as well as signal transmission between the well template infrastructure and platform are needed. This is provided by umbilicals that may include power conductors, hydraulic tubing and fibre-optic cables. A typical umbilical cross-section is seen in Figure 1.2.

Steel pipelines are preferably made of carbon steel alloys that provides a favourable strength-cost ratio. However, the un-processed well flow may contain corrosive gases such as CO_2 or H_2S . The latter is a problem specially for old reservoirs where water injection is used to maintain the reservoir pressure and the production rate where H_2S may be developed due to bacterial activity. The presence of both gases in the well flow may either require corrosion resistant alloys to be used, chemical injection or a combination of both to control the corrosion process. The corrosion resistant alloys are normally based on increasing the chrome content in the steel matrix. In simple terms, the more chrome, the more corrosion resistance, however to a significant increased material cost. Therefore, in order to provide cost efficient transport over long distances, low cost carbon steels is favourable. This requires that the corrosive gases are either removed prior to export or



Figure 1.2: Typical umbilical cross-section [MARINTEK, 2009b]

neutralised by chemicals by application of a separate injection line.

The non-bonded flexible pipe is manufactured by layers of steel and plastic that are allowed to slide relative to each other. Each layer has its specific function and a typical *rough bore* flexible pipe consists of (starting from the inside), see Figure 8.1:

- The carcass which consists of a flat steel strip, formed into a corrugated profile preventing collapse induced by external pressure, installation loads and gases in the annulus. The carcass is not leak tight and it therefore does not contribute to resisting internal pressure. The pipe is normally installed in empty condition, exposed to the full external pressure, and it is noted that the carcass design is based on assuming that the annulus between the outer sheath and the pressure bore is water filled (damage in the outer sheath), implying that the full water pressure must be sustained by the carcass alone. The other layers may contribute in terms of providing some support, however, depending on the magnitude of gap formation between the carcass and the other layers.
- The Pressure Barrier, providing a pressure tight barrier between the internal content and the external water
- The Pressure Spiral, providing support of the pressure barrier, resisting the internal pressure and also supporting the carcass with respect to resisting external pressure. The pressure spiral wire may consist of 1-2 wires in 1-2 layers with a lay angle α close to 90° relative to the pipe's longitudinal axis.
- The tensile armour, providing strength with respect to tension, torque and the pressure end-cap force. Normally two cross-wound layers are applied to ensure torsion balance, each layer consisting of 30-80 rectangular steel wires with a lay angle α in the range $+/- 29^\circ - +/- 55^\circ$. A positive lay angle is taken to be according to the



Figure 1.3: Flexible pipe cross-section

right hand rule. The layers are normally separated by anti-wear layers to avoid metal contact and possible wear and fretting wear. The fraction filled ratio is about 0.9 (Layer steel area versus layer total area)

- The external sheath, designed to avoid sea water ingress and sea water corrosion.

The carcass is made of a corrosion resistant alloy whereas the steel layers outside the pressure barrier that are protected from direct contact with the well flow are normally made of higher strength carbon steels with less corrosion resistance.

It is noted that the pressure barrier is not 100 % leak tight in the sense that gases from the pipe bore will leak to the tensile armour annulus. Then the annulus pressure may build up over time and burst the outer sheath. Therefore the end fittings are equipped with vent valves to provide gas drainage.

For flowlines, the internal pressures may be very high depending on the reservoir characteristic. Depending on the water content of the well flow, hydrates may be formed, an ice-like crystalline solid consisting of a mixture of water and natural gas. The crystallization temperature of hydrate increases with pressure, and may be significantly higher than the environmental (*ambient*) sea water temperature (typically 25°C versus ambient temperature 5°C). This represents a major challenge, since the need for maintenance of the processing machinery at the offshore installations require shutting down the production at certain intervals. Hence, the temperature inside the pipe annulus will start to drop and hydrate plugs blocking the well flow may be formed. To avoid such blocking, there are several principles in use, such as:

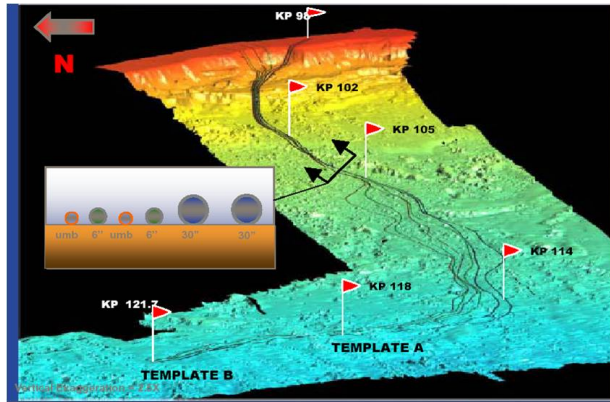


Figure 1.4: The Ormen Lange Field [MARINTEK, 2009a]

- To remove the water by subsea processing.
- To ensure that the critical hydrate formation temperature is never reached by insulating the pipe or by active heating.
- To reduce the freezing temperature by chemical injection via a separate injection line pumping chemicals into the flowline.

Which solution to be applied, requires consideration of many factors such as diameter, critical temperature, well flow rate, line length and costs.

As an example, for the Ormen Lange Gas field outside the Northwest Coast of Norway, chemical injection containing both corrosion and anti-freeze inhibitors is used to control the flow and corrosion in the two 80 km long 30" gas carbon steel pipelines transporting the flow from the subsea template located at 850 m water depth to the onshore processing plant at Nyhamna. At Nyhamna, the water and corrosive gases are removed and the inhibitors recycled. Thereafter, the gas is exported to Easington in UK by means of a 42" 970 km long export pipeline. No floaters were included in this field development and it represented a step change in technology as it was the first time unprocessed gas flow was transported over such long distances.

In the Ormen Lange case, each 30" field pipeline is followed by one umbilical and one chemical injection line as illustrated in Figure 1.4.

1.2 The design process

From the above it is clear that the pipeline design process is a multi-disciplinary process that requires a variety of engineering skills and knowledge including:

- Thermodynamics and reservoir technology

- Material technology
- Cartography
- Geotechnics
- Coastal engineering
- Oceanography/Hydrodynamics
- Structural mechanics

The basic pipeline design boundary condition is governed by thermodynamics and reservoir characteristic. A given mixture of fluid or gas is to be transported at a certain rate and at a given pressure and temperature from point A to point B . The pressure and temperature conditions provide input to the structural design requirements, whereas the chemical and thermodynamic characteristics govern which material to be used and which operation philosophy to be applied. The latter is a major challenge for flowlines due to the fore mentioned possible presence of water and corrosive gases in the well flow.

The tendency of oil and gas exploitation into deeper waters is followed by deeper reservoirs that are characterised by high temperatures and pressures. High temperatures will speed up the corrosion process, and a lot of effort has been spent to develop alloys that can handle this challenge at a reasonable cost. The life-cycle costs are governed by a combination of material costs and the operation costs of chemical injection to control both corrosion and hydrate formation. Less corrosion resistant material means lower material costs but higher injection costs. High temperatures also reduces the strength in the materials, to a variable extent depending on the applied alloy. In many cases, the more corrosion resistant material, the more temperature sensibility in yield stress is noted. This again requires more heavy pipe walls to carry the internal pressure for some alloys. Hence, the material selection is a result of an optimisation process that need to be carried out in close cooperation with other disciplines.

In order to avoid sea water corrosion, a combination of coating and cathodic protection (CP) is normally applied. For steel pipelines, the latter is provided by anodes that are attached to the pipe at regular intervals. These need to be integrated with due consideration of the external anti-corrosion coating design and installation issues (the installation vessel includes tensioners and roller boxes to support the pipe that may crush the anodes). For flexible pipes, the anodes are placed at the end terminations and an external sheath used to protect against sea water ingress and corrosion.

Steel pipelines are welded together from typically 12 m long pipe joints. Due to possible defects resulting from the weld process, the moment capacity of the pipe cross-section at the weld may be reduced and this must be taken into account when evaluating both installation and operation loads. Close cooperation between the structural design and material disciplines is therefore needed.

The pipeline needs to be installed safely on the seabed by application of an installation vessel. This requires detailed maps showing the seabed topography. The available level of

detail prior to the engineering is normally not sufficient and may need to be supplied by separate survey campaigns along the alternative pipeline routes. Depending on the seabed terrain, the predefined route may include curves to avoid terrain irregularities and obstacles in the form of ship wrecks etc. During both installation and operation, the pipeline will further be exposed to hydrodynamic loads from current and waves. Depending on the temperature and pressure conditions, the pipeline will start to move relative to the seabed due to thermal elongation. The structural response due to these effects are governed by pipe-soil interaction, which requires soil mechanics expertise supplied by survey data along the pipeline route.

Coastal engineering gives input in terms of models for describing the local current conditions which together with oceanography and metocean data gives input to the hydrodynamic load models.

The design process need to ensure that the pipeline can resist all loads throughout both installation and operation phases. This needs to be documented by structural analysis which is challenging since non-linearities from loads, material, pipe-soil interaction, boundary conditions and geometry need to be included.

From the above it is clear that pipeline design requires a high level of engineering skills from a wide range of disciplines.

1.3 Engineering phases

1.3.1 Steel pipelines

The steel pipeline engineering process is normally divided into three phases:

- Conceptual engineering.
- Pre-engineering.
- Detail engineering.

The primary objectives of the conceptual engineering phase is to investigate technical feasibility, identify constraints that need further investigation and allow basic cost and schedule investigations of different technical solutions to be performed.

In the pre-engineering phase, the pipeline concept and design issues are fixed. This includes selection of material, pipeline diameter and wall thickness. The selected solution is documented against relevant standards throughout out all phases of the pipeline design life. In some cases this also includes material take off (*MTO*) sufficient to order linepipe. The *MTO* is a table describing how many meters of each pipe dimension in terms of diameter and wall thickness that is needed. When calculating the necessary length of pipe, the 3D pipe route must be considered. In addition some spare pipe length is normally included to enable pipe repair due to e.g. installation failure.

In the detail engineering phase, the design is developed to provide all necessary technical documentation that is needed for procurement and construction tendering. The design activities includes:

- Route optimization considering pipeline length and the number and length of possible free spanning sections (in the case of irregular seabed).
- Selection of pipe wall thickness and coating.
- Check ultimate strength for different critical load scenarios during installation and operation.
- Check fatigue strength of free-spans due to hydrodynamic loads and optimize the amount of intervention work (e.g. by installing rock supports along the free-span) needed to limit the free span length.
- Prepare *Alignment sheets*. This is a drawing containing all relevant information that is needed by the lay contractor to install the pipeline, including detailed route data, coordinate values of each pipe segment, the pipe joints to be applied (different section may require different wall and coating thicknesses). Such info is normally given as a function of *KP* (kilometer point), representing the curvilinear length coordinate along the map projection plane (this only include the XY coordinates not the Z coordinate and in irregular terrains the amount of pipe needed will be larger than that calculated from the *KP*).
- Prepare all detailed drawings needed for the sub-sea work scope such as expansion spools, pipeline crossings, free-span corrections, risers, subsea structures etc.
- All necessary specifications, for materials and construction activities (welding, sub-sea tie-ins, riser installations, survey, sub-sea structures) and commissioning (i.e. flooding, pigging, hydrotest, cleaning and drying).
- Prepare detailed material take off (*MTO*).
- Prepare design data and other information needed for the certification authorities. This also includes systems for pipe-tracking so that all necessary data that relates to every single pipe joint and weld is stored in a data base. Each weld is non-destructive tested (*NDT*) by radiography or ultrasonic imaging. The image of each weld is stored as part of the data base. Then in the case of unplanned events in the operation phase, all data that is needed to evaluate the pipeline's strength can be recovered.

1.3.2 Flexible pipes

With reference to [API, 2008a], design of flexible pipes is also carried out in stages:

- Material selection considering the temperature and chemical conditions in terms of pH (sweet or sour service).
- Cross-section configuration design based on what to be transported (gas, oil, water) and at which pressure rating.
- System configuration design based on the surrounding infrastructure and environment.
- Riser dynamic analysis design, identifying the curvature and tension extreme responses.
- Detail and service life design verifying that sufficient service life is obtained.
- Installation design, ensuring that the pipe can be safely installed.

Chapter 2

Design principles

2.1 General remarks

In the following, the design principles applied for pipelines and unbonded flexible pipes are discussed. This includes definition of basic concepts such as:

- Characteristic load conditions and associated load effects.
- Definition of limit states as basis for design during relevant load conditions.
- Design formats as applied in [DNVGL, 2012] and [API, 2008b] for capacity checks against relevant failure modes.

Pipelines and risers are exposed to a variety of loads during the installation and operating conditions. Using [DNVGL, 2012] as a reference, these can be classified into:

- Functional loads
- Interference loads
- Accidental loads
- Environmental loads

Functional loads include all loads that result from the physical existence of the pipeline system and its intended use throughout all phases of the design life including construction, storage, installation and operation. This includes weight, loads from installation equipment or other components, soil reactions, static hydrodynamic forces, internal/external pressure and temperature. It is noted that soil reactions may result from a variety of effects such as permafrost and ice scouring in Arctic areas or due to reservoir drainage over the operation lifetime causing the seabed to move relative to the pipeline.

Typical interference loads include trawl interference from fishing gear hitting the pipeline, pipeline anchor hooking, vessel impacts and dropped objects. Dropped objects is of special importance close to the platform infrastructure due to crane activities. In [DNVGL, 2012] this is handled by the concept of safety classes leading to more stringent design criteria in the high risk zones. This may result in mechanical protection requirements for the pipeline section close to the platform. According to the same standard, interference loads can be classified as accidental loads if the annual probability of experiencing such loads are $< 10^{-2}$. The probability of anchor hooking is in many cases less than this and is therefore normally classified as an accidental load.

Environmental loads are defined as loads on the pipeline that are caused by the surrounding environment. This includes both wind and hydrodynamic loads where the latter are defined as flow-induced loads caused by the relative motion between the pipe and the surrounding water.

Pipelines and flexibles will be exposed to two main phases during it's design life: the construction/installation and the operation phases. The characteristic loads to be used for design purposes are obtained by considering the time duration of exposure to the above

loads during the different phases. Since environmental loads are stochastic by nature, the responses will also be stochastic. Statistical methods are therefore used to first define characteristic load conditions. These are then used as basis for global response analyses, see [Larsen et al., 2014], to find the characteristic load effects as basis for capacity checks of relevant failure modes (e.g. the bending moment at a given cross-section versus moment capacity). For pipelines and risers, the hydrodynamic loads include steady current and wave induced loads, each described statistically with a probability distribution. In the design standards, the characteristic load condition to be applied for the different phases is therefore defined by specifying combinations of return periods for the combined action of current and waves. An extensive treatment of stochastic dynamics and related issues is found in [Naess and Moan, 2013].

The capacity checks are to be carried out for all relevant phases and with reference to the concept of limit states. In [DNVGL, 2012] the limit states are:

- Servicability Limit State (SLS), A condition which exceeded renders the pipe unsuitable for operation without necessary causing a leak. For a pipeline, cross-section ovalisation will result from bending. If the ovalisation makes it impossible to carry out planned cleaning by sending cylindrical plugs through the pipeline system (PIG) , then the servicability limit state criterion is exceeded.
- Ultimate Limit State (ULS), A condition which, if exceeded, compromises the integrity of the pipeline.
- Fatigue Limit State (FLS), An ULS condition accounting for accumulated cyclic load effects.
- Accidental Limit State (ALS), An ULS due to accidental (in-frequent) loads.

Realising that both the characteristic load effects and the failure mode capacities (resistances) are statistical quantities with inherent uncertainties, each limit state is formulated by means of a design format that include limit state specific safety factors to ensure that the failure probability is acceptable. This is illustrated in Figure 2.1 showing the probability density functions for load $p(L)$ and the resistance $p(R)$. The red area governs the probability of failure. This can then be adjusted by including reduction factors for the resistance, moving $p(R)$ to the left and/or applying load factors moving $p(L)$ to the right. The final design criteria will then be obtained by first defining the target failure probability (the red area) and then associate factors to reduce the capacity and/or increasing the load to capture the inherent uncertainties.

2.2 Design formats

In relevant standards for design of steel pipelines and flexible pipes there are two different design formats in use: These are:

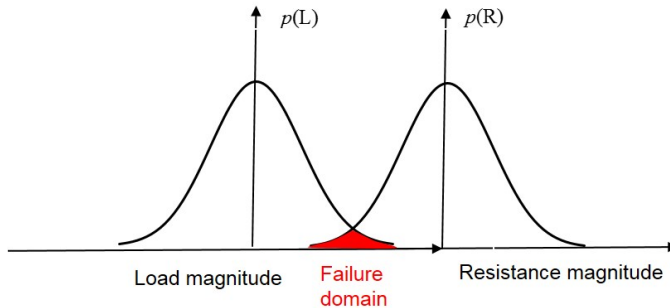


Figure 2.1: Probability density functions representing the magnitudes of load and resistances

- Load Factored Resistance Design (*LRFD*)
- Allowable Stress Design (*ASD*)

The LRFD design principle is applied in the pipeline standard DNV-OS-F101 [DNVGL, 2012], whereas ASD was applied in the previous DnV pipeline standard [DNV, 1982] and in the flexible pipe standard [API, 2008b]. The *LRFD* format applied in [DNVGL, 2012] is formulated as:

$$L_F\gamma_F + L_E\gamma_E + L_I\gamma_I + L_A\gamma_A \leq \frac{R_c}{\gamma_m\gamma_{SC}} \quad (2.1)$$

where L_i and γ_i are the characteristic *load effects* and associated load factors respectively for Functional (F), Environmental (E), Interference (e.g. fishing gear) (I) and Accidental (A) loads. R_c is the characteristic resistance, γ_m is the material factor whereas γ_{SC} represents a factor considering the safety class. Different safety classes would apply for pipeline sections near human activities as compared to the remaining pipeline. The *load effect* may e.g. represent the applied bending moment at the most critical cross-section and R_c in that case represents the characteristic bending moment capacity. As noted, factors are applied on both the load and resistance sides. These are calibrated to obtain a target safety level that depends on the application.

To perform the calibration, the inherent uncertainties in both the load and resistance need to be described. This also includes the model uncertainty contained in the chosen format itself. For example, the format used to describe failure from interaction between axial force, bending moment and external pressure would include formulas that depend on parameters such as Young's modulus, diameter, thickness, yield stress and ultimate stress. Then the model uncertainty needs to be established by comparing the equation format results to those obtained by laboratory tests and/or FE analysis, see e.g. [Bai et al., 1997], considering same load conditions and by variation of the same parameters. Having described the design format statistically, the safety factor calibration

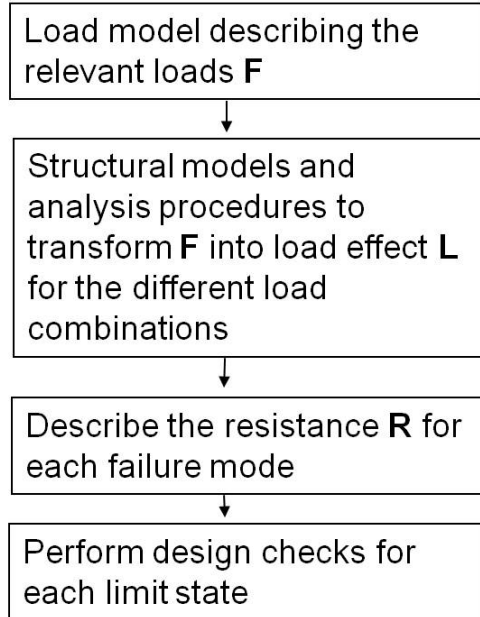


Figure 2.2: LRFD design procedure

is done based on principles from structural reliability analysis by e.g. by the First Order Reliability Method (FORM), Second Order Reliability Method (SORM) or Monte Carlo simulations, see [Melcher, 1987], [Madsen et al., 1986], [Christensen and Baker, 1982] and [Naess et al., 2009].

The LRFD based design procedure for steel pipelines is illustrated in Figure 2.2. Each limit state is described by a design equation describing each failure mode and with predefined load and resistance factors.

The *ASD* format is typically formulated in terms of stresses as:

$$\sigma \leq \eta \sigma_y \quad (2.2)$$

where σ_y is the yield stress and η is an utilization factor. Here the safety factor is applied on the resistance side only. The difference between them is illustrated in Figure 2.3, considering Euler buckling of a pinned beam exposed to the axial force L_0 . If L_0 gives $\sigma_0 < \eta \sigma_y$ then the ASD criterion will be fulfilled. By applying the LRFD format on the other hand, the structural analysis needs to include the safety factor γ on the load side. Hence, Euler buckling would take place, resulting in exceeding the allowable stress. This would not be picked up by the ASD format. In cases where the relation between load and response is non-linear (as for Euler buckling), the LRFD format is best suited.

For structures where a linear relation can be assumed between load and response, the formats can be calibrated to obtain similar safety levels. Flexible pipes are compliant structures where the design procedure has traditionally been based on the ASD approach, see [API, 2008b]. This assumes that the relation between stress and global response quantities

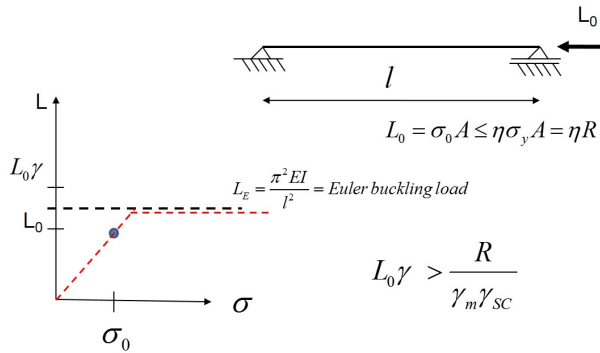


Figure 2.3: LRFD and ASD design principles applied to beam Euler buckling

can be considered linear with respect to limit state stress checks. Due to the compliant nature of the flexible pipe this is considered valid until a critical curvature is exceeded. Therefore, [API, 2008b] defines utilisation factors for both stresses and global curvature.

For steel pipelines plastic strains are allowed to occur, however, the allowable strain will depend on whether the relation between load and response is *force controlled* or *displacement controlled*. The two different scenarios are illustrated in Figure 2.4. The pinned beam is made of an ideal elastic-plastic steel material, resulting in a non-linear moment - external load characteristic. The load is increased until the proportionality limit of the steel is reached (The elastic part of the material curve) and thereafter the material starts to yield with a subsequent drop in the beam moment resistance against further loading. This is followed by an associated rapid increase in strain and deformation. However, if it can be proven that the deformation can be stopped before the allowable strain is reached, the load condition is defined to be *displacement controlled*. Such a condition can be obtained by installing e.g. a support at the midpoint, stopping further deformation as indicated in the figure. However, if this cannot be proved, the load condition is defined to be *force controlled*. For the displacement controlled case, some plastic straining can be allowed as long as other possible failure modes are avoided. The design criteria may then be expressed by strains (*strain based design*). In the force controlled case, the design criteria is expressed in terms of stresses or stress resultants (*stress based design*), only utilising a certain fraction of the ultimate capacity enforcing the response to occur in the elastic domain, thus avoiding infinite displacement and failure.

A typical strain based design case will be installation of the pipeline by application of the reel method where the pipes are plastically bent to a fixed radius. Then the response do not rely on the applied load but on the applied reel radius.

A typical force controlled design case will be a pipeline free span on an irregular seabed. The bending moment at the shoulders will depend on the weight, tension, span length, the local geometry of the seabed and the soil conditions. However, it is not possible within reasonable confidence to rely on the seabed geometry with respect to limiting the pipeline's local strain response. Therefore this case will normally be treated as a load controlled

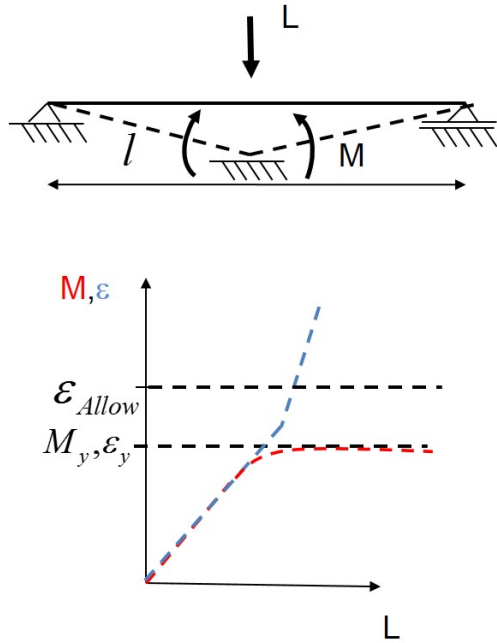


Figure 2.4: Displacement and Load controlled conditions

situation.

2.3 Discussion of loads of relevance for pipelines and flexibles

Serving as an example to discuss the loads of relevance to slender structures with one section resting on the seabed and another hanging into the sea, Figure 2.5 shows a pipeline during the installation phase by application of the S-lay method. The pipe is installed in empty condition and has a submerged weight per length of pipe w_s with an associated dry weight per length w_p . The weight of the pipe is carried by the vessel by means of a tensioner that provides tension throughout the length of the suspended section. The pipe configuration can be divided into the *sagbend* section curving upwards and the *overbend* section curving downwards. The latter is obtained by the vessel stinger, a curved steel structure having a constant radius of curvature, providing a smooth transition from the horizontal position on the vessel until the pipe enters into the water. Along the stinger, the pipe is supported by roller boxes that serve to minimize friction forces between the pipe and the stinger, thus allowing the the pipe string to slide into the sea as the vessel is moving forward. The rollers will cause reaction forces that will introduce local bending moments and stresses in the pipe wall that have to be considered in the design of the installation phase. Local stresses will also occur in the section supported by the tensioner machine that

keeps the weight of the pipe by means of a hydraulic squeeze force and friction. For deep water pipes the weight of the suspended section and the required squeeze force becomes large possibly causing collapse of the pipe cross-section. This is specially critical during flexible pipe deep water installations.

During S-lay, the net horizontal force provided by the vessel is the sum of the applied tension T at the vessel and the horizontal reaction forces from the stinger (which is opposite directed). Hence the net horizontal force applied to the pipe is T_0 as illustrated in the figure. At the seabed touch down point, localized soil reactions will occur, depending on the pipes bending stiffness and the vertical soil stiffness. Wave induced vessel motions will cause relative rotations and displacements between the suspended section and the end fixations represented by the vessel and seabed. This will introduce cyclic bending moments that can cause both fatigue and local buckling failures. At the seabed cyclic compressive axial forces may occur in addition due to the combination of vertical vessel motions and the seabed constraint. This in combination with external pressure may cause local buckling and collapse of the cross-section to occur.

The seabed is irregular and a pipeline free-span results as illustrated in the figure. Then the pipeline will act as a bridge with maximum bending moments at the span shoulders that will depend on the span length, tension, weight, bending stiffness and the end conditions in terms of soil geometry and stiffness. As long as the bottom tension and the water depth is kept constant, no relative displacements between the pipe and the soil will occur during continued pipelay. By further assuming that the free-span is sufficiently long away from the ends so that the bottom tension is fully anchored by axial friction, the free-span will rest in a pre-stressed reference configuration characterized by the bottom tension T_0 as applied during installation. During the operating phase, the weight increases as the pipe is filled with fluid. In addition, the operating pressure and temperature will cause pipe elongation, however, as this is constrained by mobilization of axial soil friction forces at the ends, a compressive force will result. This may cause the global configuration to change possibly by global buckling with associated pipe-soil relative displacements and forces.

During installation, the suspended section will be exposed to hydrodynamic loads introduced both by direct current and wave action as well as vessel motions resulting from hydrodynamic and wind forces.

With respect to the direct hydrodynamic lateral transverse line load component, this is commonly formulated by means of the Morison equation [Morison et al., 1950]. Consider a horizontal cylinder representative for a free spanning pipeline, see Figure 2.6. Then by assuming no seabed boundary effects, the Morison equation can be formulated as:

$$q_y = (C_M - 1)\rho_w A_e (\dot{v} - \ddot{r}) + \rho_w A_e \dot{v} + \frac{1}{2}\rho_w C_D D |v - \dot{r}|(v - \dot{r}) \quad (2.3)$$

where C_M is the added mass coefficient, ρ_w is the water density, A_e is the pipe external area, \dot{v} is the horizontal wave induced water particle acceleration in the lateral direction, \ddot{r} is the associated acceleration of the cylinder, C_D is the drag coefficient, v is the water particle velocity including both contributions from the steady current and the wave $v = v_c + v_w$ and \dot{r} is the structure velocity. The two first terms is related to inertia effects whereas the

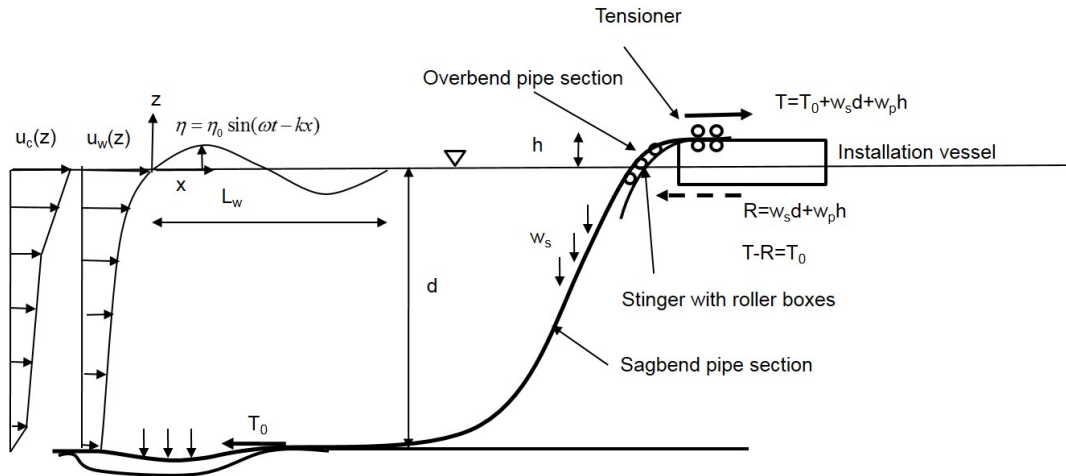


Figure 2.5: S-lay pipe configuration in static equilibrium

last is related to viscous effects proportional to the square of the velocity.

When it comes to the wave kinematics, linear (1st order) wave theory is normally applied. This relies on the assumption of:

- The water is incompressible and the density is constant in time and space
- The motion of the water particle is rotation free so there exist a scalar potential function from which the velocity components can be derived by differentiation
- There is no motion through the sea floor at $z = -d$.
- One water particle that initially was positioned at the free surface will remain so.
- The wave elevation is small (compared to wave length)
- The pressure on the free surface is constant and equal to the atmospheric pressure formulated on a linearised form by neglecting higher order terms.

The last assumption means that higher order terms are omitted. The role of these terms manifest themselves in terms of difference and sum frequencies. For floating structures, where free surface inertia effects dominates, the differential frequencies would introduce wave drift forces whereas the sum frequencies may contribute to high frequent resonance effects in e.g. tethered tension leg platforms, see [Faltinsen, 1990]. However, for slender structures such effects can be neglected in most cases..

The solution takes form in terms of harmonic functions for wave induced particle velocity, acceleration as well as dynamic pressure. Taking the deep water assumption, i.e. $d \rightarrow \infty$ with reference to Figure 2.6 (a), the quantities of relevance to Eq. 2.3 are given by [Faltinsen, 1990]:

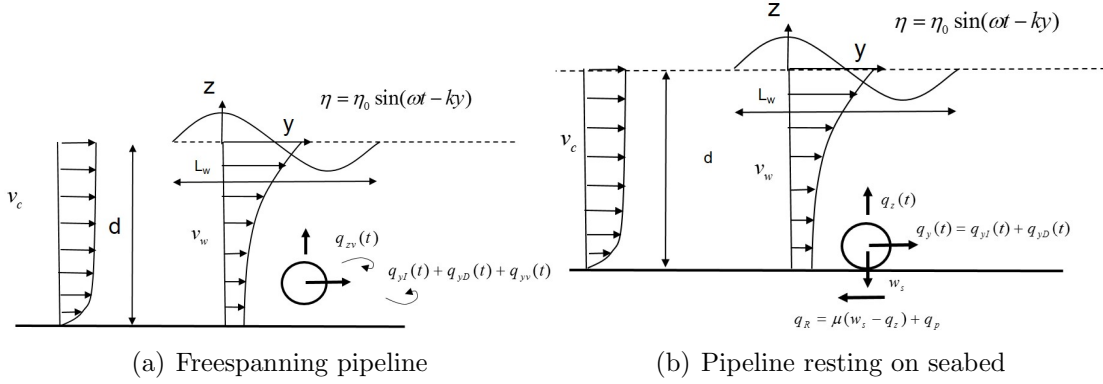


Figure 2.6: Hydrodynamic forces of a pipeline exposed to transverse current and wave kinematics for the freespanning and on-bottom cases

$$v_w = \omega \eta_0 e^{kz} \sin(\omega t - ky) \quad (2.4)$$

$$\dot{v} = \omega^2 \eta_0 e^{kz} \cos(\omega t - ky) \quad (2.5)$$

$$k = \frac{2\pi}{L_w} = \frac{\omega^2}{g} \quad (2.6)$$

$$p_d = \rho_w g \eta_0 e^{kz} \sin(\omega t - ky) \quad (2.7)$$

where k is the wave number and $\omega = \frac{2\pi}{T_w}$ is the wave frequency determined by the wave period T_w and p_d is the dynamic pressure. Considering the exponential decay as a function of water depth, and the dispersion relation between the wave period and length L_w it becomes clear that the wave induced terms in the Morison equation will not be of importance for pipelines resting on the seabed at deeper waters than about 200 m.

By integrating the dynamic pressure in Eq. 2.7 around the circumference of a virtual cylinder that moves with the water particles with outer radius r , assuming that the cylinder diameter is small compared to wave length, and taking a positive value as a force that acts along the y -axis in Figure 2.7 the instant horizontal force q_y can be obtained as:

$$\begin{aligned} q_y &= 2\rho_w g \eta_0 \int_0^\pi e^{k(z-r \sin \psi)} \sin(\omega t - kr \cos \psi) r \cos \psi d\psi \\ &\simeq 2\rho_w g \eta_0 e^{kz} \int_0^\pi [\sin \omega t - \cos \omega t k r \cos \psi] r \cos \psi d\psi \\ &= 2\rho_w g \eta_0 e^{kz} \int_0^\pi [r \sin \omega t \cos \psi - kr^2 \cos \omega t \cos \psi] d\psi \\ &= \rho_w \pi r^2 g k \eta_0 e^{kz} \cos \omega t = \rho_w \pi r^2 \omega^2 \eta_0 e^{kz} \cos \omega t \\ &= \rho_w A_e \dot{v} \end{aligned} \quad (2.8)$$

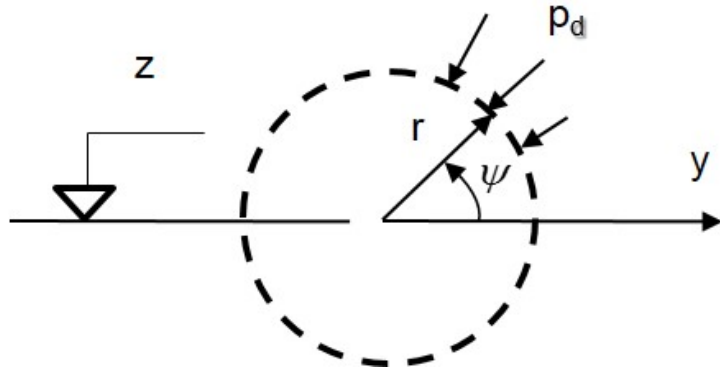


Figure 2.7: The Froude-Krylov effect

This corresponds to the second term in Eq. 2.3 which is known as the Froude-Krylov force, i.e. the force needed to keep the virtual cylinder moving according to the periodic orbital path of the contained water particles, according to Newton's second law. For a fixed cylinder, the structural acceleration becomes zero and then the inertia part of Eq. 2.3 becomes:

$$q_y = C_M \rho_w A_e \dot{v} \quad (2.9)$$

By the assumption of rotation free particle motion, the superposition principle applies and the force on the fixed cylinder can be obtained by adding an opposite potential resulting in $C_M = 2$

However, in the real case the assumption of rotation free particle motion is generally not valid. This a result of cylinder surface friction and water viscosity creating a shear layer with associated shear stresses that act to trigger water particle separation and wake formation behind the cylinder, see [Sumer and Fredsoe, 2006]. This behaviour is associated with shedding of vortices, see Figure 2.6 (a), the pattern depending on several factors such as the *Reynold's number* defined by:

$$Re = \frac{Dv}{\nu_w} \quad (2.10)$$

where D is the diameter of the cylinder v is the current velocity and ν_w is the kinematic viscosity of water.

The boundary layer and shedding of vortices is accompanied with a time varying shift of the pressure distribution along the cylinder surface giving rise to mean drag and high frequent in-line and lift forces. Further, when the frequency of vortex shedding is synchronised with e.g. the eigenfrequency of a pipeline freespan, Vortex Induced Vibrations (VIV) may occur, possible leading to fatigue failure.

As a consequence of the above, the C_M and C_D values to be used in Eq. 2.3 will represent a best fit time average that will vary depending on several factors such as:

- *Reynold's number* as defined above

- Roughness number = k/D (k = characteristic cross-sectional dimension of the roughness of the cylinder surface)
- Keulegan-Carpenter number, KC ($KC = \frac{v_w T_w}{D} = \frac{2\eta_0 \pi e^{kz}}{D}$ expressing the distance travelled by the water particle over one period relative to the diameter)
- Relative current number = v_c/v_w (assuming that they are both in the same direction)
- The gap ratio = e/D (see Figure 2.6 (a))

An extensive treatment of the influence of the above factors on C_M and C_D and the fluctuating vortex induced components is found in [Sumer and Fredsoe, 2006]. In terms of the consequences with regard to pipeline design, it is noted that when the gap ratio approaches zero as illustrated in Figure 2.6 (b), the vortex generation is mostly stopped. Instead there will be a lift force due to the enforced particle motion changing the pressure profile around the cylinder. Depending on the relative current number, the flow pattern becomes complex and cannot be described by a Morison model with constant coefficients. Therefore more advanced hydrodynamic models have been developed for on-bottom stability analysis [Sotberg et al., 1994] considering horizontal equilibrium between the hydrodynamic forces and the available soil resistance in terms of Coulomb friction and passive earth pressure resistance q_p , see Figure 2.6 and [DNVGL, 2010a].

When it comes to the high frequent forces due to vortex shedding, these can occur both due to constant current and wave induced current, the latter being dependent on the KC. The larger KC-number, the larger number of vortices can be shed during one cycle.

The vortex shedding frequency is determined by the Strouhal number St defined as:

$$St = St(Re, k/D) = \frac{f_v D}{v} \quad (2.11)$$

where f_v is the vortex shedding frequency. For the relevant range of Reynold's number and roughness a typical St value is 0.2. That means that for a riser experiencing sheared current (variable current versus depth), several eigen-frequencies may be triggered contributing to VIV. For pipeline free-spanning problems, the boundary layer related to steady current may cause the velocity to vary along the free-span causing more than one frequency to contribute due to the same effect.

For pipelines, the onset of VIV is commonly defined by means of the *Reduced velocity* parameter, see [DNVGL, 2006a], defined as:

$$v_R = \frac{v}{f_i D} \quad (2.12)$$

where f_i is the eigenfrequency of the span. In-line vibration occurs at the smallest velocities, however, the amplitude is smaller than for cross-flow vibrations due to lift forces, leading to smaller stress amplitudes. However, for a given probability distribution of the current velocity, the exposure time to in-line vibrations becomes larger. Therefore, in-line vibrations may give larger contribution to fatigue. This is illustrated in Figure 2.8 which also illustrates the effect of reducing the span length in terms of increasing the eigen-frequency, thus moving the on-set velocity to the right.

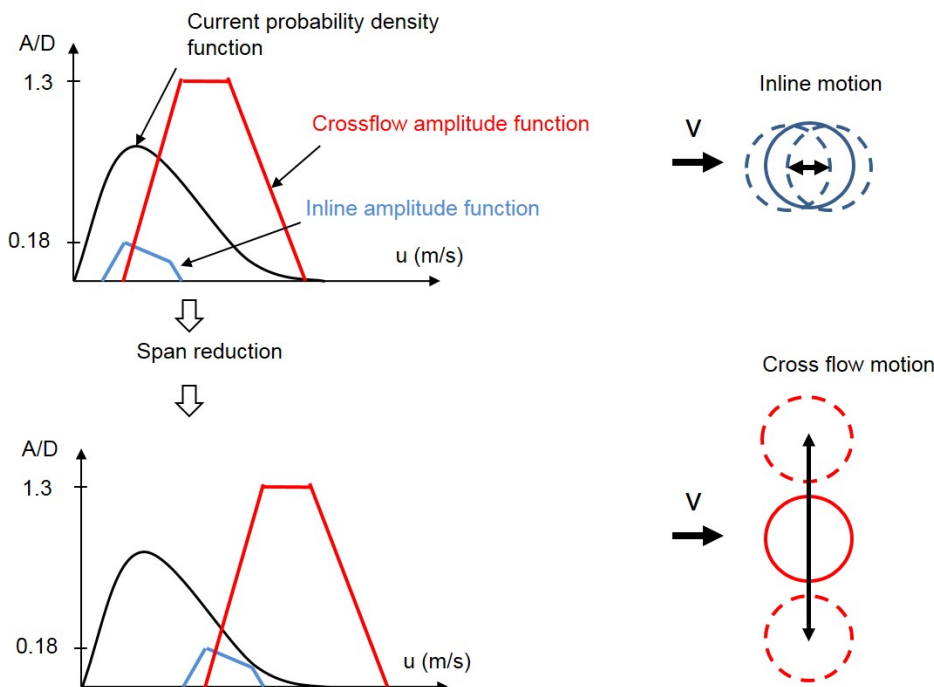


Figure 2.8: The onset of in-line and cross-flow VIV versus current probability density function

2.4 Discussion of failure modes

2.4.1 Mechanical failure modes for steel pipelines

The pipeline including riser sections needs to be designed to ensure robust and safe operation throughout its lifetime. This includes avoiding flow failure by wax blocking (typically due to hydrocarbons clogging to the pipe wall in oil pipelines) or hydrate formation (typically for flowlines with unprocessed flow including water and natural gas) and corrosion failure due to internal or external corrosion.

With respect to structural failure, important failure modes are [DNVGL, 2012]:

- Excessive yielding.
- Local buckling due to bending and pressure.
- Buckle propagation.
- Impact load denting.
- Ovalization.
- Fracture.

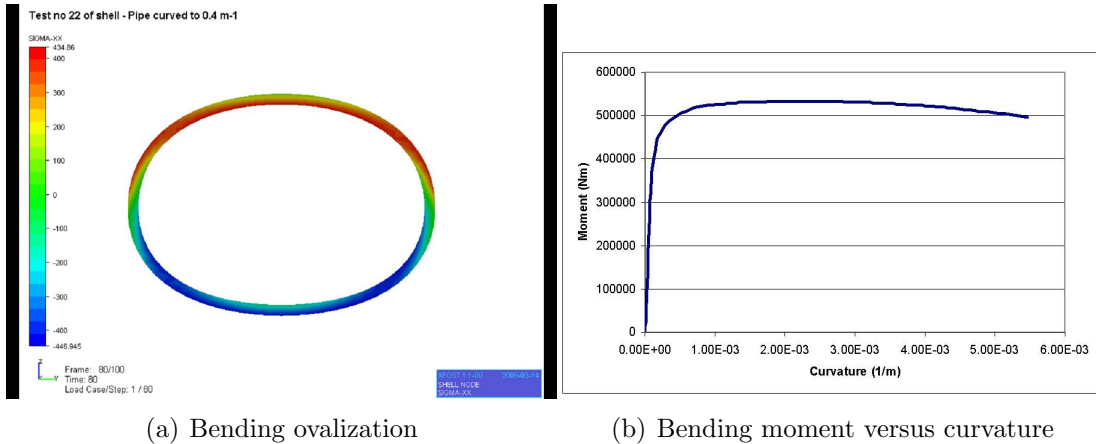


Figure 2.9: Moment curvature behaviour

- Fatigue.

Excessive yielding means that the yield limit in the material is exceeded so that the material yields until failure. If the weight of the free spanning section is too large in a free-span, the material at the shoulders may yield until the pipe hits the bottom in the span.

When the pipe cross-section is exposed to bending moment, compressive and tensile stresses develops in the pipe cross-section. The combined action of curvature gives a squeeze force that tend to ovalise the cross-section. This is illustrated in Figure 2.9(a) where the tensile/compressive stresses are shown in red and blue colours, respectively. At some point the yield limit of the material is reached and the increase in stress can no longer compensate the reduction in the diameter, the maximum bending moment is reached and somewhere beyond that point the pipe will collapse. The associated bending moment response curve is illustrated in Figure 2.9(b).

Exposure to combined action of bending and external pressure will accelerate the buckling process whereas internal pressure will act to stabilize the buckling process by means of action of tensile stresses in the hoop direction..

Impacts or abrupt bending deformation, e.g. caused by loosing the pipe during failure in the installation vessel tensioner system (that holds the weight of the suspended pipe), may further cause the buckling process to start and propagate along the pipe at a lower pressure than the theoretical collapse pressure. This phenomenon is termed *buckle propagation*. For thin and medium walled pipes, thicker sections are normally applied at certain intervals to stop this process (so called *buckle arrestors*).

Accidental loads from e.g. falling objects may cause denting of the pipe and is much related to the high risk areas close to the platform infrastructure. Protection in terms of soil cover or mechanical protection may be required in order to fulfil the limit state criteria..

The welds will contain defects. Even if *NDT* testing is performed for each weld, there is a limitation in how small defects that can be discovered. The defects may cause the weld to fail by brittle fracture before the theoretical maximum bending moment in Figure 2.9(b) is reached. In order to define the allowable moment capacity, fracture mechanics based Engineering Criticality Assessment (*ECA*) is required, considering the base and weld material characteristics versus the nature of weld defects, see [Berg et al., 2009], [DNVGL, 2006b], [PD6493, 1991].

As mentioned above, plastic strains are allowed to occur in steel pipelines as long as it can be proved that the maximum allowable strain is not exceeded (this also includes evaluation of weld defects and fracture). The standards such as [DNVGL, 2012] limits the maximum accumulated plastic strain that can be allowed when summing up the contributions from both installation and operation.

For high temperature and pressure flowlines cyclic plasticity effects due to the combined action of alternating buckling and hoop stress cycles in combination with temperature de-rating of the material may contribute to low cycle fatigue. Low cycle fatigue may also result from the installation phase by repeated plastic straining or from repeated global buckling resulting from subsequent start-up and shut-downs during operation. In addition to this comes high-cycle fatigue from the hydrodynamic loads discussed above. The total fatigue is obtained by considering all these effects, either by application of fracture mechanics based calculations or from application of Miner's rule using S-N curves obtained from testing, see [DNVGL, 2010b].

The pipeline is normally installed in empty condition. When the installation is completed, the pipe is waterfilled and hydrostatic tested to prove weld performance. Thereafter the water is removed and the pipe wall dried prior to operation. This is normally carried out by sending a set of *pigs* (a plug that is hydraulically pumped along the pipeline) through the pipeline system. This is also known as the commissioning phase.

The governing loads and associated failure modes during installation and commissioning are:

- Gravity. The weight of the pipe string during installation may cause:
 - Excessive yielding. At the stinger some plastic straining is allowed since the pipe strains cannot exceed the value determined by the stinger radius
 - Local buckling including buckle propagation. The sagbend section is critical.
 - Fracture due to excessive bending and tension. The stinger section is critical
 - Lateral stability issues with respect to the balance between the transverse forces generated by the combination of installation tension and route curvature versus the available soil friction.
- Wave and current induced loads and vessel motion may cause:
 - Fatigue due to vessel/pipe and seabed/pipe interaction induced by vessel motion.

- On-bottom lateral instability due to hydrodynamic loads. The time before waterfilling is critical as the low weight in combination with wave and current load action may cause the pipe to move away from the desired route. This may again lead to interference with other installations or in worst case excessive yielding and buckling.
- Vortex induced vibration and fatigue.
- External pressure together with pipeline bending may cause local buckling and collapse. The sagbend section of the pipe string will be most critical.
- Hydrostatic testing may either cause excessive yielding in the hoop direction (bursting) or as a result of combined loads e.g. due to bending at the shoulders in free-spans.

The governing loads and associated failure modes during operation can be summarised as:

- Gravity. For pipelines resting on irregular seabeds, the weight of free spans may induce large bending moments at the shoulders which may cause:
 - Excessive yielding.
 - Local buckling or weld fracture. Critical sections are free span shoulders where the bending moment is largest,
- Wave and current induced loads may cause:
 - Fatigue due direct action of wave loads in free-spans.
 - On-bottom lateral instability of pipelines resting on the seabed possibly causing interference with other installations or in worst case excessive yielding, weld fracture and buckling.
 - Vortex induced vibration induced fatigue in free-spans.
- Operation temperature and pressure may cause:
 - Bursting specially due to high pressure and material degradation from subsequent variations in temperature and pressure. If the cyclic strain range includes accumulation of plastic strains, instabilities in terms of material thinning might occur, so called *ratcheting* [Jiao and Kyriakides, 2009].
 - Global buckling due to thermal elongation which may lead to excessive bending, local buckling and weld fracture.
 - Low cycle fatigue due to subsequent shut-downs and start ups.
- Interference with fishing activities may cause:
 - Excessive yielding and local buckling due to trawl gear or anchor pull-over.

- Fatigue due to trawl pull over.
- External pressure will act reduce the bending capacity related to the sustaining the above loads. During shut-down conditions (e.g. due to maintenance works at the platform) the internal pressure may only include the static pressure from the internal content. This is specially critical for gas pipelines since the density of gas may be in the range of 250kg/m^3 as compared to ≈ 1025 for seawater. This gives a net overpressure of $\approx 0.75\text{MPa}$ per 100m

2.4.2 Mechanical failure modes for flexible pipes

Flexible pipes are normally used for flexible risers or flowlines. The flexible pipe is a complex structure where each layer has different failure modes. The combined use of steel and thermoplastics introduce material compatibility issues. This is specially the case for high temperature and pressure applications, where cyclic transient loads may cause creep and tearing behaviours finally causing the cross-section to collapse. This leads to a significant increase in possible failure modes than for steel pipelines. For a detailed overview of these, see [API, 2008b], [API, 2008a] and [Ferestad and Løtveit, 2014].

The failure modes of the metallic layers include basically the same ones as for pipelines and include:

- Overload, i.e. excessive yielding in the metallic layers.
- Collapse of the cross-section due to external pressure.
- Local Buckling.
- Fatigue.

The cross-section strength is governed by the steel helix layers and the design analyses used to define the amount of steel needed are normally carried out according to the requirements of [API, 2008b] which applies the *allowable stress format*. This means that a load condition specific utilization factor is applied to the yield stress defining a stress limit that is not to be exceeded.

Collapse behaviour due to external pressure and bending is basically the same as for steel pipes. Design practice is based on the pessimistic approach that the outer sheath is leaking, i.e. the external pressure acts on the pressure barrier and need to be resisted by the Carcass. However, due to the non-bonded pipe structure that allow the layers to slide relative to each other, the bending stiffness is much less than for a steel pipe with same diameter. Hence, the interaction between pressure and bending is less dominant than for steel pipes.

The low bending stiffness makes free-spans on the seabed less likely to occur. On the other hand this gives less global buckling resistance. In North Sea applications, flexible flowlines are buried and/or covered with rock to provide mechanical protection. In order to control thermal buckling behaviour, the pipe is normally pressurized to hydrostatic test

pressure to initiate the global buckling process. This is then followed by burial or rock cover installation to fix the pipe in a pre-tensioned configuration that will result in smaller displacements when the operating temperature is applied.

The flexible pipe is manufactured in a continuous layer by layer process. Possible failures due to welding and fracture of the armour layers are avoided by ensuring that the welds needed to splice each armour wire are performed at different sections along the pipe and ensuring that no welds take place in the dynamic section of flexible risers.

The pipe is normally installed in empty condition. For deep water applications this gives significant compressive stresses in the tensile armour that may cause local buckling in the tensile armour, either in the lateral or radial directions of the armour wire, the latter termed *bird-caging*. Anti-buckling tape is commonly used to limit radial displacements and avoid the bird-caging failure mode.

Normally, the tensile armour is taken as the governing layer with respect to metal fatigue. The tensile armour is made of cold formed carbon steel with high yield stress and a limited corrosion resistance. Until mid nineties, the common fatigue design practise was based on assuming dry air environment, relying on an intact outer sheath and no leakage of gas from the bore to the annulus. Assuming that no welds were present in the dynamic section of the flexible pipe, the fatigue limit approach was applied where no stress range was allowed to exceed the defined limit, which for non-welded cold formed steels under in-air condition is in the range 400-600 MPa. At the early stages, the pipe designs were further based on not having antiwear tapes between the tensile armours and using wear models to estimate the cross-section reduction of the tensile armour as a function of time. This was based on Archard's formula considering the distance of relative displacements, the contact pressure, the wear coefficient and the material penetration hardness, see [Feret et al., 1986]. Fatigue failure was assumed to occur when the mean stress due to the loss of tensile armour cross-section caused the stress range to exceed the fatigue limit, normally defined at 10^6 cycles of constant amplitude loading.

During the fatigue tests on two 4 inch flexible pipes [Sævik et al., 1992a] and [Sævik et al., 1992b], fretting effects due to metal to metal contact was identified as a possible failure mechanism. Fretting occurs if an alternating stress in one direction is combined with contact stresses in the transverse direction, which may cause crack growth initiated from the contact surface. Since then anti-wear tapes have been introduced between the tensile layers and this failure mode is now rarely seen. One critical section where fretting may still be an issue, is the top end fitting where the tape layers are removed to allow anchoring the wires into the end fitting.

During the nineties it was realised that the in-air annulus assumption cannot be assumed, both due to a number of failures found in the outer sheath causing sea water ingress and leakage of corrosive ingredients such as H_2S and CO_2 from the bore into the armour annulus. The fatigue limit approach was therefore replaced by the Miner sum approach as applied in other steel structures.

The most critical sections with respect to fatigue in flexible risers are normally the top connection point at platform, the touch down point or the sagging and hogging sections, depending on the riser configuration. The most important loads include 1st order wave hy-

drodynamics and associated floater motions. Vortex induced vibration (VIV) is considered to be of less importance due to the damping contribution from the thermoplastic layers and the friction between the layers. However, for deep water applications, the contact pressure introduced by riser weight may cause the layers to be fixed relative to each other so that friction damping vanish. Therefore, the effect of VIV needs to be evaluated on a case to case basis.

2.5 Cross-section design

Steel pipelines and flexible pipes are primarily designed to carry the product to be transported, i.e to sustain the internal pressure. Hence, the selection of cross-section design in terms of wall thickness and dimension of armour layers is normally governed by the stress in the circumferential and axial directions of the pipe wall, i.e. *hoop stress* and *end cap stress* (axial stress that results from pressure). In order to provide safety against *excessive yielding* in the hoop direction (*bursting*), reduction (safety) factors are applied to the material yield stress ensuring sufficient cross-section strength. However, the pipe will be exposed to a set of different load conditions from it is manufactured, during installation throughout operation that may trigger other failure modes as well as noted in Section 2.4.

For deep water steel pipeline applications, local buckling due to external pressure may govern the selection of wall thickness. Even if the pipe is installed water filled, the density of the content during operation may be less than that of seawater, hence external over pressure may occur during shut-down and de-pressurisation conditions and this must be considered when designing the pipe wall. In some cases, the corrosive well flow may be dealt with by adding a corrosion allowance to the pipe wall. If it can be assumed that the corrosion takes place on the lower side of the pipe, this will give capacity benefit even at the end of the pipeline's life.

For large diameter export pipeline's at reasonable water depths, the hoop stress criteria normally governs, and buckle arrestors are used to deal with buckle propagation. For deep water export pipelines where the external pressure requirement governs, this failure mode may be eliminated by the required increase in wall thickness. For high internal pressure flowline applications, this may also be the case due to the heavy wall required to handle high reservoir pressures.

In cases where temperature induced global buckling takes place, it may become economic beneficial to increase the wall thickness to improve the local buckling capacity. Alternatively, intervention work for controlling the buckling process and limit the bending moments involved, is needed by e.g. rock installation. This is a cost optimisation exercise to be performed in each case.

The steel wall thickness to be selected may also be governed by the choice of installation method. If the reeling method is applied, the pipe may be plastically deformed. This will induce ovalisation and possible buckling. Hence, the wall thickness need to be selected to eliminate these failure modes.

For flexible pipes, the cross-section design analysis is normally based on the pressure

rating and use of analytical models considering axisymmetric effects alone (internal and external pressure, tension and torsion). In most designs, a pressure spiral is applied to support the internal pressure radial force whereas the axial force from end-cap pressure and gravity loads is sustained by the tensile armour. However, static applications at low pressure allow the support of both the axial and radial forces by the tensile armours alone. In that case the lay angle of the cross-wound tensile armour layers is $\simeq 55^\circ C$ which is the so-called *neutral angle*, see Section 8.4. The stress analysis is based on the mean stress approach. This means that only stresses due to the axial load in the wires are included when calculating the stresses. Secondary stresses in the wire due to manufacturing, bending and friction is not included. This relies on the assumption that the flexible pipe is a compliant structure where the secondary stresses can be taken care of by introducing a maximum curvature limit (minimum curvature radius), see [API, 2008b] to ensure that no overstressing takes place throughout the installation and operation phases. It is also assumed that the material is capable of taking the combined sum of manufacturing strain and strains resulting from the applied load. External overpressure is handled by the Carcass design (rough bore pipes). Water injection applications where the pipe is installed waterfilled may eliminate the need for a Carcass (smooth bore pipes).

Chapter 3

Heat transfer and thermal insulation

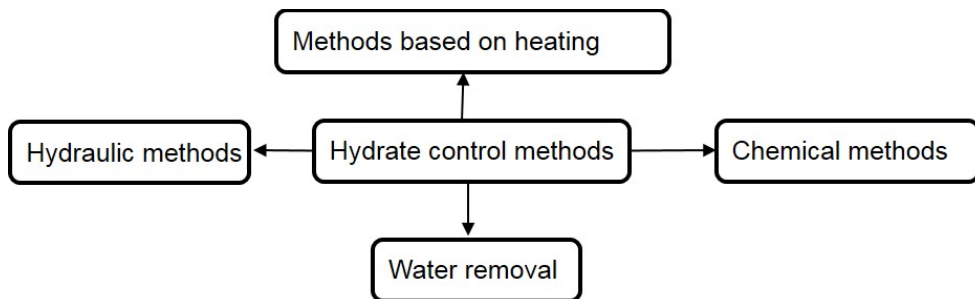


Figure 3.1: Alternative principles to avoid hydrate blocking

3.1 General remarks

For pipelines, the flow characteristics in combination with heat and pressure losses determines the temperature and internal pressure profiles along the pipe. Following, the commissioning phase, the flow will start to heat the pipeline, first at the inlet end then gradually along the pipeline. Provided that the flow is constant, steady state conditions will finally be reached. However, due to e.g. maintenance works in either ends, it is necessary to shut down the production at certain intervals. The pipe content will then start to cool down until it finally reaches the ambient temperature.

Due to pipe-soil interaction effects, the transient process of subsequent heating and cooling will result in non-linear and time dependent pipeline behaviours. The transient temperature distribution therefore represents a basic boundary condition with respect to the structural design process and close cooperation between structural and flow engineering disciplines is therefore needed during the pipeline design process as mentioned in Section 1.2.

This is of particular importance for flowlines that transports unprocessed flows at high operating temperatures and pressures. In such cases it is also important to control the temperature at the cool end so that hydrate formation is avoided. This can be done by application of different principles as illustrated in Figure 3.1 where the most commonly used ones are:

- Removing water from the flow
- Insulation and reduction of heat loss
- Chemical injection by feeding anti-freeze liquids into the flow
- Methods based on active heating

Water removal by subsea processing represents a key factor with respect to cost reduction in future designs as it allows unprocessed flow over long distances, thus eliminating the need for additional process platforms. Insulation can be obtained by application of

high performance coating technology including pipe in pipe systems, soil burial or combinations of these. Electrical heating systems have been developed to improve the flowline shut-down performance, either in the form direct electrical heating *DEH* or as part of pipe in pipe systems. DEH is based on application of an electrical power cable installed on top of the pipeline (*piggy-back*). During shut downs, the power is turned on and heat will be generated in the steel pipe due to the electrical field induced, see [Nysveen et al., 2005].

In order to optimize the operating philosophy with regard to avoiding hydrate formation and provide input to pipeline design, the engineering phase includes flow calculations by applying advanced flow simulators such as OLGA® and LedaFlow® to accurately capture the thermodynamics related to the above.

Here, some simplified analytical formulates will be derived to give some basic understanding of which physical parameters that are important in such analyses. This includes:

- The heat transfer coefficient.
- The steady state temperature profile.
- The time until the critical temperature is reached at the cool end during shut-down.

3.2 The heat transferr coefficient

Heat is transported in three fundamental ways as illustrated in Figure 3.2:

- By conduction
- By radiation
- By convection

Of the above effects only convention and conduction gives significant contributions for heat transfer in pipelines.

3.2.1 Conduction

In cylindrical coordinates, the heat diffusion equation can be written as:

$$\frac{1}{r} \frac{\partial}{\partial r} \left(kr \frac{\partial T}{\partial r} \right) + \frac{1}{r^2} \frac{\partial}{\partial \psi} \left(k \frac{\partial T}{\partial \psi} \right) + \frac{\partial}{\partial x} \left(k \frac{\partial T}{\partial x} \right) + \dot{q} = \rho C_p \frac{\partial T}{\partial t} \quad (3.1)$$

where:

T = the temperature (K).

r = the radial coordinate (m).

x = the longitudinal coordinate (m).

ψ = the circumferential coordinate (rad).

\dot{q} = the heat generation ($\frac{W}{m^3}$).

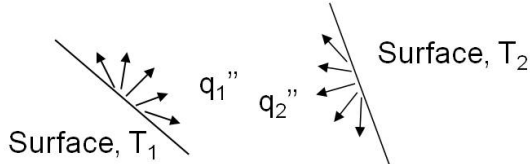
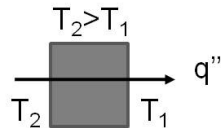
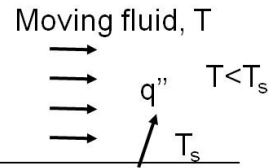
a) radiation:**b) conduction:****c) convention:**

Figure 3.2: Principles of heat transferr

ρ = density ($\frac{kg}{m^3}$).

C_p = Specific heat capacity ($\frac{J}{kgK}$).

k = thermal conductivity ($\frac{W}{mK}$).

For the long length pipeline case, axial heat transfer and variations in the circumferential direction in Eq. 3.1 can be neglected, so for the case without heat generation we are left with:

$$\frac{1}{r} \frac{\partial}{\partial r} (kr \frac{\partial T}{\partial r}) = \rho C_p \frac{\partial T}{\partial t} \quad (3.2)$$

For the steady state case, this gives the heat flux Q_r per unit length along the pipeline as:

$$Q_r = -2\pi rk \frac{dT}{dr} \quad (3.3)$$

By multiplying with dr on both sides, integration and introducing the boundary conditions in terms of the temperatures T_1 and T_2 respectively on the inside and outside radii r_1 and r_2 of layer 1 the following expression is obtained:

$$T_1 - T_2 = \frac{Q_r \ln(\frac{r_2}{r_1})}{2\pi k_1} = \frac{Q_r}{R_1} \quad (3.4)$$

where R_1 represents the layer heat conduction resistance. By dividing the cross-section into n multiple layers and summing up the contribution for each layer, the heat flux can be expressed as:

$$Q_r = \frac{T_1 - T_n}{\sum_{j=1}^n \frac{\ln(\frac{r_{j+1}}{r_j})}{2\pi k_j}} = \frac{T_1 - T_n}{\sum_{j=1}^n \frac{1}{R_j}} = UA(T_1 - T_n) \quad (3.5)$$

where U is called the heat transfer coefficient ($\frac{W}{m^2 K}$) and normally refers to the inner pipe surface where the area $A = 2\pi r_1$ which gives:

$$U = \frac{1}{r_1 \sum_{j=1}^n \frac{\ln(\frac{r_{j+1}}{r_j})}{k_j}} = \frac{1}{2\pi r_1 \sum_{j=1}^n \frac{1}{R_j}} \quad (3.6)$$

3.2.2 Convection

At the outer and inner surfaces heat transport takes place by convection. The convection rate will depend on the flow physical properties and velocity governing the boundary layer thickness at the interfaces. The same heat must be transported through these layers as well, i.e.:

$$Q_r = 2\pi r_i h_i (T_i - T_1) = 2\pi r_o h_o (T_n - T_o) \quad (3.7)$$

where:

$$\begin{aligned} h_i &= \text{the internal convection coefficient } (\frac{W}{m^2 K}) \\ h_o &= \text{the external convection coefficient } (\frac{W}{m^2 K}) \end{aligned}$$

which by application of the same principles as in Eq. 3.5 and Eq. 3.6 gives:

$$U = \frac{1}{\frac{1}{h_i} + r_i \sum_{j=1}^n \frac{\ln(\frac{r_{j+1}}{r_j})}{k_j} + \frac{r_i}{r_o h_o}} \quad (3.8)$$

It is noted that in cases where the pipe is buried or insulated, the contributions from convection are normally insignificant compared to the insulation/burial conductive terms.

3.2.3 Influence of soil burial

Flowlines are normally buried into soil both to improve the insulation properties and to provide mechanical protection. This gives extra contribution to the insulation so that the total U-value can be expressed as:

$$U = \frac{1}{\frac{1}{h_i} + r_i \sum_{j=1}^n \frac{\ln(\frac{r_{j+1}}{r_j})}{k_j} + \frac{r_i}{r_o h_o} + \frac{r_i}{k_{soil}} \cosh^{-1}(\frac{z}{r_o})} \quad (3.9)$$

where z is the burial depth to the pipe centre.

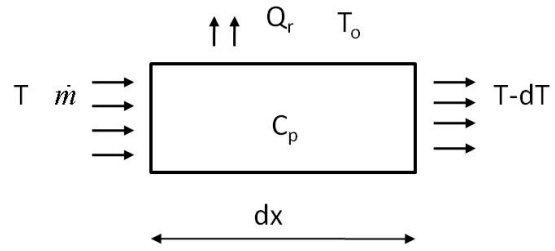


Figure 3.3: Heat flux in small pipe segment

3.3 The temperature profile

Assuming steady state conditions, axisymmetric heat flow and constant internal pressure, the temperature profile can be obtained by considering the heat flux in and out of an infinitesimal pipe segment as shown in Figure 3.3

With reference to Eq. 3.5 the net heat loss through the pipe wall can be expressed by:

$$Q_r = 2\pi r U dx (T - T_o) \quad (3.10)$$

This must accordingly be balanced by a reduction in the heat content inside the pipe of:

$$Q_r = -\dot{m} C_p dT \quad (3.11)$$

where \dot{m} is the mass flux ($\frac{kg}{s}$). By equating Eq. 3.10 and Eq. 3.11, integrating on both side and introduce the inlet temperature T_{in} and the external temperature T_o as boundary conditions, the following expression is obtained for the temperature profile along the pipe:

$$T = (T_{in} - T_o) e^{-\frac{2\pi r_i U}{\dot{m} C_p} x} + T_o \quad (3.12)$$

3.4 Time to reach critical temperature

During shut-downs the well flow will stop and the pipe will start to cool down. If it is assumed that the pipe is insulated by a thin efficient layer of insulation so that most of the heat is stored inside of the insulation, the time until a critical temperature can be estimated by the approach shown in Figure 3.4 where axisymmetric heat flow, no heat exchange in the axial direction and no time dependency in material properties are assumed.

The most critical section will be the cool end which starts from an inside temperature T and having an outside temperature of T_o . From Eq. 3.10, the heat passing through the pipe during a time increment dt is:

$$dQ = Q_r dt = 2\pi r U dx (T - T_o) dt \quad (3.13)$$

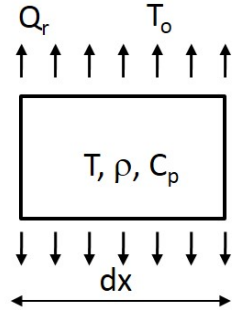


Figure 3.4: Heat flux in infinitesimal element during shut-down condition

This leads to a change in heat content of:

$$dQ = - \sum \rho_i C_{pi} A_i dx dT \quad (3.14)$$

where A_i is the area of layer i and the summation includes the annulus and steel layers. By equating Eq. 3.13 and Eq. 3.14, and integration on both sides, the time t until the critical temperature T_c is reached is found to be:

$$t = \frac{\sum C_{pi} \rho_i A_i}{2\pi r U} \ln\left(\frac{T_s - T_o}{T_c - T_o}\right) \quad (3.15)$$

where the radius r refers to the inside of the insulation layer. Hence U must be defined accordingly.

One limitation in the above procedure is that it excludes the effect of heat storage within the insulation layers. In reality different materials also change the heat capacity with temperature. In order to take such effects into account, more advanced methods are needed e.g. by the finite difference scheme, see [Bai and Bai, 2005].

Example 3.4.1 Cool-down during shut down This example is to illustrate the results obtained by using different insulation with respect to temperature profile and shut down times. Input data are given in Table 3.1.

By using Eq. 3.12, the temperature profiles presented in Figure 3.5 are obtained. Further, by using Eq. 3.15 in combination with the obtained end temperatures at the cool end, the shut down times presented in Table 3.2 were found. It is seen that insulation or burial significantly improves the critical time performance with respect hydrate formation.

Table 3.1: Cross-section data for temperature profile and shut-down time analysis

Parameter	Value	Unit
Flowline length	5000	m
Internal diameter	0.152	m
Steel wall thickness	0.015	m
C_{pfluid}	2053	$\frac{J}{kgK}$
C_{psteel}	500	$\frac{J}{kgK}$
C_{psoil}	900	$\frac{J}{kgK}$
ρ_{fluid}	800	$\frac{kg}{m^3}$
ρ_{steel}	7850	$\frac{kg}{m^3}$
k_{steel}	50	$\frac{W}{mK}$
k_{soil}	1.6	$\frac{W}{mK}$
Oil inlet temperature	100	$^{\circ}C$
Ambient temperature	5	$^{\circ}C$
Critical temperature	25	$^{\circ}C$

Table 3.2: Results in terms of shut-down times

Case	Shut down times (hrs)
2 cm insulation	3.8
10 cm insulation	17.1
20 cm soil	2.6
100 cm soil	6.9

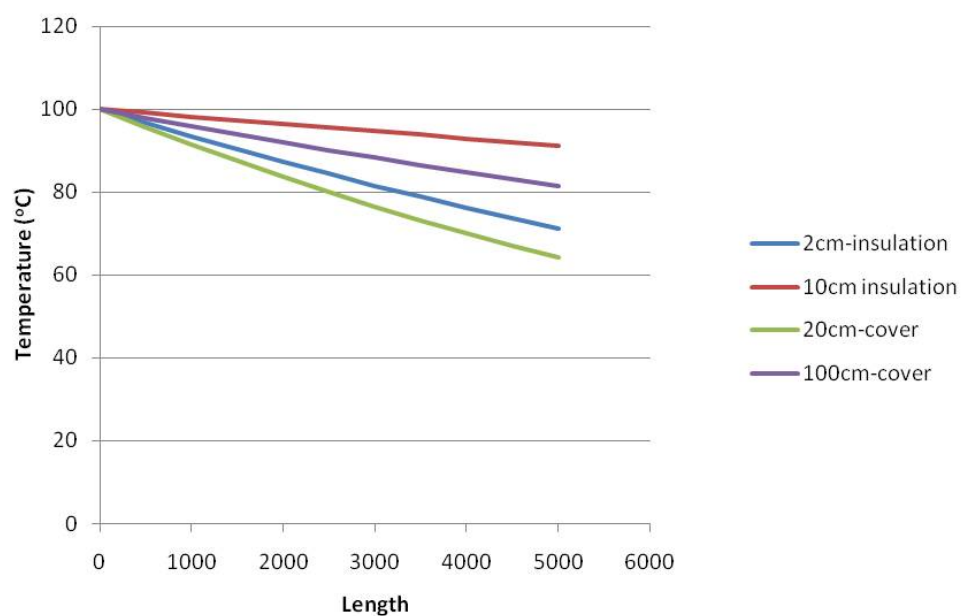


Figure 3.5: Temperature profile

Chapter 4

Pipeline Design

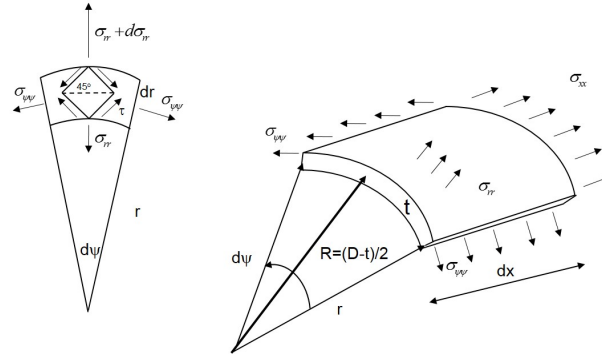


Figure 4.1: Stress components in the pipe wall

4.1 General remarks

The purpose of the present section is to give an understanding of the stress components and the physical effects that are inherent in pipeline design formulas used for wall thickness sizing and stress checks. There are several different design codes in use for wall thickness sizing, applying slightly different approaches. A review and comparison between these can be found in [Bai and Bai, 2005]. Here an outline of the basic principles is given, using [DNVGL, 2012] as a reference. Stress components in flexible pipe cross-sections are dealt with in Chapter 8.

4.2 Stress and strain components

The components of stress in the pipe wall due to internal and external pressure and external loads are shown in Figure 4.1. The $\sigma_{\psi\psi}$ (hoop) stress can be described by thin walled or thick walled shell theories. The thick walled theory is based on radial equilibrium assuming no shear stress components $\sigma_{r\psi}$ on the side surfaces as visualised in Figure 4.1 and expressed as:

$$(\sigma_{rr} + d\sigma_{rr})(r + dr)d\psi - \sigma_{rr}rd\psi - \sigma_{\psi\psi}drd\psi = 0 \quad (4.1)$$

$$\frac{d\sigma_{rr}}{dr} + \frac{\sigma_{rr} - \sigma_{\psi\psi}}{r} = 0$$

which by introduction of the plane stress Hooke's law in two dimensions, the radial displacement v and the strain quantities:

$$\epsilon_{rr} = v_{,r} \quad (4.2)$$

$$\epsilon_{\psi\psi} = \frac{v}{r} \quad (4.3)$$

gives the following differential equation:

$$r^2 v_{,rr} + r v_{,r} - v = 0 \quad (4.4)$$

which is known as the Euler equation with solution:

$$\sigma_{rr} = \frac{E}{1-\nu^2} \left[C_1 - \frac{C_2}{r^2} + \nu \left(C_1 + \frac{C_2}{r^2} \right) \right] \quad (4.5)$$

$$\sigma_{\psi\psi} = \frac{E}{1-\nu^2} \left[C_1 + \frac{C_2}{r^2} + \nu \left(C_1 - \frac{C_2}{r^2} \right) \right] \quad (4.6)$$

For a pipe exposed to an internal pressure p_i at the internal surface and an external pressure p_e at the external surface, this gives the following hoop stress $\sigma_{\psi\psi}$ at the internal and external radii r_i and r_e :

$$\sigma_{\psi\psi,i} = \frac{(r_i^2 + r_e^2)p_i - 2r_e^2 p_e}{r_e^2 - r_i^2} \quad (4.7)$$

$$\sigma_{\psi\psi,e} = \frac{-(r_i^2 + r_e^2)p_e + 2r_i^2 p_i}{r_e^2 - r_i^2} \quad (4.8)$$

where it is noted that the largest tensile hoop stress occurs on the inner pipe wall in internal overpressure cases.

The general solution valid for any radius r in the pipe wall, considering both the hoop and radial stress components are:

$$\sigma_{\psi\psi} = \frac{p_i r_i^2 - p_e r_e^2}{r_e^2 - r_i^2} + \frac{(p_i - p_e)r_i^2 r_e^2}{(r_e^2 - r_i^2)r^2} \quad (4.9)$$

$$\sigma_{rr} = \frac{p_i r_i^2 - p_e r_e^2}{r_e^2 - r_i^2} - \frac{(p_i - p_e)r_i^2 r_e^2}{(r_e^2 - r_i^2)r^2} \quad (4.10)$$

Consistent with no shear stresses at the side surfaces, the maximum shear stress will occur at an orientation of 45° relative to these and given by:

$$\tau = \frac{1}{2}(\sigma_{\psi\psi} - \sigma_{rr}) = \frac{(p_i - p_e)r_i^2 r_e^2}{(r_e^2 - r_i^2)r^2} \quad (4.11)$$

Further by noting that the first term in Eq. 4.9 and Eq. 4.10 represent the longitudinal stress due to the end-cap force $\sigma_{xx,p}$ these equations can be written as:

$$\sigma_{\psi\psi} = \sigma_{xx,p} + \tau \quad (4.12)$$

$$\sigma_{rr} = \sigma_{xx,p} - \tau \quad (4.13)$$

From the above it can be concluded that at any point in the pipe wall, the stresses can be decomposed into [Sparks, 1984]:

1. A hydrostatic component $\frac{1}{2}(\sigma_{rr} + \sigma_{\psi\psi}) = \sigma_{xx,p}$

2. A deviatoric shear stress $\frac{1}{2}(\sigma_{\psi\psi} - \sigma_{rr}) = \tau$
3. A constant axial stress from the external axial load represented by the effective tension T_{eff} which gives $\sigma_{xx,eff} = \frac{T_{eff}}{\pi(r_e^2 - r_i^2)} = \frac{T_{eff}}{(A_e - A_i)}$

Some codes such as [DNVGL, 2012] are based on thin walled theory where:

$$\sigma_{\psi\psi} = \frac{(r_i + r_e)}{2t}(p_i - p_e) = \frac{R}{t}(p_i - p_e) = \frac{D - t}{2t}(p_i - p_e) \quad (4.14)$$

and where R is the mean radius, D is the outer pipe diameter and t is the wall thickness. For pipes that are not restrained by external forces (e.g. from soil friction), the longitudinal stress due to internal and external pressure is determined by the end cap force and the steel area, i.e. for the thick walled case:

$$\sigma_{xx,p} = \frac{(\pi r_i^2 p_i - \pi r_e^2 p_e)}{\pi r_e^2 - \pi r_i^2} \quad (4.15)$$

which for the thin walled case with $R = \frac{1}{2}(D - t)$ gives:

$$\sigma_{xx,p} = \frac{\pi R^2(p_i - p_e)}{2\pi R t} = \frac{1}{2}\sigma_{\psi\psi} \quad (4.16)$$

By assuming no external forces, the longitudinal strain ϵ_{xx} due to pressure and temperature effects can be expressed using thin walled theory as:

$$\epsilon_{xx} = \frac{\pi R^2(p_i - p_e)}{E 2\pi R t} - \nu(p_i - p_e) \frac{R}{Et} + \alpha \Delta T = \frac{\pi R^2(p_i - p_e)}{EA_p}(1 - 2\nu) + \alpha_T \Delta T \quad (4.17)$$

where the second term is related to the two-dimensional Hooke's law and the Poisson effect of pressure induced hoop stress. ν is the Poisson's number, ΔT is the temperature change and α_T is the temperature elongation coefficient, A_p is the pipe wall cross-section area and E is the Young's modulus.

In order to perform excessive yielding stress checks in steel materials for combined loads, the Von Mises's equivalent stress criteria is normally used as it gives a good description of the yield process due to multi-axial stresses in metals. In the two dimensional case, neglecting shear stresses, the equivalent stress criteria is given by:

$$\sigma_e = \sqrt{\sigma_{xx}^2 + \sigma_{\psi\psi}^2 - \sigma_{xx}\sigma_{\psi\psi}} \quad (4.18)$$

4.3 Wall thickness design

4.3.1 The hoop stress (bursting) criteria

Different standards use slightly different formulations to deal with the bursting criteria. In the [DNVGL, 2012] formulation, the required wall thickness to avoid excessive yielding in the hoop direction is based on the following design format:

$$p_i - p_e \leq \frac{p_b}{\gamma_m \gamma_{SC}} \text{ where } p_b \leq \frac{2t}{D-t} \sigma_{cb} \frac{2}{\sqrt{3}} \text{ and where } \sigma_{cb} = \text{Min} \left[\sigma_y, \frac{\sigma_u}{1.15} \right] \quad (4.19)$$

The above requirement is referred to as the pressure containment (bursting) criteria and is based on inserting Eq. 4.16 and Eq. 4.14 into Eq. 4.18 and equating this to the characteristic strength σ_{cb} which is determined from either of the yield stress σ_y or the ultimate stress σ_u . The target safety level is obtained by means of a material factor γ_m coping with material uncertainties and a safety class factor γ_{SC} that depends on the application.

4.3.2 External pressure collapse

The external pressure collapse equation applied in [DNVGL, 2012] is based on calibration against test data. Here, the background for the Timoschenko equation of collapse of circular rings [Timoshenko and Gere, 1963] will be presented as it provides an easy interpretation of which physical effects that are involved.

The elastic buckling of a circular ring starts out with considering yield in the hoop direction at the outer fibre of the pipe wall, see Figure 4.2. Collapse is assumed when:

$$\sigma_{\max} = \frac{p_e R}{t} + \frac{M_{\max}}{t^2/6} = \sigma_y \quad (4.20)$$

where the stress consists of the contributions from the hoop stress and the bending moment that occurs due to the imperfect shape described by the ovalisation parameter $\delta_0 = \frac{v_0}{R}$ where v_0 is the imperfection amplitude of the assumed function $v_0 \cos 2\psi$, see Figure 4.2. This is consistent the definition $(D_{\max} - D_{\min})/(D_{\max} + D_{\min})$ used in several standards.

Starting from the above imperfection shape, external pressure gives load terms both in terms of membrane forces and bending. This can be evaluated based on curved beam theory under the following assumptions:

- Only bending strains over the thickness in hoop direction is considered.
- Plane strain conditions, no strains along the pipe.
- Membrane strains in the hoop direction are assumed to be zero.
- No shear deformations, i.e. plane surfaces that were orthogonal to each other before deformation remain so after deformation.

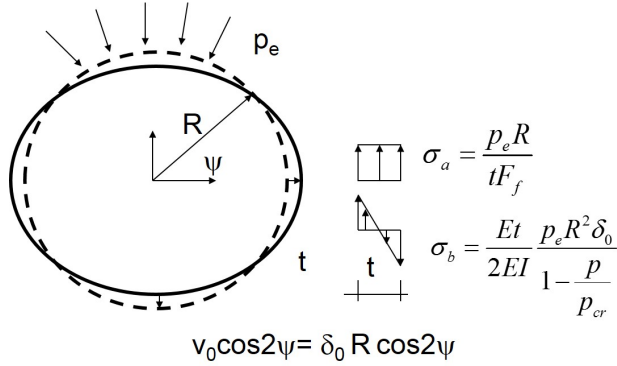


Figure 4.2: Timoshenko collapse model

Introducing the curve linear axis system $s = R\psi$, t and n in the hoop, axial and radial directions, respectively, and only allowing for the displacement in the hoop direction u and the radial direction v , the quantity that defines the bending deformation in the case of a curved beam with initial curvature $1/R$ [Sævik, 1992] can be applied to obtain:

$$\omega_t = -\frac{d^2v}{ds^2} + \frac{1}{R} \frac{du}{ds} \quad (4.21)$$

where ω_t is the curvature deformation quantity of hoop bending (about the local longitudinal axis). The membrane strain in the hoop direction can further be expressed as:

$$\epsilon_{\psi\psi} = \frac{du}{ds} + \frac{v}{R} \quad (4.22)$$

Then by imposing the zero membrane strain condition in the hoop direction:

$$\frac{du}{ds} = -\frac{v}{R} \quad (4.23)$$

which inserted into Eq. 4.21 gives:

$$\omega_t = -\frac{d^2v}{ds^2} - \frac{v}{R^2} \quad (4.24)$$

Then by introducing the convention that a positive bending moment gives tensile stresses on the outside of the pipe surface:

$$M = -EI \left(\frac{d^2v}{ds^2} + \frac{v}{R^2} \right) = p_e R (v_0 \cos 2\psi + v) \quad (4.25)$$

and then:

$$\frac{d^2v}{ds^2} + \frac{v}{R^2} + \frac{p_e R v}{EI} = -\frac{p_e R}{EI} v_0 \cos 2\psi \quad (4.26)$$

where EI is the hoop bending stiffness per unit length of pipe given as:

$$EI = \frac{Et^3}{12(1 - \nu^2)} \quad (4.27)$$

Further by introducing $ds = Rd\psi$:

$$\frac{d^2v}{d\psi^2} + \left(1 + \frac{p_e R^3}{EI}\right)v = -\frac{p_e R^3}{EI} v_0 \cos 2\psi \quad (4.28)$$

The total solution of the above differential equation is given by the sum of the homogeneous and particular solutions where the homogenous solution takes the form:

$$v_h = C_1 \sin k\psi + C_2 \cos k\psi \quad (4.29)$$

where $k^2 = 1 + \frac{p_e R^3}{EI}$ and C_1 and C_2 are constants given by the initial conditions:

$$v(\psi = 0) = v_0 \quad (4.30)$$

$$\frac{dv}{ds}(\psi = 0) = 0 \quad (4.31)$$

which gives:

$$v_h = v_0 \cos k\psi \quad (4.32)$$

The critical elastic buckling pressure is obtained by imposing:

$$\frac{d^2v}{ds^2}(\psi = \frac{\pi}{4}) = 0 \quad (4.33)$$

which gives a non-trivial solution only for $k = 2$ as:

$$p_{cr} = 3 \frac{EI}{R^3} \quad (4.34)$$

Then the particular solution is found by assuming a solution of the form $C_1 \cos 2\psi$ as:

$$v_p = \frac{v_0 p_e}{p_{cr} - p_e} \cos 2\psi \quad (4.35)$$

The hoop bending moment is then obtained as:

$$M = p_e R(v_h + v_p) = \frac{p_e R^2 \delta_0}{1 - \frac{p_e}{p_{cr}}} \cos 2\psi \quad (4.36)$$

where the denominator represents the amplification of the moment due to the buckling effect and where p_{cr} by introducing Eq. 4.27 can be written as:

$$p_{cr} = \frac{3EI}{R^3} = \frac{E}{4(1 - \nu^2)} \left(\frac{t}{R}\right)^3 \quad (4.37)$$

By inserting Eq. 4.36 and Eq. 4.37 into Eq. 4.20, the collapse pressure p_c can be defined as the pressure needed to cause first yield at the outer fibre in the hoop direction as:

$$p_c^2 - p_c \left[\sigma_y \frac{t}{R} + \left(1 + 6 \frac{R}{t} \delta_0 \right) p_{cr} \right] + \sigma_y p_{cr} \frac{t}{R} = 0 \quad (4.38)$$

The limitation of the above equation is that it gives a poor description of plastic collapse governing thick walled pipe behaviour, i.e low D/t ratios. This is not unexpected since it assumes failure to occur at first yield. Therefore, the equations describing this failure mode applied in e.g. [DNVGL, 2012] are modified to give a better description of the transition from elastic collapse (High D/t) to plastic collapse (Low D/t).

4.4 Design against other relevant failure modes in steel pipelines

4.4.1 Buckling due to combined loads

The buckling design criteria to be applied for combined loading depends on the load condition, whether it is displacement controlled or force controlled. The two load conditions are illustrated in Figure 4.3. The pipeline response exposed to gravity load in a free span is clearly force controlled and the interaction between failure due to the axial, bending moment and external pressure load effects can be handled by an equation describing the interaction between the different associated failure modes on the following format:

$$f\left(\frac{M}{M_c}, \frac{T}{T_c}, \frac{p}{p_c}\right) = 0 \quad (4.39)$$

where M_c is the critical bending moment related to bending buckling, T_c is the critical axial force and p_c is the critical pressure. The critical pressure will depend on whether the pressure differential is positive or negative. If it is positive (internal over-pressure), the critical pressure will be governed by yielding whereas buckling as described by Eq. 4.38 will take place for external over-pressure cases. The latter case will tend to reduce the moment capacity M_c whereas internal over-pressure will cause a tensile hoop stress acting to support the cylinder surface, thus reducing the ovalisation and increasing the moment capacity. Hence different design equations are needed for the different cases [DNVGL, 2012]. In principal, the critical axial force T_c will also depend on whether the axial force is positive (tension) or negative (compressive). If it is positive T_c will be described by the axial yielding capacity alone, whereas in the compressive case, axial (pipe shell) buckling should be considered in the T_c expression. However, for the D/t ratios relevant for pipelines, axial yielding will take place before axial shell buckling and there is hence no need for including this failure mode in most cases.

The displacement controlled case can be treated by considering the critical strain at the outer fibre instead of the axial and moment load effects and application of the following format:

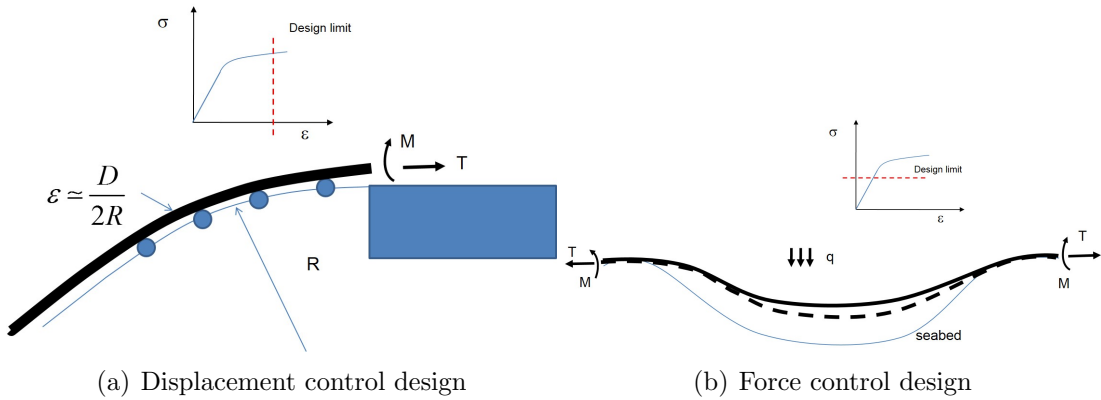


Figure 4.3: Illustration of displacement and load control scenarios

$$f\left(\frac{\varepsilon}{\varepsilon_c}, \frac{p}{p_c}\right) = 0 \quad (4.40)$$

4.4.2 Fatigue

The fatigue due to crack growth in the welds resulting from cyclic loads can be calculated either by application of fracture mechanics principles or by means of the Miner sum approach using fatigue data obtained from testing. By application of the Miner sum approach, the design criterion is formulated as:

$$D_m = \sum_{i=1}^N \frac{n_i}{N_i} < D_{ff} \quad (4.41)$$

where N is the number of stress range classes, n_i is the number stress ranges in each class and N_i is the number of allowable cycles at each stress range class and D_{ff} is fatigue design factor (< 1) that depends on the application, see [DNVGL, 2012]. N_i is then obtained from an S-N diagram on the following format:

$$\lg N_i = \lg a - m \lg(\Delta\sigma_i) \quad (4.42)$$

where $\lg a$ and m are constants obtained by material testing of the relevant material and welding method, also including the inherent uncertainties. Depending on the weld geometry, stress concentration factors may have to be included when calculating the stress ranges.

4.4.3 Other mechanical failure modes

The capacity equations given above requires that sufficient capacity of the welds are obtained. The weld capacity is governed by material selection, which welding method to

be applied and the performance of the NDT technique used to check the quality of the welds. All these parameters need to be evaluated. Reference is given to [PD6493, 1991] and [Berg et al., 2009].

Chapter 5

Material selection and welding

5.1 General remarks

The overall basis for pipeline material selection is to ensure economic and safe product transport. During the pipeline design phases, the material engineering includes different activities where the conceptual design phase normally focus on identifying the material requirements in terms of:

- Internal conditions: Corrosion, Erosion
- Corrosion Allowance
- Linepipe material selection
- Linepipe material requirements
- External coating evaluation and selection
- Corrosion protection preliminary design

This is then followed by the detailed design phase that includes:

- Linepipe material definition
- External coating definition
- Corrosion protection design
- Specifications for materials
- Linepipe/Components/Coating/Anodes
- Specifications for fabrication

The above is a multi-discipline activity that need to interact with other disciplines such as:

- Process engineering, giving input in terms of:
 - Fluid composition/chemistry
 - Production rates for the applicable fluid components
 - Temperature and pressure (design and operation / min. and max.) profiles
 - Insulation requirements
- Structural design installation requirements given by the selected installation methods:
 - Reel/S-lay/J-lay/Bundle
- Structural design wall thickness requirements considering:

- Water depth along the route
- The need for buckle arrestors
- Structural design and operation requirements

In the following the basic principles of material selection will be discussed. This is followed by a brief description of different alternative welding methods and associated non-destructive test methods (NDT).

5.2 Material selection

The basic question related to costs is to identify whether carbon steel can be used or not. In many cases carbon steel can be applied even in corrosive environments. However, this requires calculation of corrosion rates and the required corrosion allowance (CA). Corrosion allowance is the amount of pipe wall that can be allowed to corrode without violating the operation design requirements. Note that the benefit from this extra wall may be utilised during installation e.g. by allowing the reel method to be applied. It may also be beneficial during operation depending on which assumptions that can be applied in terms of the distribution of corrosion around the pipe wall. The decision to be made is much related to the fluid composition; whether water is present or not and the amount of CO_2 .

[NORSOK STANDARD, M506] gives an internal CO_2 corrosion model. However, corrosion rate calculations is only one element in a material selection process. Other essential factors are uncertainty in input data for corrosion rate calculations, construction and commissioning conditions, consideration of normal and upset operating conditions, actual corrosivity of produced fluids, scale, wax, inhibitor efficiency and geometry of corrosion attacks. These and other factors may influence the actual corrosion rates considerably, and be more important than any uncertainty in the corrosion rate calculations. Evaluation of results as defined in [NORSOK STANDARD, M001] states that if the corrosion rate resulted in a CA for the design life larger than 10 mm, then a Corrosion Resistance Alloy (CRA) need to be applied.

Another fundamental question is whether corrosion inhibition is to be applied or in case of condensed water, pH stabiliser. This requires a planned corrosion management with corrosion monitoring and corrosion inhibition.

If a CRA linepipe is needed, possible candidates are:

- 13 % Cr martensitic stainless steel
- 22 % Cr duplex stainless steel
- 25 % Cr duplex stainless steel
- Carbon steel with 316L stainless steel liner

- Carbon steel with 22% Cr duplex stainless steel liner
- Carbon steel with 25% Cr duplex stainless steel liner
- Carbon steel with 904L stainless steel liner
- Carbon steel with Alloy 825 liner
- Carbon steel with Alloy 625 liner

The above materials can be delivered as seamless pipes or seam welded pipes, normally delivered in 12 m lengths. The seamless pipe is formed by forging and thus have no longitudinal welds, the maximum diameter for manufacturing such pipes is about 16 inches (1 inch = 1" = 25.4 mm) and with a maximum wall thickness of approx. 50 mm depending on diameter.

The seam welded pipe is manufactured from flat steel plates that are formed and then longitudinally welded. Such pipes are applicable for large diameters from 18" inch up to 60"-84" and with wall thicknesses up to 50 mm depending on diameter.

A cost saving alternative to full CRA linepipe is carbon steel with an internal CRA liner. Such pipes can be manufactured by applying two different principles:

- By metallurgical bonding of the CRA to the carbon steel
- By installing the CRA pipe inside the steel pipe and then provide mechanically bonding by applying expansion forces

Carbon steel pipe with internal polyethylene (PE) liner also represents an alternative in e.g. water injection systems.

5.3 Pipeline welding

5.3.1 General

Welding is a fabrication process that joins materials, usually metals or thermoplastics. The main idea is to bond the surfaces together by liquefying the material surfaces and thereafter allowing the liquid to solidify. At the end of this process the two pieces of material have become one continuous solid. This is often done by melting the workpieces and adding a filler material to form a pool of molten material (the weld pool) that cools to become a strong joint.

For metals, electrical arc welding is the governing method. An electric arc is an electrical breakdown of a gas which produces an ongoing plasma discharge, resulting from a current flowing through normally nonconductive media such as air. In arc welding, an electrode is further used to conduct current through a workpiece to fuse two pieces together. Depending upon the process, the electrode is either consumable, in the case of gas metal arc welding or shielded metal arc welding, or non-consumable, such as in gas tungsten arc welding. In

order to provide good quality welds of metals, the weld material cannot be allowed to react with the atmospheric gases such as oxygen, nitrogen, carbon dioxide, and water vapour as these gases can reduce the quality of the weld.

One way of controlling the weld environment is by applying shielding gases as in gas metal arc welding to protect the weld area from the atmospheric gases. Other arc welding processes use other methods of protecting the weld from the atmosphere. Shielded metal arc welding, for example, uses an electrode covered in a flux that produces carbon dioxide when consumed, a semi-inert gas that is an acceptable shielding gas for welding steel.

5.3.2 Welding processes

The following processes are applied for Subsea Pipelines and Systems Fabrication, see [Cary, 1979] (Designation in numbers, reference to [ISO, 4063]) :

Shielded Metal Arc Welding (SMAW 111)

A consumable electrode coated with flux, is used to produce the weld. An electric current, in the form of either alternating current or direct current from a welding power supply, is used to form an electric arc between the electrode and the metals to be joined. As the weld metal is deposited, the flux coating of the electrode disintegrates, giving off vapors that serve as a shielding gas and provides a layer of slag, both of which protect the weld area from atmospheric contamination. The method is applied in the manual mode.

Flux Cored Arc welding (FCAW 136/137)

Semi-automatic or automatic arc welding process. FCAW requires a continuously-fed consumable electrode containing a flux and a constant-voltage or, less commonly, a constant-current welding power supply. An externally supplied active (136) or inert (137) shielding gas is normally used, but the flux itself also provides good protection from the atmosphere. FCAW is the dominating weld process in the Norwegian offshore sector (laybarge welding not included) due to its high welding speed and portability.

Tungsten Inert Gas welding (TIG 141)

Arc welding process where an electric arc is burning between a non-consumable tungsten electrode and the workpiece. The weld area is protected from atmospheric contamination by a shielding gas (usually an inert gas such as argon), and filler metal is normally added.

GTAW is known as a high quality welding method, but with low productivity. GTAW is most commonly used to weld thin sections of stainless steel and light metals such as aluminum, magnesium, and copper alloys.

Submerged Arc Welding (SAW 121)

SAW is an arc-welding process that uses a continuously fed consumable, solid or tubular (flux cored). The molten weld metal and the weld arc are protected from atmospheric contamination by being *submerged* under a blanket of granular fusible flux. When molten, the flux becomes conductive, and provides a current path between the electrode and the work. This thick layer of flux completely covers the molten metal, thus preventing spatter and sparks.

SAW is normally operated in the automatic or mechanized mode. SAW is known as the most effective welding process and is used for producing longitudinal weld in seam welded pipes and double-jointing (joining two 12m joints together to speed up the installation process).

Gas Metal Arc Welding (GMAW 131/135)

Single wire Gas Metal Arc welding is the dominant pipe girth welding technique applied on pipeline installation vessels. The method makes use of a consumable wire electrode which heats the workpiece metal(s), causing them to melt, and join. Along with the wire electrode, a shielding gas feeds through the welding gun, see Figure 5.1. The weld is performed by several *passes*, starting with the *root pass* at the inside of the pipe, followed by *filler passes* and ending by a *cap pass* that build somewhat outside the pipe external surface.

5.3.3 Non destructive testing

The purpose of NDT testing is to find weld defects. In general, the less well defect that can be detected, the better pipe mechanical performance in terms of structural capacity. There are three different principles in use in order to inspect the welding process with respect to defects and weld acceptance:

- UT: Ultrasonic Testing - High frequency ultrasound pulses are emitted from a transducer at the surface of a sample. The sound waves propagate through the sample, and reflect at interfaces. The reflected waves are monitored using a detector at the surface.
- RT: Radiographic Testing - radiographic film being placed under a sample. The sample is then exposed to radiation, the radiation passes through the sample, and exposes the film.
- AUT: Automated Ultrasonic Testing A series of UT angle probes is localised in specific areas of the weld zone. Every zone has a specific calibration reflector. The scanner is calibrated against controlled reference reflectors, simulating weld defects.

AUT is the dominant inspection method for pipeline girth welds, and preferred by [DNVGL, 2012]

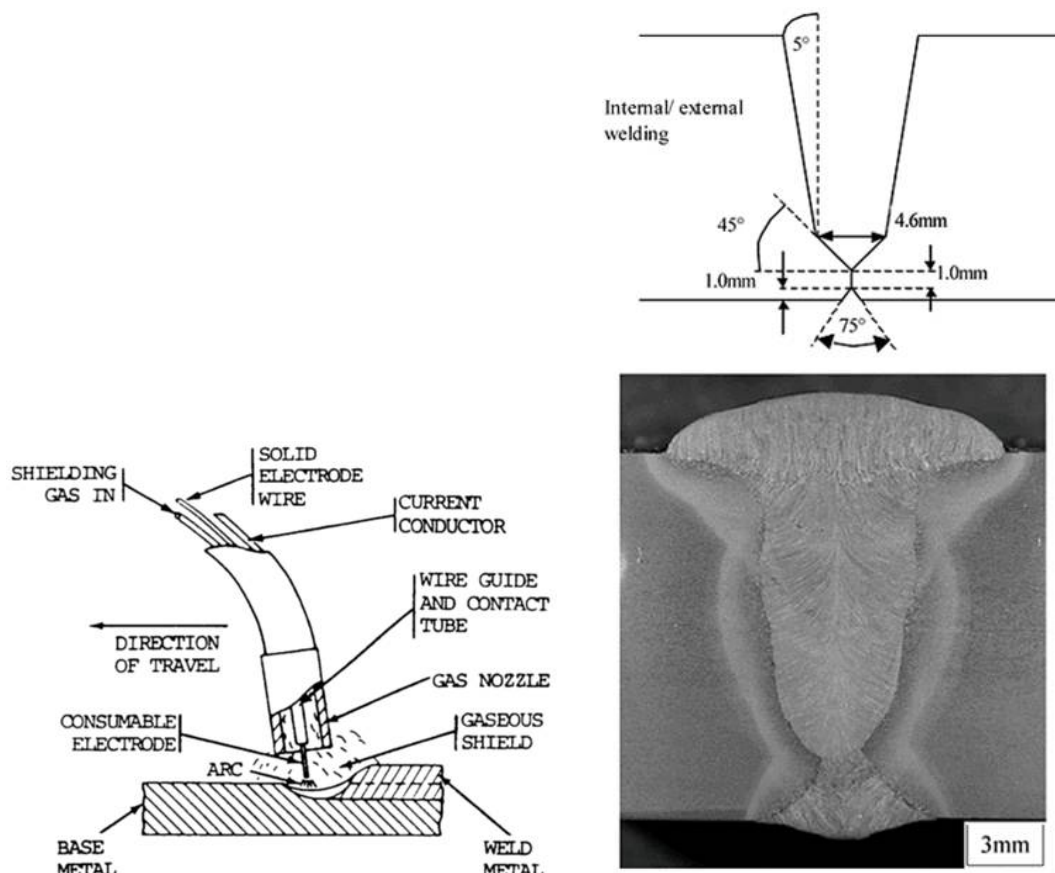


Figure 6-6. Gas metal arc welding.

Figure 5. CAPS weld bevel and macro-section from weld in 14.9 mm wall X100 linepipe.

(a) GMAW welding principle

(b) GMAW weld

Figure 5.1: GMAW welding [REINERTSEN, 2009]

Chapter 6

Pipeline installation

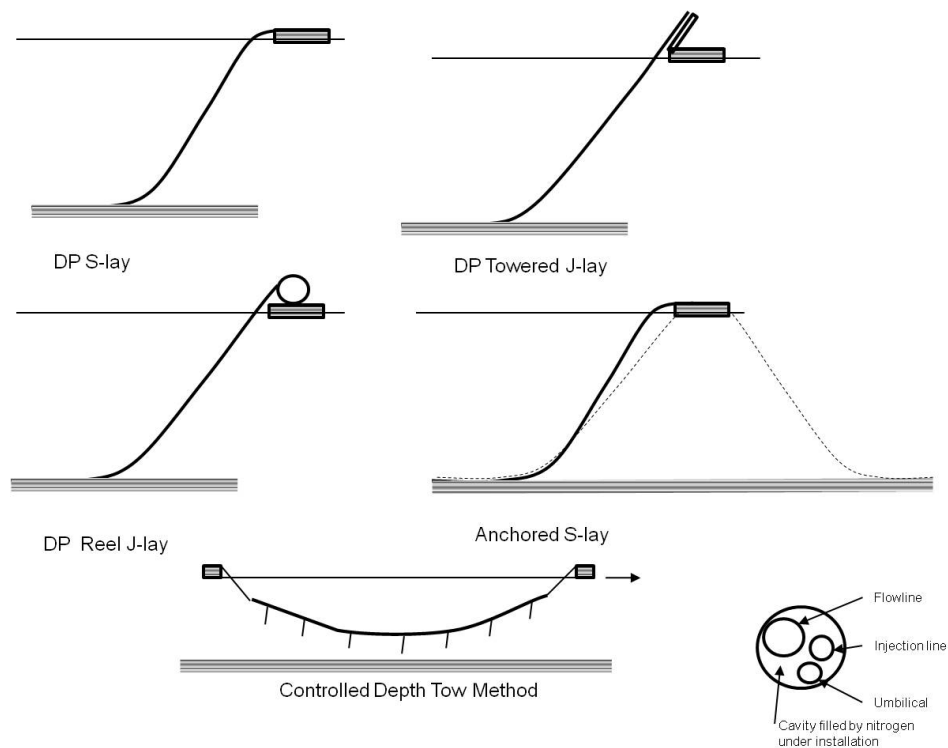


Figure 6.1: Pipeline installation methods

6.1 General remarks

In the following, different pipeline installation methods will be discussed. This is followed by an analytical treatment of different topics related to installation analysis, including:

- The concept of *effective tension*
- The catenary equation
- Minimum curvature radius in the horizontal plane
- Residual radius and roll behaviour

6.2 Pipeline installation methods

Figure 6.1 gives an overview of different pipeline installation methods.

There are 3 main installation methods in use:

- Tow methods
- J-lay

- S-lay

of which only J-lay is of relevance for flexible pipe and cable installation.

6.2.1 Controlled Depth Tow Method

The Controlled Depth Tow Method (*CDTM*) is applicable for flowline bundles. A bundle may include all elements that are needed to connect the subsea well to the existing infrastructure including flowline, umbilical and injection lines. The bundle is fabricated onshore and the basic elements are built into a carrier pipe which is filled with nitrogen during installation. The nitrogen is pressurised to balance the external pressure so that the carrier pipe do not collapse. At moderate water depths this procedure will give net buoyancy so that the pipe can be floated by two tug boats to the field. Anchor chains are connected at regular intervals at the lower side of the bundle. During tow, the drag force will create lift forces on the chain elements so that the entire bundle will float in the water. When the tow is stopped, the bundle will sink until the length of the chain resting on the seabed balance the loss in lift forces. The buoyancy is thus tuned so that the bundle floats a certain distance above the seabed at zero tow velocity. This requires very accurate weight control during the manufacturing process.

When approaching to the target, the bundle is left in floating condition until the ends have been tied into the sub-sea connection points. Thereafter, the bundle is filled with injected (anticorrosion) water. The main advantage of this method is that the manufacturing can be completed under controlled condition onshore and allow installation by low cost tug boats. However, the length that can be installed in one operation is limited by the current forces and associated drift off/manoeuvrability difficulties. In North Sea conditions this means about 3 km. Longer lengths means sub-sea tie-ins which will add costs. Another limiting factor is water depth. The more water pressure, the more internal pressure of nitrogen is needed to avoid collapse during tow-out. This means thicker wall and increased density of the nitrogen, and at one point it is not possible to obtain net buoyancy. By application of conventional carbon steels, these factors limit the method to about 1000 m.

6.2.2 J-lay

For the J-lay method, the pipe is installed in a J-shaped (*catenary*) configuration and is entering the water at a certain angle (*the top angle*) that is governed by the water depth, the submerged weight of the pipe and the applied horizontal tension. The lower horizontal tension, the higher top angle, and the shorter *layback length*, i.e. the horizontal length from where the pipe leaves the vessel to it touches the seabed at the *touch down point (TDP)*.

J-lay installation is normally performed either by reeling or by welding using a Dynamically Positioned (*DP*) vessel where DP means that station keeping is provided by thrusters rather than by anchors and anchor lines. For the reeling method, the pipe string is manufactured onshore and then reeled onto the lay barge. For steel pipe installation, plastic deformations will normally occur, depending of diameter. The amount of plasticity

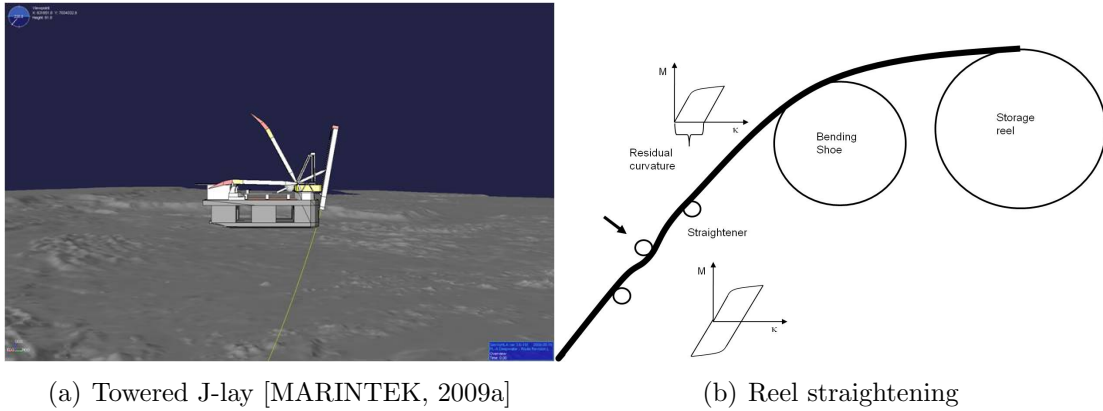


Figure 6.2: J-lay by welding and reeling

that can be allowed limits the maximum steel pipe diameter to about 18 inches for this method. When the pipe is unreeled during installation, the pipe needs to be straightened. This is normally performed by first bending all pipe sections to the same bending radius by application of a bending shoe. This is because the pipes stored on the outermost layers have larger radius than the inner layers. Then, the straightener setting will be the same for all pipe sections. The straightener may include three rollers, where the mid one is placed eccentric to the two others, then bending the pipe in the opposite direction, see Figure 6.2(b) and a straight pipe will result.

Alternatively, the pipe joints are welded together on the barge. However, this requires that the pipe joint is welded to the pipe string in an almost vertical position. Since, the pipe string manufacturing procedure also requires stations for application of anti-corrosion coating at the welded section (*the field joint*) and NDT testing, this requires a tower of considerable height. Hence there is limited room for welding stations (normally only one). To compensate for this, welding of quad joints (48 m), manufactured onshore or onboard the vessel, can be applied to speed up the process. This concept is mainly used for deep water installation of large diameter pipes, as was the case for the pipeline installation at the Ormen Lange gas field northwest Norway, see Figure 6.2(a).

6.2.3 S-lay

For the S-lay method the pipe string is installed in an S-shape, see Figure 6.1 i.e. the pipe is launched horizontally from the vessel. This requires that the pipe is supported by a *stinger* that provides a smooth transition from the horizontal position to a certain angle termed the *the departure angle* from where the suspended section basically will behave as a catenary similar to J-lay. The section from the vessel to the inflection point where the direction of curvature shifts sign is termed the *overbend* whereas the lower section is termed the *sagbend*. S-lay installation is performed either by reeling or by welding either using a Dynamically Positioned *DP* vessel or an anchored lay barge. Since the pipe string

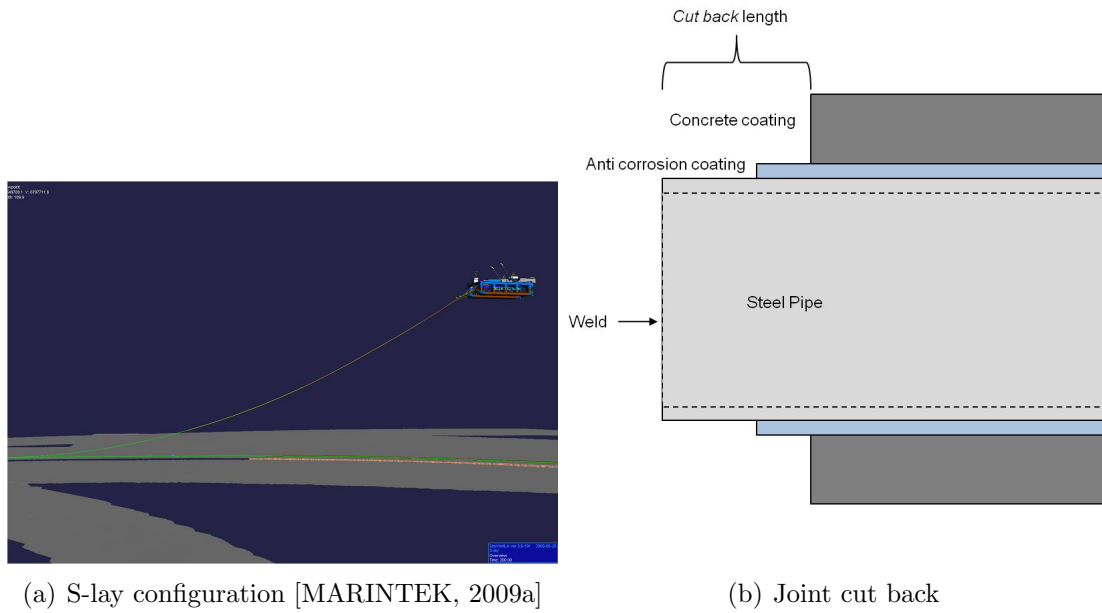


Figure 6.3: Illustration of S-lay configuration and field joint prior to coating process

is launched in horizontal mode, the deck space allows for several welding stations along the *firing line*, one for each of the different welding *passes*, see Section 5.3, to fill up the weld groove. By combining this by separate stations for manufacturing double joints (24 m), very efficient pipe string manufacturing can be obtained. S-lay is the dominant method for installation of long length large diameter pipelines at moderate water depths. The firing line also includes stations for application of anti-corrosion coating at the bare steel weld section. Shallow water large diameter pipes, may also need additional weight coating (normally concrete) to provide sufficient weight for hydrodynamic stability. In order to allow space for welding, the pipes are delivered from the coating plant with a certain cut back (30-40 cm), see Figure 6.3(b), which gives diameter discontinuity. To allow the pipe to slide along the roller boxes of the stinger without crushing the weight coating, the diameter discontinuity has to be eliminated by coating the field joint section by eg. a rapid solidifying polyurethane on the outside of the anti-corrosion coating.

Note that the Young's modulus of the fill material is usually much less than for concrete. This will give strain concentrations in the field joints when exposing the pipe to bending. This has to be taken into account when evaluation the pipeline strength both during installation and operation.

6.2.4 Selection of method

The CDTM tow method both allow onshore fabrication and installation by standard low cost tug boats. However, it is mostly applicable for short and reasonable straight flowline

sections due to manoeuvrability limitations.

One basic advantage of the reel method is that it allows manufacturing the pipe string under controlled conditions onshore and that the installation rate is high, hence costs related to offshore installation is minimised. Since the daily rates of such vessels may be several millions NOK per day, minimising installation times means cost reduction. However, due to the diameter limitation this method is mostly applicable for flowlines and flexibles. A limited number of available vessels may also enhance other methods to be used.

For J-lay, the horizontal tension needed to keep the catenary shape is governed by the minimum curvature that can be allowed in the *sagbend* which again is determined by the pipe buckling capacity. The resulting top angle will depend on the water depth and the vessel is equipped with an adjustable ramp providing support of the pipe as it enters into the sea. However, the adjustment capability is limited and therefore restricts the minimum water depth for application of J-lay. In the case of welding J-lay, the tower height limits the number of welding stations and the lay rate tends to be less than for S-lay.

The horizontal tension and the transverse friction force that can be mobilised between the pipe and the seabed governs the minimum radius of curvature that can be allowed for routing the pipeline along the seabed. In uneven terrains, minimising the number of free spans is crucial with respect to cost savings. This may require multiple curves at low curvature radii. In deeper waters J-lay may be the only alternative in such cases, since it allows for small horizontal tension at the seabed.

The stinger applied in S-lay provides a support of the pipe as it enters into the sea. For shallow water installation, the gravity load of the free spanning pipe is partly carried by membrane and beam bending stiffness effects. The deeper water, the longer span length and the more the membrane effect will govern the global configuration. The effect of bending stiffness will be to reduce the required horizontal tension during shallow water installation. Hence DP S-lay will be favourable for shallow water installation with complicated routing and manoeuvrability requirements. When the pipe enters into deeper waters, the limitation of stinger length means higher top angle and horizontal tension than would be required for J-lay. This means that at some water depth J-lay will be favourable with respect to pipeline curve stability. Another limitation of S-lay is fatigue of the stinger due to wave and pipe interaction forces from vessel motions. This may limit the weather window within which the lay operation can take place.

6.3 Pipeline installation analysis

In order to determine the installation forces and associated stresses, there are several techniques available:

- Analytical calculations based on the catenary equation
- Finite differences solution of the stiffened catenary equation

- Finite differences solution of the full non-linear beam equation
- The Finite Element (FE) method

The structural analysis of pipeline installation includes a number of non-linearities such as:

- Non-linear loads
- Non-linear geometry
- Plastic material behaviour
- Interaction between pipe, stinger and tensioner machinery
- Pipe-soil interaction

Only the FE method is capable of handling all the above items in a consistent way and full time domain integration of the non-linear equation of motion is normally needed to capture all relevant effects related to dynamic behaviour and fatigue, see Chapter 9. However, in order to determine the main lay parameters such as the required lay tension, simplified analysis based on analytical formula's or finite differences as stated above can be performed.

In the following four topics of relevance to the above will be addressed:

- The effective tension concept
- The catenary equation
- Minimum horizontal lay radius
- Residual radius and roll

6.3.1 The effective tension concept and Archimedes law

In the literature the concept of *effective tension* is referred to when explaining the behaviour of slender marine structures, see [Sparks, 1984].

It is well known that the behaviour of beam structures can be described by six cross-section stress resultants; one axial force, two shear force components, one torsion moment and two bending moment components. The axial force is the result of integrating **all** stresses in the cross section. For a pipe, the inside may be filled with pressurised air, water, oil etc. and the inside annulus needs to be kept in equilibrium by stresses according to the same principles as for the steel part of the cross-section, see Figure 6.4. The mechanical behaviour resulting from a given axial force (such as buckling) do not differentiate between whether the axial force results from stresses related to keeping the annulus with its content in equilibrium or from stresses needed to keep the steel wall in equilibrium. Hence the

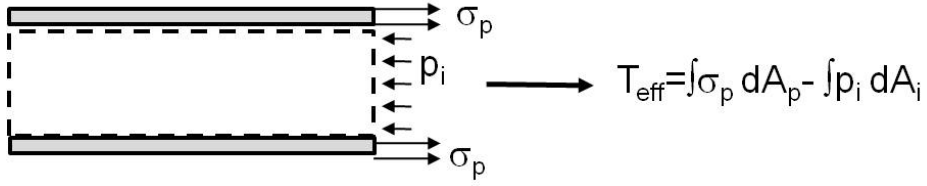


Figure 6.4: The effective tension concept

concept of effective tension is nothing more than the total cross-section resultant, resulting from integrating the stresses over the entire cross-section. This is intuitively realised with reference to Figure 6.4.

The total cross section axial force only considering internal pressure can then be written as:

$$T_{eff} = \int_{A_p} \sigma_p dA_p - \int_{A_i} p_i dA_i = T_p - p_i A_i \quad (6.1)$$

where the subscript p refers to the pipe wall. What about external pressure?. It can of course be argued that external pressure attacks the external surface and has opposite sign of internal pressure, so therefore:

$$T_{eff} = \int_{A_p} \sigma_p dA_p - \int_{A_i} p_i dA_i + \int_{A_e} p_e dA_i = T_p - p_i A_i + p_e A_e \quad (6.2)$$

However, what is the physical interpretation of the above external pressure term? For a pipe segment that is water tight and submerged into the water, no one end surface is exposed to the external pressure. This can obviously not happen without application of an axial force that compensates the lack of external pressure stresses at all cross-sections, i.e. at each cross-section there must exist a force $+p_e A_e$.

Figure 6.5 illustrates the Archimedes law. By integrating all surfaces of a virtual pipe segment with length ds and submerged in water, the result will be a buoyancy force equal to $B = g\rho_w A_e ds$ necessary to keep the water element in equilibrium. All elements submerged into water will be exposed to the same buoyancy force equal to the weight of the submerged body volume, which is known as the Archimedes law. By application of the super-position principle, see [Sparks, 1984], and as illustrated in Figure 6.6, it is realized that the submerged pipe section can be described as a sum of contributions that gives an equivalent system of forces. The figure concludes that the pipe section can be described by the submerged weight taken as $w_s = w_p - g\rho_w A_e$ and an extra contribution to the effective tension equal to $+p_e A_e$. It is ,however, noted that as long as no external forces is applied to the system this force needs to be balanced by an opposite directed compressive force in the steel wall, such that the effective tension is zero. A closed pipe segment that is submerged

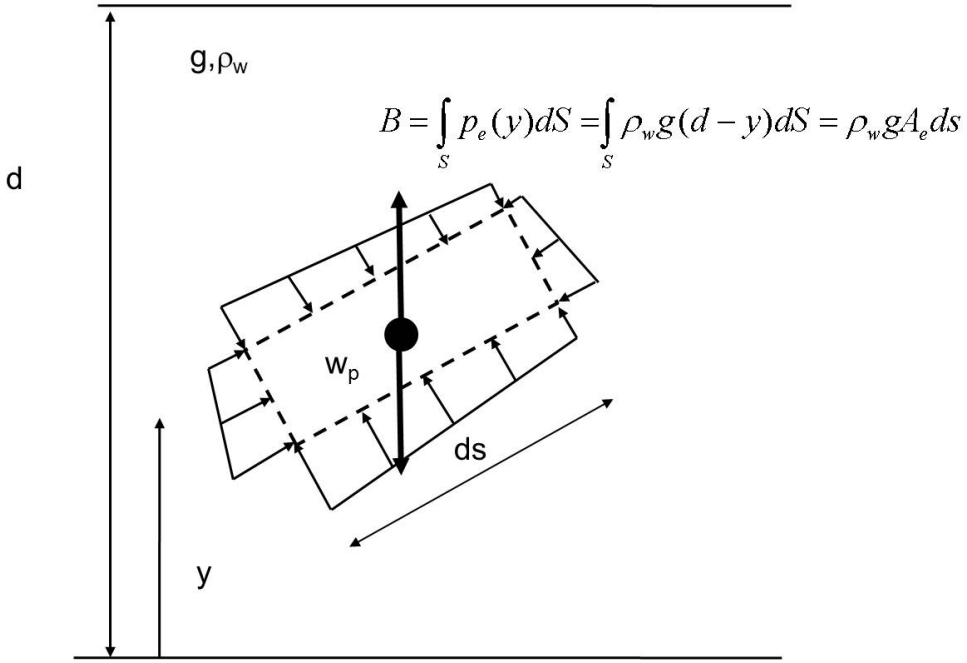


Figure 6.5: The Archimedes law considering a virtual pipe segment of water

into water can thus experience local shell buckling due to the compressive stresses in the pipe wall but will never experience global buckling since the latter is governed by the total stress resultant, i.e. the effective tension.

It is also possible to obtain the above conclusion based on integrating the pressure field and then studying the beam differential equation with respect to transverse equilibrium, see Figure 6.7. The buoyancy B acts transverse to the infinitesimal element and consists of two contributions:

- The pressure acting on the upper part of the pipe surface is less than the pressure acting at the lower part of the pipe surface (B_1)
- The area at the upper side is less than at the lower side (B_2)

The external pressure at any y -coordinate can be expressed by:

$$p_e = -g\rho_w r \sin \gamma \cos \theta + g\rho_w(d - y) \quad (6.3)$$

B_1 is then found by integrating the pressure around the circumference of the pipe surface as:

$$B_1 = - \int_0^{2\pi} p_e r \sin \gamma d\gamma = g\rho_w \int_0^{2\pi} r^2 \sin^2 \gamma \cos \theta d\gamma = g\rho_w A_e \cos \theta \quad (6.4)$$

where $A_e = \pi r^2$. B_2 is found by expressing the net area difference caused by the angular

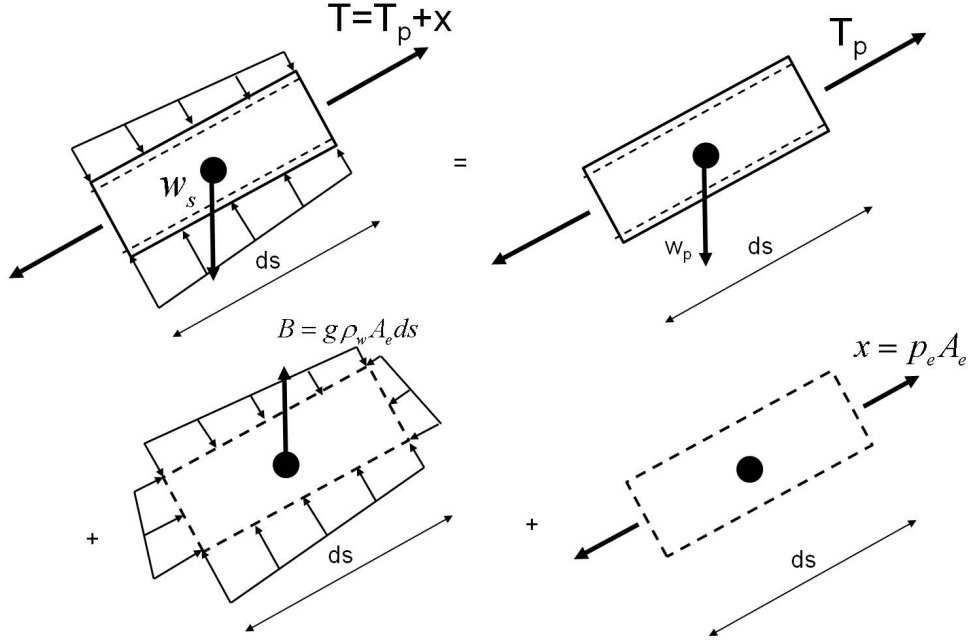


Figure 6.6: Application of the superposition principle of an equivalent system of forces

change $d\theta$ as $A d\theta$. This gives:

$$\begin{aligned} B_2 ds &= A_e g \rho_w (d - y) d\theta \\ B_2 &= A_e g \rho_w (d - y) \frac{d\theta}{ds} \end{aligned} \quad (6.5)$$

So the total buoyancy can be expressed as:

$$B = g \rho_w A_e [\cos \theta + (d - y) \frac{d\theta}{ds}] \quad (6.6)$$

By considering transverse equilibrium under the constraint that $d\theta$ is small:

$$(T_p + dT_p) d\theta + (Q + dQ) - Q + B ds - w_p \cos \theta ds = 0 \quad (6.7)$$

which by neglecting 2nd order terms and introducing the result from Eq. 6.6 gives:

$$\begin{aligned} [(T_p + g \rho_w A_e (d - y)) \frac{d\theta}{ds} + \frac{dQ}{ds}] &= (w_p - g \rho_w A_e) \cos \theta \\ [(T_p + p_e A_e) \frac{d\theta}{ds} + \frac{dQ}{ds}] &= w_s \cos \theta \\ T_{eff} \frac{d\theta}{ds} + \frac{dQ}{ds} &= w_s \cos \theta \end{aligned} \quad (6.8)$$

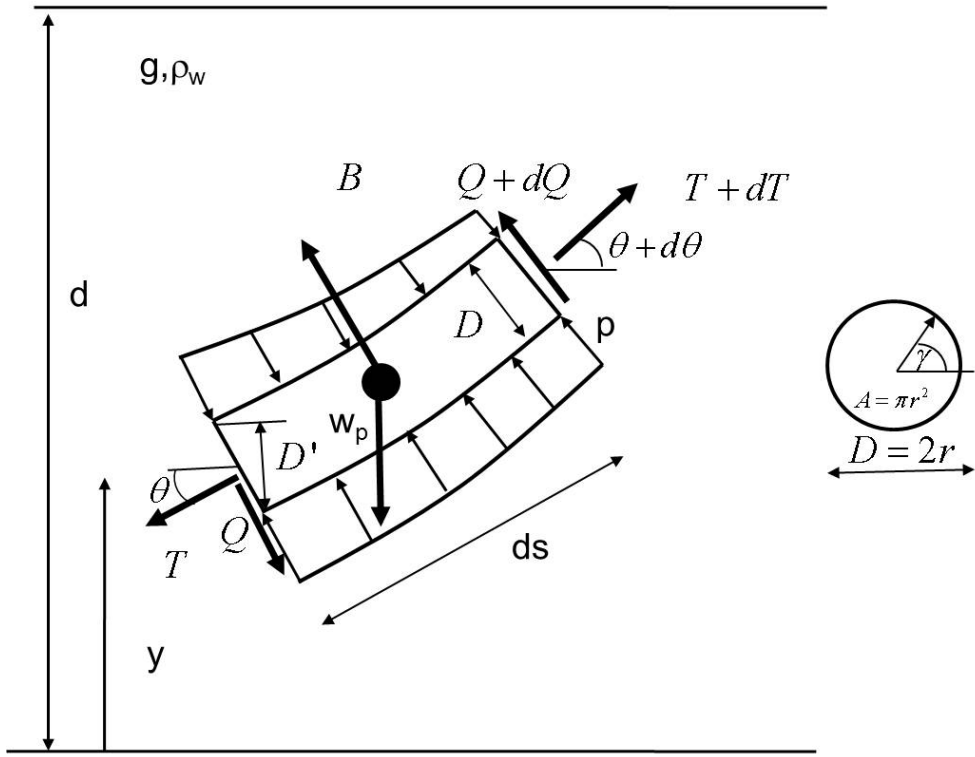


Figure 6.7: Infinitesimal beam element exposed to external pressure

which concludes the proof: *The mechanical behaviour is governed by the effective tension (the total stress resultant including both the pipe wall and the submerged/pressurised annulus) and the submerged weight.*

Also consider an infinitesimal element carried by tension forces alone and with no consideration of buoyancy effects, see Figure 6.8(a) positioned at coordinate point y as illustrated in Figure 6.8(b), then by equilibrium at position y :

$$dT_p = w_p \sin\theta ds = w_p dy \quad (6.9)$$

Further, by integration on both sides:

$$T_p = w_p y + T_{p0} \quad (6.10)$$

where T_{p0} is the pipe wall tension at the origin positioned at TDP. Then by direct application of Eq. 6.2 at the coordinate point y we get:

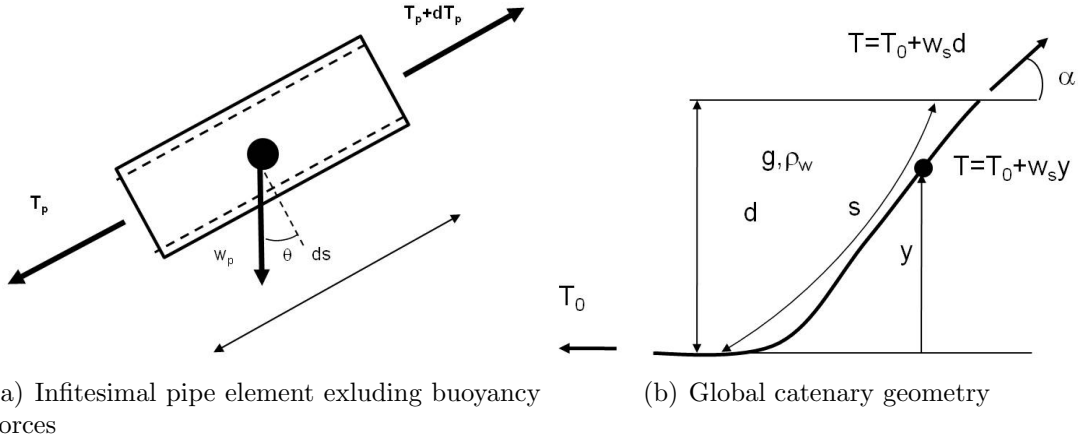


Figure 6.8: Effective tension along catenary

$$\begin{aligned}
 T_{eff} &= T_{p0} + w_p y + p_e A_e \\
 &= T_{p0} + w_p y + \rho_w g(d - y) A_e \\
 &= T_{p0} + \rho_w g d A_e + (w_p - \rho_w g A_e) y \\
 &= T_{eff0} + w_s y \\
 T &= T_0 + w_s y
 \end{aligned} \tag{6.11}$$

where T and T_0 hereafter will refer to the effective tension values.

6.3.2 The catenary equation

The catenary equation is based on neglecting the bending stiffness effect. This means that it will represent an approximate solution, even for J-configurations, specially with respect to the curvature at TDP which will be influenced locally by the pipe's bending stiffness. By neglecting the bending stiffness term in Eq. 6.8, equilibrium yields:

$$\begin{aligned}
 T d\theta &= w_s \cos\theta ds \\
 T &= w_s \cos\theta \frac{ds}{d\theta}
 \end{aligned} \tag{6.12}$$

Further, by differentiation on both side of Eq. 6.11 with respect to the length coordinate s :

$$\begin{aligned}
 \frac{dT}{ds} &= w_s \frac{dy}{ds} \\
 dT &= w_s \sin\theta ds
 \end{aligned} \tag{6.13}$$

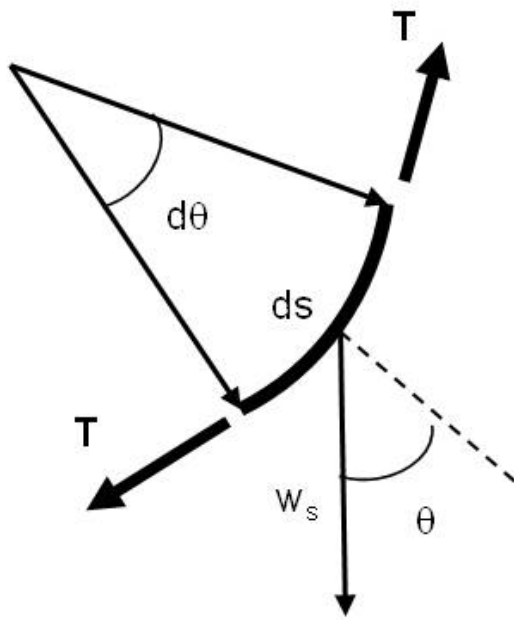


Figure 6.9: Infintesimal catenary segment - only tension - no bending stiffness

By dividing Eq. 6.13 with Eq. 6.12 and integrating on both sides, we get:

$$\begin{aligned} \frac{dT}{T} &= \frac{\sin\theta}{\cos\theta} d\theta \\ \ln T &= -\ln \cos\theta + C \\ T &= T_0 \frac{\cos\theta_0}{\cos\theta} \end{aligned} \quad (6.14)$$

where θ_0 represents the slope of seabed at TDP. If one assume $\theta_0 = 0$ at $s = 0$ then:

$$T = \frac{T_0}{\cos\theta} \quad (6.15)$$

Further from Eq. 6.15 and Eq. 6.12 and introducing the top angle α located at $s = s^*$ and $y = d$ as new parameters.

$$\begin{aligned} ds &= \frac{T d\theta}{w_s \cos\theta} \\ s &= \frac{T_0}{w_s} \tan\theta + C \\ \tan\theta &= \frac{w_s}{T_0} s \\ \tan\alpha &= \frac{w_s}{T_0} s^* \end{aligned} \quad (6.16)$$

We also have by using Eq. 6.11 and Eq. 6.16:

$$\begin{aligned} dy &= \sin\theta ds \\ &= \frac{T_0 \sin\theta}{w_s \cos^2\theta} d\theta \\ y &= \frac{T_0}{w_s \cos\theta} + C \\ d &= \frac{T_0}{w_s} \left(\frac{1}{\cos\alpha} - 1 \right) \end{aligned} \tag{6.17}$$

By application of Eq. 6.16 and Eq. 6.17, the catenary length s^* can be expressed in terms of the water depth d , the submerged weight w_s and the horizontal bottom tension T_0 as:

$$s^* = \sqrt{d^2 + 2 \frac{dT_0}{w_s}} \tag{6.18}$$

The curvature along the catenary is further found by application of Eq. 6.15 and Eq. 6.12 as:

$$\frac{d\theta}{ds} = \frac{w_s}{T_0} \cos\theta^2 \tag{6.19}$$

having its maximum value at TDP.

The horizontal length from TDP to the top connection point, the so-called *layback* x^* can further be found by utilising the above as:

$$\begin{aligned} dx &= \cos\theta ds \\ &= \frac{T_0}{w_s \cos\theta} d\theta \\ x &= \frac{T_0}{w_s} \ln\left(\frac{1}{\cos\theta} + \tan\theta\right) \\ x^* &= \frac{T_0}{w_s} \ln\left(1 + \frac{w_s d}{T_0} + \sqrt{\left(1 + \frac{w_s d}{T_0}\right)^2 - 1}\right) \end{aligned} \tag{6.20}$$

6.3.3 Minimum horizontal radius

One important routing and installation criterion is the minimum horizontal radius of curvature that can be obtained on the seabed. This is found by simple transverse equilibrium in the horizontal plane using the available lateral transverse force $\mu_y w_s$ instead of $w_s \cos\theta$ in Figure 6.9:

$$R_{min} = \frac{T_0}{\mu_y w_s} \tag{6.21}$$

6.3.4 Residual radius and roll

During S-lay and reel-lay the pipeline may be exposed to plastic strains in the stinger/drum section where a certain plastic strain can be allowed to occur. This is because the load scenario is *displacement controlled*, see Section 2.2, which means that the amount of strain will be governed by the radius of curvature of the stinger/drum rather than the external load. For an ideal elastic-plastic material and with reference to Figure 6.10(a), the moment curvature relation for a tubular section will take the form as indicated in Figure 6.10(b). If the pipe is bent to the value M_1 in the stinger section as indicated in the figure, a residual curvature κ_r will result as unloading takes place to $M = 0$, i.e. the pipe is no longer straight in the unloaded condition. For S-lay this will result in a non-straight pipe section leaving the stinger. For reel-lay a straightening device is used to introduce plastic deformation in the opposite direction to get a straight pipe before leaving the ramp, see Figure 6.2(b)

By considering a thin-walled tube pipe section as in Figure 6.11 that is exposed to a bending moment that gives plastic strains, the cross-section may be divided into two parts; one part that is still elastic, the second part being plastic. Further, by only including one component of moment and applying the same ideal elastic-plastic material, the transition between the elastic and plastic zone can be defined by:

$$\psi_0 = \sin^{-1}\left(\frac{\kappa_0}{\kappa}\right) \quad (6.22)$$

where κ_0 is the curvature at which yielding start to occur and κ is the applied curvature. Then the bending moment for an arbitrary curvature beyond κ_0 can be determined as:

$$M = 4\sigma_y R^2 t \cos \psi_0 + 2E R^3 t (\psi_0 - \sin \psi_0 \cos \psi_0) \quad (6.23)$$

where it is seen that the full plastic moment $M_p = 4\sigma_y R^2 t$ and the first yield bending moment is given by $M_y = \pi \sigma_y R^2 t$. The above may be rewritten on explicit form in terms of curvature as:

$$M = 4\sigma_y R^2 t \sqrt{1 - \left(\frac{\kappa_0}{\kappa}\right)^2} + 2E R^3 t \left(\sin^{-1}\left(\frac{\kappa_0}{\kappa}\right) - \frac{\kappa_0}{\kappa} \sqrt{1 - \left(\frac{\kappa_0}{\kappa}\right)^2}\right) \quad (6.24)$$

Given the above bending moment M and associated curvature κ , the residual radius κ_r can be determined by first calculating the elastic unloading curvature κ_e given by:

$$\kappa_e = \frac{M}{E \pi R^3 t} \quad (6.25)$$

and

$$\kappa_r = \kappa - \kappa_e \quad (6.26)$$

Pipe sections that have residual curvature may be exposed to torsion instability when the pipe section is exposed to the opposite curvature in the sagbend. This can be evaluated by studying the differential torsion equation for a curved beam as follows, see Figure 6.12:

$$\frac{\partial M_s}{\partial s} - \kappa_n M_t + \kappa_t M_n + m_s = 0 \quad (6.27)$$

where M_s is the torsion moment, κ_n , κ_t , M_n and M_t are respectively the curvatures and moments about curvilinear axes n and t in an arbitrary equilibrium state. m_s is the distributed external torsion moment which is neglected here. The moments and curvatures are taken positive when the components are associated with a positive rotation when moving a small positive distance along the s -axis. By taking the residual state characterised by its curvature κ_{tr} as the reference state and neglecting deformations in the t -direction, the M_n -moment can be expressed as:

$$M_n = EI(-\Delta\kappa_t) \sin \theta_s \quad (6.28)$$

which means that as the pipe is being straightened by an increment the $\Delta\kappa_t$ from state κ_{tr} the moment potential available to cause torsion instability increases. Further by introducing Eq. 6.28 and St.Venant torsion expressed by:

$$M_s = GI_t \frac{\partial \theta_s}{\partial s} \quad (6.29)$$

into Eq. 6.27 and neglecting m_s , the following differential equation is obtained:

$$GI_t \frac{\partial^2 \theta_s}{\partial s^2} - EI\Delta\kappa_t(\kappa_{tr} - \Delta\kappa_t) \sin \theta_s = 0 \quad (6.30)$$

The above differential equation cannot be solved analytically and therefore requires a numerical solution by, e.g. finite differences or finite elements. However, in order to evaluate whether torsion instability is likely to occur or not the differential equation can be modified by introducing the small angle assumption $\sin \theta_s \approx \theta_s$ and Eq. 6.30 is modified into a standard second order differential equation. Introducing $G = \frac{E}{2(1+\nu)}$ and $I_t = 2I$ the differential equation becomes:

$$\frac{\partial^2 \theta_s}{\partial s^2} - (1 + \nu)\Delta\kappa_t(\kappa_{tr} - \Delta\kappa_t)\theta_s = 0 \quad (6.31)$$

It is seen that the solution of the above equation depends on the sign of $\kappa_t - \Delta\kappa_{tr}$. If the pipe still have a positive total curvature then the solution would include hyperbolic functions. If it is zero then a linear function is obtained for θ_s . Assuming $\Delta\kappa_t > \kappa_{tr}$ the general solution is given by trigonometric functions as:

$$\theta_s = C_1 \cos ks + C_2 \sin ks \quad (6.32)$$

where k is defined by:

$$k = \sqrt{(1 + \nu) \Delta\kappa_t(\Delta\kappa_t - \kappa_{tr})} \quad (6.33)$$

Introducing the boundary condition that $\theta_s = 0$ at $s = 0$ and at the end of the span $s = l$ a non-trivial solution requires that $kl = \pi$ which gives the following with respect to the critical curvature increment needed to introduce torsion instability over a certain length l :

$$\Delta\kappa_t = \frac{1}{2}\kappa_{tr}\left(1 + \sqrt{1 + \frac{4\pi^2}{\kappa_{tr}^2 l^2(1 + \nu)}}\right) \quad (6.34)$$

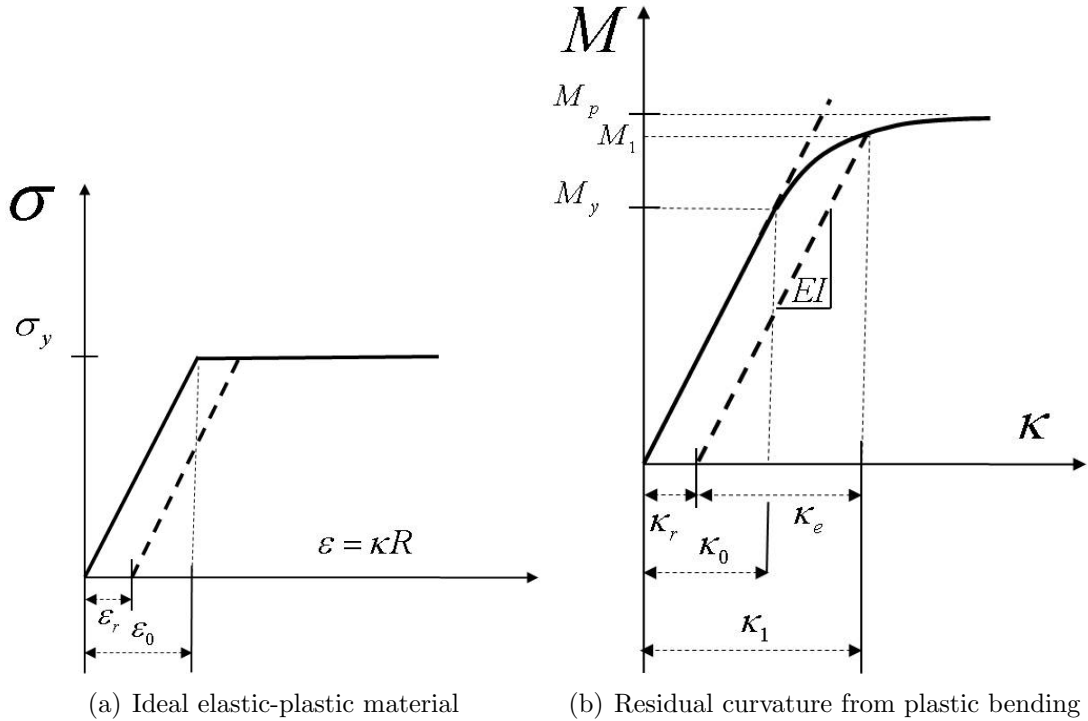


Figure 6.10: Moment-curvature relation

As $l \rightarrow \infty$ it is seen that torsion instability will occur for any negative total curvature i.e. $\Delta\kappa_t > \kappa_{tr}$. Graphs showing the opposite curvature ($\Delta\kappa_t - \kappa_{tr}$) needed to introduce torsion instability as a function of residual curvature radius and suspended length are shown in Figure 6.13.

Example 6.3.1 The above has also been investigated by FE analysis for six cases as defined in Table 6.1 all based on 1000 m suspended length. The theoretical radii of curvature to introduce torsion instability from Figure 6.13 are included.

A 1000 m long pipe was modelled by 100 elastic beam elements and based on first introducing an initial curvature field followed by end bending moments to introduce reversed curvature. A fixed-pinned boundary condition was applied for the ends. Then a restart was carried out where all end DOFs were defined fixed in the end local coordinate systems except the torsion degree of freedom at one end where a prescribed rotation was introduced.

The results are presented in Figure 6.14. A negative torsion stiffness is noted for Cases 2, 4 and 6, indicating that torsion instability occurs. This fits well with the theoretical buckling radii given in Table 6.1 and the expectations from Figure 6.13 obtained by the analytical solution.

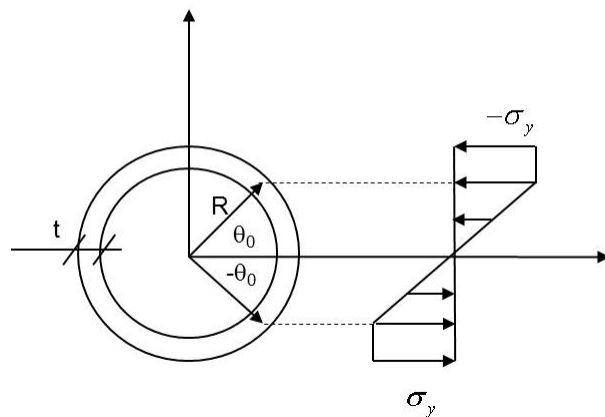


Figure 6.11: Pipe section exposed to bending moment - ideal elastic-plastic material

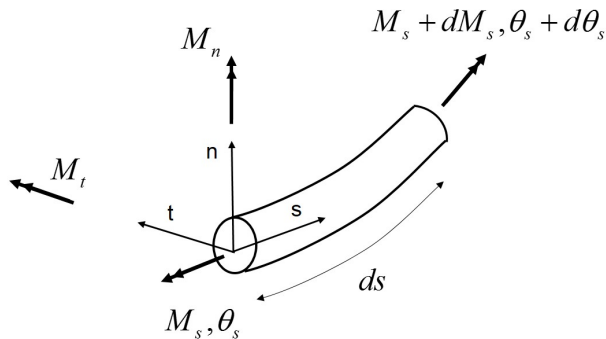


Figure 6.12: Curved beam coordinate system and moments

Table 6.1: ROLL NUMERICAL STUDY DATA

Case	Residual curvature radius(m)	Theoretical buckling radius (m)	Applied curvature radius (m)
1	300	819	2000
2	300	819	819
3	500	517	1250
4	500	517	454
5	1000	434	500
6	1000	434	400

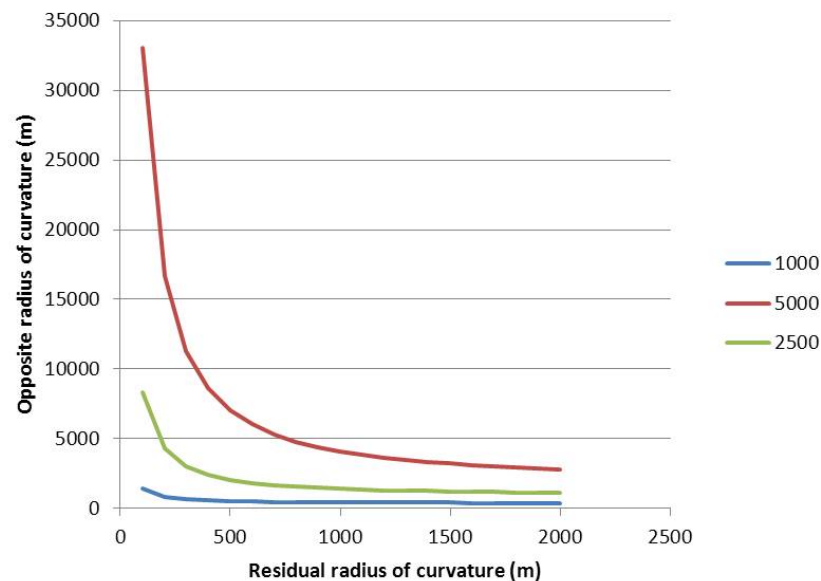


Figure 6.13: Required opposite radius of curvature as a function of residual radius of curvature and suspended length

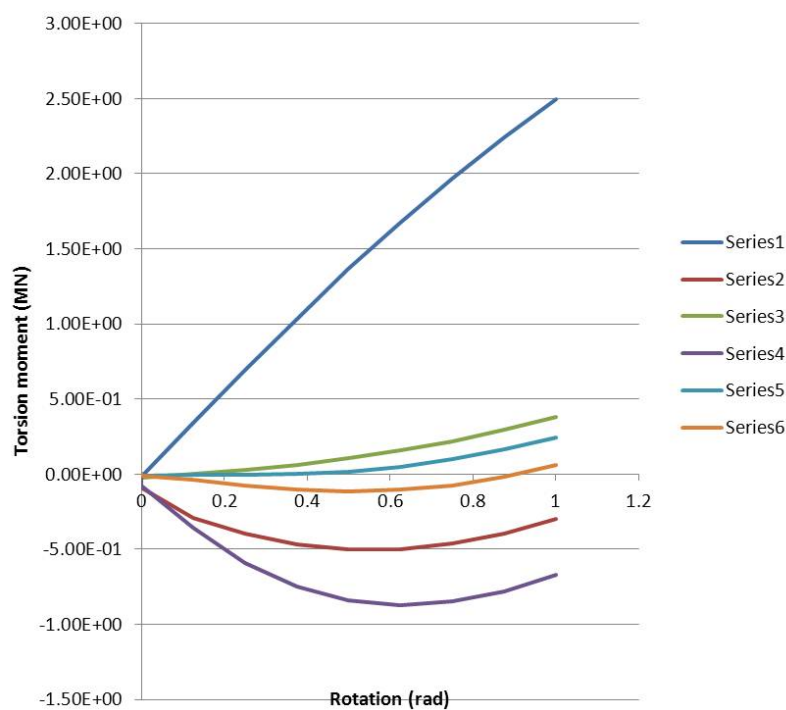


Figure 6.14: Torsion moment versus torsion rotation

Chapter 7

Global buckling

7.1 General remarks

In the following the physical behaviour related to global buckling of pipelines and flexibles will be explained. This is supported by an analytical model that describes the major parameters of the buckling process and a probabilistic study to investigate which parameters that are most important with respect to the upheaval buckling problem for steel pipelines.

7.2 The process of buckling

Pipelines resting on the seabed exposed to a change in internal pressure and flow temperature will try to expand according to the strain given in Eq. 4.17. If no external forces are acting on the pipeline it will just increase its length and no global buckling will take place. The negative force obtained by integrating the internal pressure over the internal area will be balanced by an equal sized tension in the pipe wall needed to keep the content in place, i.e. the *effective* axial force or the total cross section resultant is zero.

However, as illustrated in Figure 7.1 (a), the expansion will be restrained by soil friction, i.e. an external force is introduced into the pipeline until at a certain point, the accumulated axial force P completely restrains the expansion, i.e. $\epsilon_{xx} = 0$ in Eq. 4.17 ($P = EA_p\epsilon_{xx}$). The length needed by axial soil friction to mobilize this force is termed the virtual anchor length L_a given by:

$$L_a = \frac{P}{\mu_x w_s} \quad (7.1)$$

and due to the linear strain field the end expansion Δ_x is determined as:

$$\Delta_x = \int_0^{L_a} \epsilon_{xx} dx = \frac{PL_a}{2EA_p} = \frac{P^2}{2\mu_x w_s EA_p} \quad (7.2)$$

Since an external load now acts on the pipeline, Euler buckling may take place at a certain initiation axial force level P_i . If this occurs, the force will drop to a certain level determined by the Euler buckling load P_E corresponding to the geometry and boundary conditions, as illustrated in Figure 7.1 (b). Transverse buckling requires a certain feed-in of pipe from the neighbouring sections, Δ_x . This process mobilises axial friction that cause a linear axial force increase away from the buckle, until sufficient axial force to initiate the next buckle is introduced. The axial force needed to start the buckling process depends on the imperfection size, determined by seabed irregularities, pipe out of straightness etc. The less imperfection, the higher load P is needed to generate a new buckle. Hence, the force drop $\Delta P = P - P_E$, the associated feed-in Δ_x , the transverse displacement and bending moment at the apex of each buckle will tend to increase for small imperfection sizes. Therefore, if no action is taken, detrimental buckling that exceeds the bending moment capacity of the pipeline, is more likely to occur in flat seabed areas than in irregular sea areas as the latter will introduce large natural imperfections that act as triggers for the

buckling process, thus ensuring that the expansion potential is shared among more buckles than for the flat seabed case.

For pipelines that are left exposed on the seabed, the buckling process may take place as a combination of vertical and transverse buckling. This is typically the case in irregular seabed areas. First the pipe will lift upwards at the local maxima, i.e. at the imperfection apex, then after loosing contact over a certain length, the bending plane is shifted and the pipe starts to deform horizontally. Global buckling of pipelines left exposed on the seabed as illustrated in Figure 7.2 (a) is often termed *snaking*. For buried pipelines, horizontal displacements will be restrained by the soil, and the buckling process therefore only takes place in the vertical direction. This is normally referred to as *upheaval buckling*, see Figure 7.2 (b).

There are two design principles in use to deal with such behaviour:

- For pipelines exposed on the seabed, allow the pipe to buckle in a controlled manner
- Restrain the pipeline from buckling

The latter principle may be applied for both buried and exposed pipelines. In the buried *upheaval buckling* case, the major design issue is to ensure sufficient soil cover to avoid buckling, normally by rock installation at the imperfections. In the exposed case this can be obtained by several methods, including rock installation and weight coating. In both cases, eventual buckling may cause the pipeline to collapse in bending, due to the large transverse soil reaction force and the associated large bending moment at the buckle apex. To ensure sufficient safety against global buckling is therefore crucial. Further, since the buckling load is sensitive to imperfections, pipeline survey efforts to measure the imperfection geometry are normally carried out to optimise the design in such cases.

In order to capture all non-linearities related to soil-interaction and material behaviours, FE analysis is normally required. A lot of efforts have been made in order to obtain standardised procedures for such analyses to capture all relevant effects. [DNVGL, 2007] gives detailed instructions on how perform such analyses and document that the design criteria are fulfilled. This has been based on the works by many authors such as [R.E.Hobbs, 1984], [Gijjt, 1990], [Putot and Rigaud, 1990], [Sævik and Levold, 1995a], [Sævik and Levold, 1995b] and [Nes et al., 1996].

Important into this is the issue of soil modelling which has been an important part of the *Safebuck JIP*, see [Carr et al., 2006], [D.Brunton et al., 2006] and [D.Brunton et al., 2008]. This is particularly relates to the vertical soil resistance model used in upheaval buckling analyses and the lateral transverse soil resistance used in snaking analyses of pipelines resting on the seabed. With respect to the latter case, the cyclic behaviour due to temperature variations lead to large amplitude lateral displacements. In cohesive soils (clay) this may cause build up of soil berms that gives increased resistance during subsequent cycles, see [D.Brunton et al., 2006]. This may increase the moment at the buckle apex.

Flexible pipes have a low bending stiffness. Hence the imperfections needed to trigger buckling are therefore smaller than for steel pipelines and the length needed to create a new

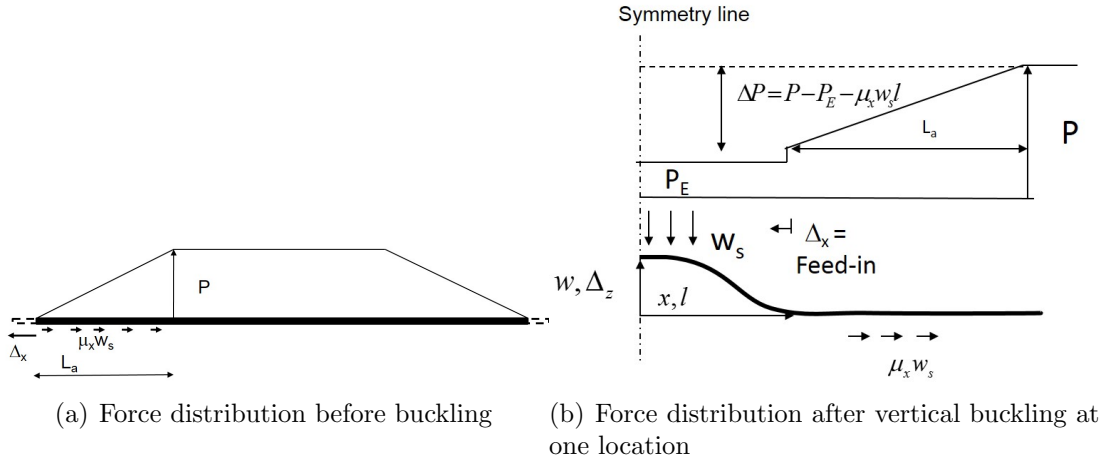


Figure 7.1: Axial force distributions before and after vertical buckling

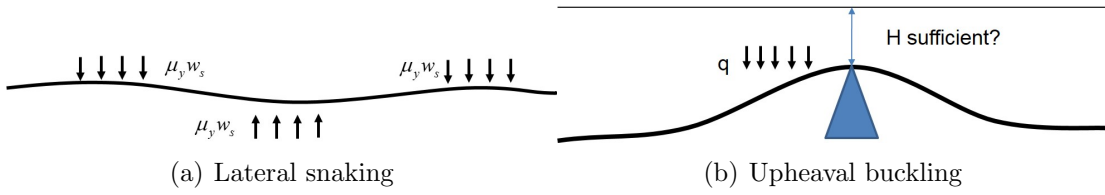


Figure 7.2: Buckling modes

buckle shorter. Normally, flexible pipes need to be buried to provide mechanical protection. In order to ensure equal sharing of the temperature and pressure displacement potential, the pipes are normally pressurised to hydrostatic pressure during the burial process. Then the pipe will rest in a prestressed condition restrained from moving back to the initial configuration, thus acting to reduce the additional displacement from temperature during the operating condition. The design criteria will then be to ensure that the maximum allowable curvature is not exceeded, see e.g. [Putot and Rigaud, 1990]. Since the bending stiffness of a flexible pipe is sensitive to the internal pressure and temperature conditions, this has to be included in FE analyses, see [Fergestad and Løtveit, 2014].

7.3 Analytical global buckling model

By considering the infinitesimal element in Figure 7.3, assuming small angles θ , and considering equilibrium in moment about the left end:

$$(Q + dQ)dx + Pdw - q\frac{1}{2}dx^2 - (M + dM - M) = 0 \quad (7.3)$$

$$Q = \frac{dM}{dx} - P\frac{dw}{dx}$$

Further by considering equilibrium in z direction:

$$(Q + dQ - Q)dx - qdx = 0 \quad (7.4)$$

$$\frac{dQ}{dx} = q$$

by introducing that $M = -EI\frac{d^2w}{dx^2}$, where EI is the bending stiffness, the following differential equation is obtained:

$$EI\frac{d^4w}{dx^4} + P\frac{dw^2}{dx^2} = -q \quad (7.5)$$

$$\frac{d^4w}{dx^4} + k^2\frac{dw^2}{dx^2} = -\frac{q}{EI}$$

where $k^2 = \frac{P}{EI}$. The solution constituting both the homogeneous and particular solutions can be written as:

$$w = w_h + w_p = C_1 + C_2x + C_3 \cos kx + C_4 \sin kx - \frac{qx^2}{2P} \quad (7.6)$$

As seen from (7.5) the external resistance q on the right hand side is respectively balanced by bending and membrane terms on the left hand side. If the pipe is straight and rests on a rigid and flat foundation, the pipe will resist loads by membrane action alone, through the development of axial stresses. However, if imperfections are introduced, there will be a driving force represented by the membrane term which is balanced by the bending and the external resistance terms. This is realised by the fact that the above homogeneous solution will cause the bending term to be positive whereas the membrane term will be negative. The membrane term will then act to increase the required vertical transverse resistance whereas the bending term will act to reduce it. Further, if the pipeline is buried, the lateral resistance tends to be large. Therefore, if global buckling is allowed to occur, this may cause localized bending at the imperfection apex with associated large strains possibly leading to collapse by local buckling. This is a fundamental feature in upheaval buckling response and this needs to be considered carefully when deciding on cover depth and safety margins.

The axial shortening of the beam along the w displaced section is obtained by studying the shortening due to the angular deformation and assuming small angles .i.e.

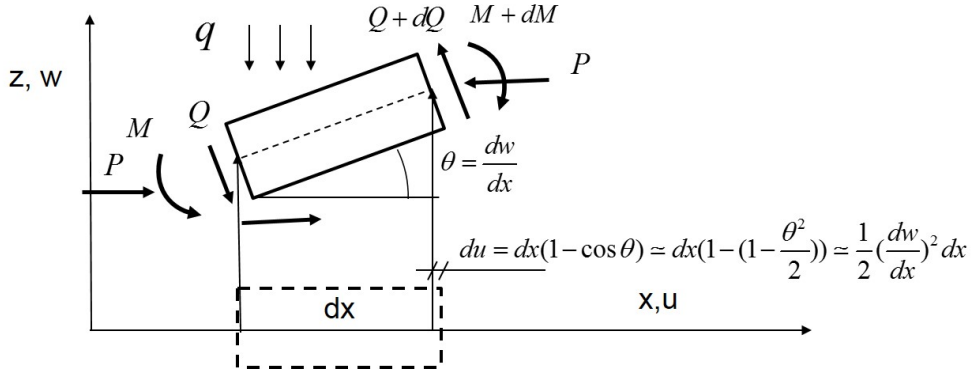


Figure 7.3: Infinitesimal pipe element

$$du = dx(1 - \cos \theta) \simeq dx(1 - (1 - \frac{\theta^2}{2})) \simeq \frac{1}{2}(\frac{dw}{dx})^2 dx$$

$$\Delta_x = \int_0^l du = \frac{1}{2} \int_0^l (\frac{dw}{dx})^2 dx \quad (7.7)$$

The axial shortening Δ_x requires that pipe is fed into the buckle from the neighbouring sections. Since the strain distribution is linear we again have:

$$\Delta_x = \int_0^{L_a} \epsilon_{xx} dx = \frac{\Delta PL_a}{2EA_p} = \frac{\Delta P^2}{2\mu_x w_s EA_p} \quad (7.8)$$

By equating Eq. 7.7 with Eq. 7.8, the force P needed to keep a certain equilibrium configuration described by it's Euler buckling load P_E is obtained.

It is however, noted that the differential equation assumes elastic material properties, uniform soil reactions and idealised boundary conditions. In practise, non-linear finite element analysis is required in most cases to include all relevant physical effects and to document the pipeline thermal performance versus relevant failure modes.

Example 7.3.1 Buckling in vertical direction, first mode The task is to find the axial force P needed to keep a certain buckling configuration in equilibrium considering the first vertical symmetric mode with the boundary condition illustrated in Figure 7.4 where the last boundary condition (5) gives the Euler load P_E . The following results are obtained:

Boundary conditions:

$$1: \frac{dw}{dx} \Big|_{x=0} = 0$$

$$2: \frac{dw}{dx} \Big|_{x=l} = 0$$

$$3: w \Big|_{x=l} = 0$$

$$4: \frac{d^2w}{dx^2} \Big|_{x=l} = 0$$

$$5: Q \Big|_{x=0} = 0$$

Symmetry line

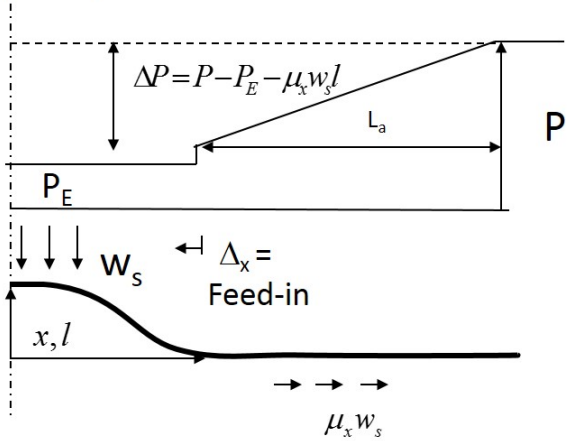


Figure 7.4: First vertical buckling mode

$$1: \Delta_z = 15.7 \frac{w_s EI}{P_E^2} = 0.0385 \frac{w_s l^4}{EI}$$

$$2: P_E = 20.25 \frac{EI}{l^2} = 3.98 \sqrt{\frac{w_s EI}{\Delta_z}}$$

$$3: M_y \Big|_{x=0} = M_{\max} = 5.6 \frac{w_s EI}{P_E}$$

$$4: Q_z \Big|_{x=l} = ql$$

$$5: \Delta_x = 37.4 \frac{w_s^2 EI^{3/2}}{P_E^2}$$

Kinematic compatibility is introduced by equating the Δ_x obtained from Eq. 7.3.1 with the result from Eq. 7.8. The load P needed to keep the buckle shape is then obtained as:

$$P = 20.25 \frac{EI}{l^2} + \mu_x w_s l + 4.52 \cdot 10^{-2} \frac{w_s}{EI} \sqrt{EA\mu_x w_s l^7}$$

By expressing P as a function of e.g. the buckle half length l , a minimum in P will be reached. If the combined action of pressure and temperature along the pipeline (obtained from $P = EA_p \epsilon_{xx}$ using Eq. 4.17) gives less potential expansion force than corresponding to this minimum value, no vertical buckling takes place. However, this will normally give a low temperature compared to the actual one, specially for high temperature and pressure flowlines and and FE analyses would be needed to capture the inherent non-linearities.

Example 7.3.2 Buckling in horizontal direction For horizontal buckling the weight of the buckled section cannot be carried as a pointload at the end. Therefore it is more realistic that the buckle configuration will take place in three waves as illustrated in Figure 7.5 which includes the selected boundary conditions.

Key results are:

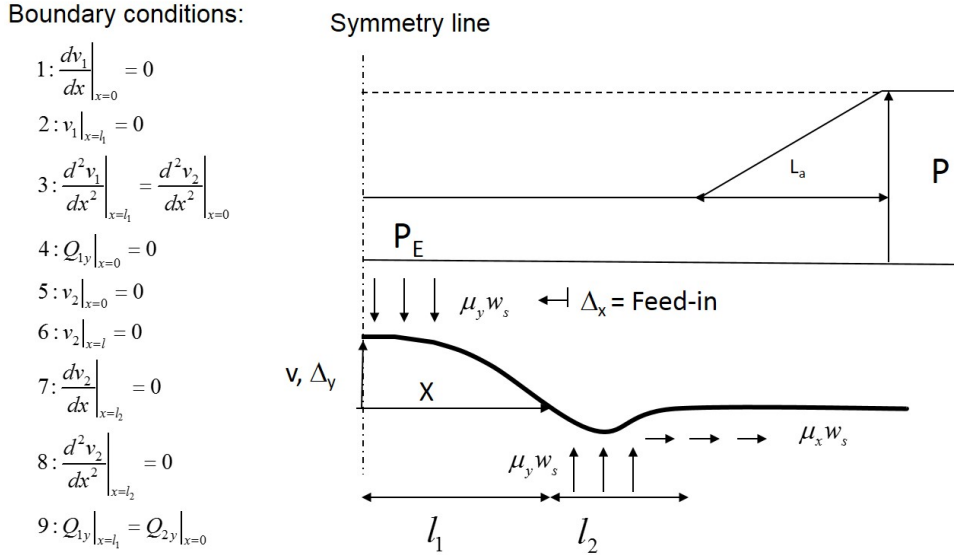


Figure 7.5: Three wave horizontal buckling mode

$$\begin{aligned}
 1 : \Delta_y &= 11.94 \frac{\mu_y w_s EI}{P_E^2} \\
 2 : P_E &= 3.45 \sqrt{\frac{\mu_y w_s EI}{\Delta_y}} \\
 3 : M_z \Big|_{x=0} &= M_{\max} = 4.89 \frac{\mu_y w_s EI}{P_E} \\
 4 : \Delta_x &= 32.54 \frac{\mu_y^2 w_s^2 EI^{3/2}}{P_E^2}
 \end{aligned}$$

Kinematic compatibility is introduced by equating the Δ_x obtained from Eq. 7.3.2 with the result from Eq. 7.8. The load P needed to keep the buckle shape is then obtained.

By expressing P as a function of e.g. the buckle half length l , a minimum in P is reached. If the combined action of pressure and temperature along the pipeline gives a fully restrained compressive axial force (obtained from $P = EA_p \epsilon_{xx}$ using Eq. 4.17) that is less than this minimum value, no horizontal buckling takes place. As noted above, however, this will often correspond to a low temperature compared to the actual one and in that case FE design analyses would be needed to investigate the structural behaviour including non-linear material, pipe profile and soil interaction effects in more detail.

Chapter 8

Mechanical behaviour of flexible pipes

8.1 General remarks

The understanding of pipe performance characteristics and related failure modes is important for obtaining a reliable design of flexible pipe systems. The experience gained from flexible pipe applications over the last two decades has identified a significant number of failure modes. The performance with respect to these failure modes may be determined by the use of analytical and computational methods in combination with testing procedures, see [Fergestad and Løtveit, 2014]. Here an overview of the most important aspects related to the mechanical performance of the flexible pipe including design of the steel layers is given.

A detailed description of experienced failure modes and test methods are found in Section A3 and Section B5, respectively.

With reference to [API, 2008a], design of flexible pipes is carried out in stages:

- Material selection considering the temperature and chemical conditions in terms of pH (sweet or sour service).
- Cross-section configuration design based on what to be transported (gas, oil, water) and at which pressure rating.
- System configuration design based on the surrounding infrastructure and environment.
- Dynamic analysis design, identifying the curvature and tension extreme responses.
- Detail and service life design verifying that sufficient service life is obtained.
- Installation design, ensuring that the pipe can be safely installed.

The cross-section strength is governed by the steel helix layers and the design analyses used to define the amount of steel needed are normally carried out according to the requirements of [API, 2008b] which applies the *allowable stress format*. This means that a load condition specific utilization factor is applied to the yield stress defining a stress limit that is not to be exceeded. The cross-section design analysis is normally based on the pressure rating and use of analytical models considering axisymmetric effects alone (internal and external pressure, tension and torsion) and based on the mean stress approach. The latter means that only stresses due to the axial load in the wires are included when calculating the stresses. Secondary stresses in the wire due to bending and friction is not included. This relies on the assumption that the flexible pipe is a compliant structure where the secondary stresses can be taken care of by introducing a maximum curvature limit to ensure that no over bending takes place.

This section focus on methods for analysis and design of non-bonded flexible pipes with respect to known metallic layer failure modes that can be described by analytical or computational methods and are part of the design requirements reflected in [API, 2008b]. The failure modes addressed here are:

- Overload, i.e. excessive yielding in the metallic layers.
- Collapse of the cross-section due to external pressure.
- Buckling.
- Metal fatigue.
- The effect of corrosion on metal fatigue and tensile armour buckling.

Analytical formulas are included for estimation of mechanical properties and structural capacities for specific cases. These formulas are primarily given for verification purposes, enabling capacity and performance parameters to be calculated in a simplified way and under specific conditions.

8.2 Governing stress components

The nonbonded flexible pipe consists of a layered structure where each layer is free to slide (under the restraint of friction) relative to each other. Each layer has its specific function as described in Section A2.

A typical *rough bore* flexible pipe consists of (starting from the inside):

- The carcass which consists of a flat steel strip, formed into a corrugated profile preventing collapse induced by external pressure, installation loads and gases in the annulus. The carcass is not leak tight and it therefore does not contribute to resisting internal pressure. It is further noted that the design is based on assuming that the annulus between the outer sheath and the pressure bore is water filled, implying that the full water pressure must be sustained by the carcass alone. The other layers may contribute in terms of providing some support, however, depending on the magnitude of gap formation between the carcass and the other layers.
- The Pressure Barrier, providing a pressure tight barrier for the internal content and the external water
- The Pressure Spiral, providing support of the pressure barrier, resisting the internal pressure and also supporting the carcass with respect to resisting external pressure. The pressure spiral wire may consist of 1-2 wires in 1-2 layers with a lay angle α close to 90° .



Figure 8.1: Flexible pipe cross-section

- The tensile armour, providing strength with respect to tension, torque and the pressure end-cap force. Normally two cross-wound layers are applied to ensure torsion balance, each layer consisting of 30-80 rectangular steel wires with a lay angle α in the range $+/- 29^\circ - +/- 55^\circ$. A positive lay angle is taken to be according to the right hand rule. The layers are normally separated by anti-wear layers to avoid metal contact and possible wear and fretting wear.
- The external sheath, designed to avoid sea water ingress and sea water corrosion.

In order to understand the mechanical behaviour of flexible pipes it is important to clarify which layers and stress components that contribute. In the general case, the stress components include 3 normal stress components σ_{11} , σ_{22} , σ_{33} and 3 shear stress components σ_{13} , σ_{23} , σ_{12} , see Figure 8.2

The load response is primarily governed by the steel layers, however, the plastic layers influence how the load is shared between the layers. This is exemplified in Figure 8.3 showing how internal pressure is transferred throughout a typical flexible pipe cross-section. This pipe cross-section includes starting from the inside; the carcass, a pressure sheath, pressure spiral wires in two layers, 4 layers of cross-wound tensile armour separated by antiwear tapes and an external sheath.

It is seen that the carcass do not carry pressure (pressure on inside and outside of carcass is the same), due to its corrugated structure. The plastic layers are in this example assumed to have a Poisson's ratio of 0.5. Hence, these layers behave hydrostatic (same stress in all three directions) and the contact pressure (starting from internal pressure at the outside of

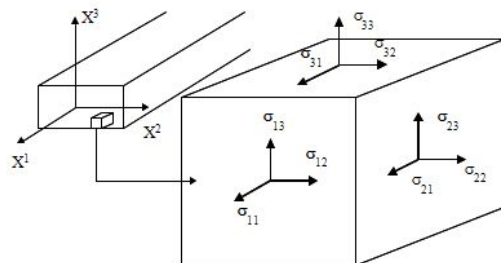


Figure 8.2: General components of stress

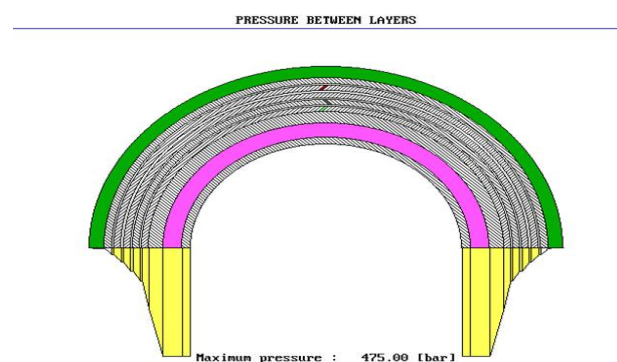


Figure 8.3: Pressure distribution in a typical flexible pipe exposed to internal pressure

carcass) is seen to be transformed directly to the next steel layer. The contact pressure from the tensile armour onto the pressure spiral wire results from the end-cap effect (tensioning the tensile armour) and act as a support of the two pressure spiral wire layers, reducing the associated pressure differential that need to be taken by the pressure spiral wires.

From the above it is clear that the stress state in each layer of a flexible pipe is in nature 3-dimensional, however, since the steel layers are governing with respect to structural strength and these consists of long slender helical beams, the primary stress component to be included in strength calculations will be the axial stresses resulting from the axial load in each wire.

The wires are further normally assumed to rest stress free in the helix configuration as the manufacturing procedure involves plastic strains in the helices. With reference to Figure 8.4 (a), this results in an initial torsion κ_1 and an initial normal curvature κ_2 whereas $\kappa_3 = 0$ along the helix. Hence, curved beam theory that include the coupling between initial curvature, membrane and bending effects is needed to describe the structural behaviour. The stresses are related to the governing stress resultants defined in Figure 8.4 (b) and the load scenario, which can be divided into:

- Axisymmetric loads that only change the length and diameter of the straight pipe cylinder and with small relative deformations between wires. This includes tension, torsion, internal and external pressure loads, the latter assuming that no local buckling or collapse effects occur.
- Bending loads where the straight pipe cylinder is bent into a torus and where significant relative deformations will occur between the wires.

The significant stress components are shown in Figure 8.5 and include components from axial force, torsion moment and bidirectional bending. The components of shear stresses σ_{12} and σ_{13} related to the local shear forces Q_2 and Q_3 are small and can be neglected.

For axisymmetric loads, the stresses related to torsion and bending are insignificant, hence the stresses resulting from the axial load in the wire will govern. It is noted that for non-symmetric pressure spiral wires, such as the Z-spiral, significant stresses may result from rotation as a result of the M_3 moment about the strong radial axis resulting in a significant stress gradient along the cross-section, see Figure 8.5 (b). However, since the spiral wire will be locked when the gaps are closed, these stresses are not essential for equilibrium and can be neglected in static strength calculations. This is one of the reasons why [API, 2008a] refers to the concept of *mean stress* when dealing with strength calculations, i.e. neglecting the contribution from the bending moment resulting in each wire. It is noted that this approach rests on the assumption that the steel material used have sufficient fracture toughness to accommodate the involved strain level and where the minimum allowable curvature radius will represent the limiting criteria with respect to controlling the total strain involved for each load case.

For bending fatigue calculations, the axial, torsion and bending components need all to be included for both the tensile and pressure armours. In the latter case, the bending process also gives variation in σ_{22} , σ_{23} and σ_{33} that need to be taken into account, see Section 8.5

8.3 Wire geometries

The tensile armour consists of flat rectangular profiles, with rounded corners to create a smooth profile thus avoiding notch effects. For each layer, all wires are simultaneously cold formed onto the pipe surface, 40 – 80 wires in each layer at lay angles 29° – 55° . The fraction filled ratio F_f is usually around 0.9. For the tensile armour, the fill factor is defined by:

$$F_f = \frac{nb}{cos\alpha 2\pi R} \quad (8.1)$$

where n is the number of tendons in the layer, b is the width of the tendon, R is the mean layer radius and α is the lay angle. The applied wire dimension depends on the pipe diameter, some typical thickness/width mm values are 3/7.5, 5/17.5, 4/17.5, 6/12 and 6/15.

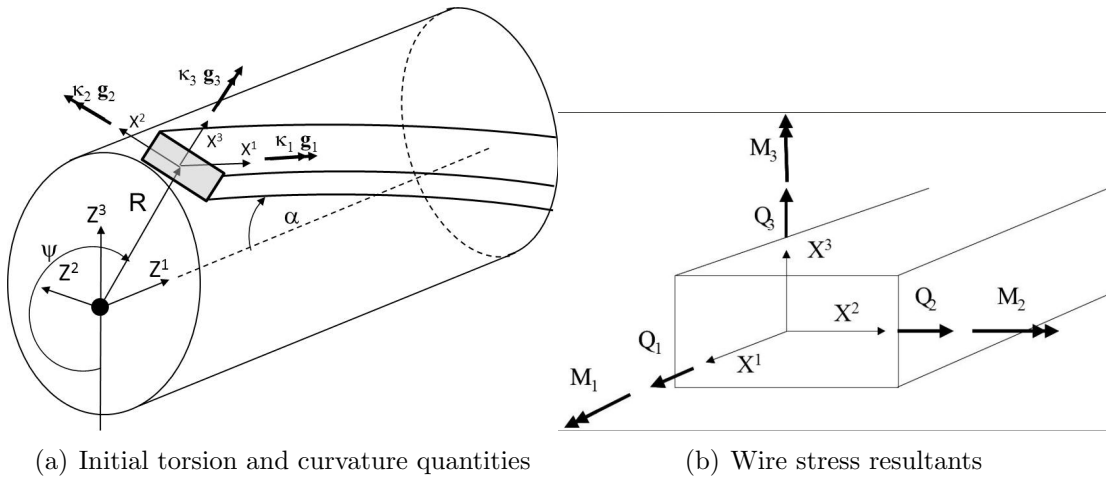


Figure 8.4: Definition or wire coordinate axes and mechanical quantities

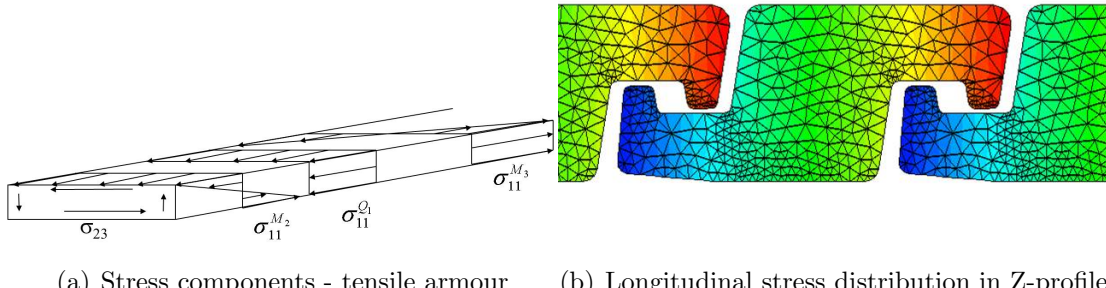


Figure 8.5: Stress components in armour wires

The pressure armour consists of interlocked spiral wires, normally 1-2 spiral wires per layer in 1-2 layers. The different manufacturers supply different geometries such as the Z-spiral, the C-clip and the Theta-clip. For high pressure applications a rectangular back up spiral wire may be applied to increase the pressure capacity. The fraction filled ratio is normally in the range of 0.85 for these layers. For the pressure armour and carcass, the fill factor is normally defined by:

$$F_f = \frac{nA}{L_p t} \quad (8.2)$$

where L_p is the pitch length of the n spiral wires in the layer (normally 1 or 2) with cross-section area A . Different wire configurations are illustrated in Figure 8.6. The pitch length is defined as:

$$L_p = \frac{2\pi R}{\tan \alpha} \quad (8.3)$$

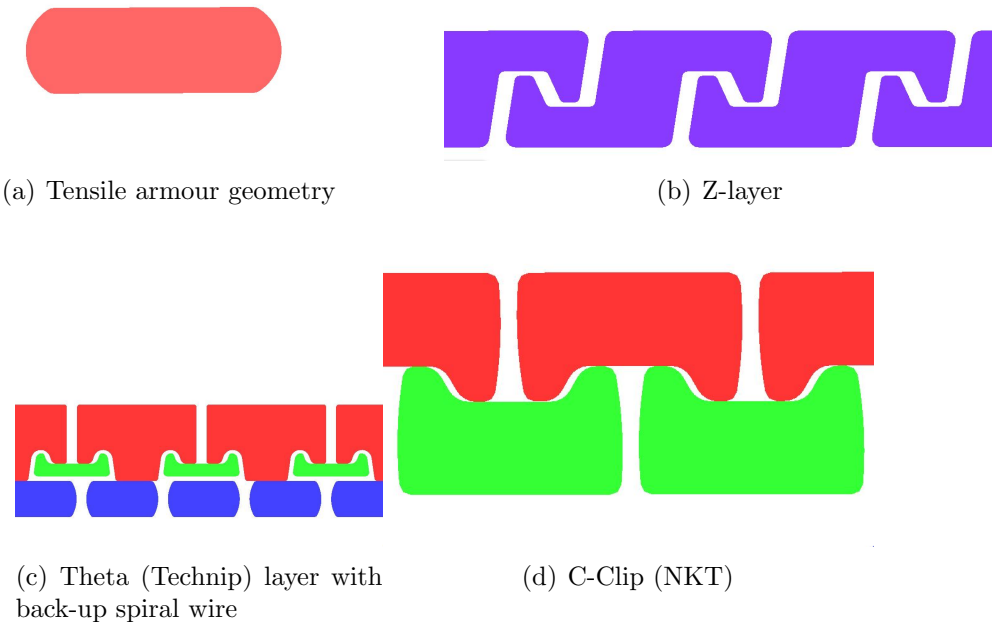


Figure 8.6: Tensile armour profile and alternative pressure spiral wire configurations

The carcass is manufactured from a flat steel plate and formed into a corrugated profile as illustrated in Figure 8.7. A typical fill factor is 0.55.

8.4 Behaviour due to axisymmetric loads

8.4.1 General

In this section, the behaviour due to axisymmetric loads, i.e. i.e. tension, torsion, internal and external pressure loads will be explained in terms of an analytical approach assuming that the cylindrical straight pipe shape is kept during deformation. It is noted that with respect to external pressure loads this assumes that no local buckling or collapse effects will occur. Buckling effects are treated separately in Section 8.6.

As noted above, the response due to axisymmetric loads are primarily governed by the response of the metallic layers which all consist of helices. The wires are normally assumed to rest stress free in the helix configuration as the manufacturing procedure involves plastic strains. With reference to Figure 8.4, the initial torsion κ_1 and curvatures components κ_2 and κ_3 along the helix can be expressed by the lay angle α and the helix radius R as:

$$\kappa_1 = \frac{\sin \alpha \cos \alpha}{R} \quad (8.4)$$

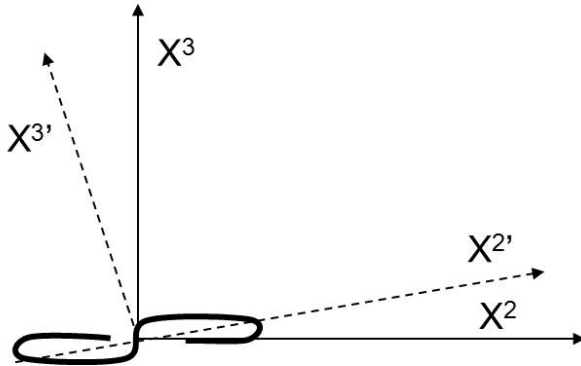


Figure 8.7: Carcass corrugated profile - principal outline

$$\kappa_2 = \frac{\sin^2 \alpha}{R} \quad (8.5)$$

$$\kappa_3 = 0 \quad (8.6)$$

The long and thin wires can be described by curved beam theory and the wire equilibrium equation when only considering axisymmetric loads can be written as [Sævik, 2011]:

$$-\kappa_2 Q_1 + \kappa_1 Q_2 + q_3 = 0 \quad (8.7)$$

$$-\kappa_2 M_1 + \kappa_1 M_2 + Q_2 = 0 \quad (8.8)$$

where Q_i and M_i respectively represent the forces along and moments about the X^i axes defined in Figure 8.4 and q_3 is the contact line load in the radial direction. For the slender armour wire, the contribution from M_i and Q_2 is small and can be neglected. This means that wire equilibrium can be described by the axial load Q_1 alone. The contact pressure line load q_3 is then obtained from Eq. 8.7 and Eq. 8.5 as:

$$q_3 = \kappa_2 Q_1 = \frac{\sin^2 \alpha}{R} Q_1 \quad (8.9)$$

8.4.2 Axial loading

Primary effects

By considering all steel layers and neglecting the contribution from the plastic layers, pure axial equilibrium yields:

$$\sum_{j=1}^{N_a} n_j \sigma_{11j} A_j \cos \alpha_j = T_p = T + \pi p_{int} R_{int}^2 - \pi p_{ext} R_{ext}^2 \quad (8.10)$$

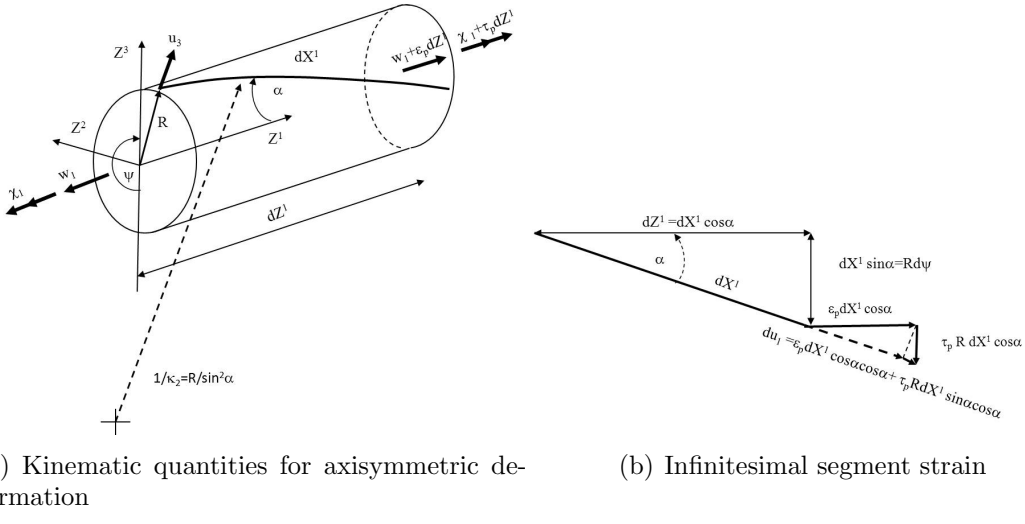


Figure 8.8: Definition of kinematic quantities - axisymmetric loading

where N_a is the number of contributing layers, T_p is the true wall tension, n_j is the number of wires in layer j , σ_{11j} is the axial stress in the layer, A_j is the wire cross-section area, T is the effective tension (the total cross-section resultant), p_i is the internal pressure and p_e is the external pressure. It seen that since the lay angle of the pressure spiral wire is close to 90° , the axial load is primarily taken by the tensile armour layer.

For a two layered cross-wound structure where the lay angles are assumed to be equal in size but opposite in lay direction (balanced), the below formulas can be used to estimate the stresses in the tensile armour.

$$\sigma_t = \frac{T_p}{nA_t \cos\alpha} = \frac{T_p}{2\pi R t_{tot} F_f \cos^2\alpha} \quad (8.11)$$

where n is the total number of tensile armour wires, A_t is the area of the wire, t_{tot} is the thickness including both layers and F_f is the fill factor. By assuming same fill factor and number of tendons for the two layers, the nominal external pressure from the tensile armour layer onto the pressure spiral wire can further be approximated by:

$$p_t = 2 \frac{q_3}{b} F_f = 2 \frac{\sigma_t A_t \sin^2 \alpha}{R b} F_f = 2 \frac{T_p}{2n_j \cos\alpha} \frac{\sin^2 \alpha}{R b} \frac{n_j b}{\cos\alpha 2\pi R} = \frac{T_p \tan^2 \alpha}{2\pi R^2} \quad (8.12)$$

where R is taken to be the mean layer radius.

With reference to Figure 8.8, the axial strain in the helix can be described by standard beam quantities at the cross-section centre and the radial motion u_3 of each layer as:

$$\epsilon_{11} = \cos^2 \alpha \epsilon_p + \frac{\sin^2 \alpha}{R} u_3 + R \sin \alpha \cos \alpha \tau_p \quad (8.13)$$

where ϵ_p and τ_p are the overall pipe strain and torsion at the pipe centre, cfr. Figure 8.8. The axial stiffness of the two layered pipe can then be obtained by assuming no torsion coupling, i.e. neglecting the last term in Eq. 8.13 and using energy principles as:

$$EA = nEA_t \cos \alpha (\cos^2 \alpha - \nu_a \sin^2 \alpha) = 2\pi R t_{tot} F_f E \cos^2 \alpha (\cos^2 \alpha - \nu_a \sin^2 \alpha) \quad (8.14)$$

where ν_a is the apparent Poisson's ratio defined by the relation between axial and radial strain:

$$\nu_a = -\frac{u_3}{R\epsilon_p} \quad (8.15)$$

The first term in Eq. 8.14 describes the stiffness contribution from the tensile armour, whereas the second term describes the softening effect of the radial contraction associated with the helix. For nonbonded pipes with a stiff pressure armour and carcass, $\nu_a \sim 0.2$. Consequently, the first term in the stiffness expression in Eq. 8.14 dominates. It should also be noted that the expression in Eq. 8.14 assumes small geometric deformations and that the layers remain in contact. The last assumption signifies that initial gaps introduced during fabrication or due to the load condition may influence the axial pipe stiffness significantly. This is particularly the case for compressive axial loads.

Figure 8.9 shows experimental results on the axial load -relative elongation behaviour of an 8m long 4" smooth bore dynamic pipe, [Skallerud, 1991a], with zeta layer and pressure back-up layer. The results are presented for different levels of internal pressure and signify:

- Relatively little hysteresis
- Axial stiffness ranging from 11.05-21.05 MN, depending on internal pressure

Figure 8.10 indicates that increasing frequency increases the hysteresis, but the stiffness is not significantly affected. The discontinuity at the loop ends are due to resolution problems at the high frequency, and is not a physical effect of the pipe. It is likely that the hysteresis seen for high frequencies is caused by visco-elastic effects induced by the plastic layers.

The results showed that a linear relation can be assumed between axial force and strain with an associated equivalent damping ratio less than 3 % for the tested pipe.

For a given design, ν_a can also be calculated based on information given in terms of the axial strain at a given internal pressure and the axial stiffness. The axial strain at a given pressure ϵ_p can be approximated as:

$$\epsilon_p = \frac{(1 - 2\nu_a)p_{int}\pi R_{int}^2}{EA_p} \quad (8.16)$$

which can be used to find ν_a , in most cases giving the same value of ~ 0.2 for the standard non-bonded pipe (not 55° designs with no pressure spiral wire).

Existing methods for the determination of pipe response to axial tension are fairly reliable. However, this is not the case for axial compression, which is a more complex

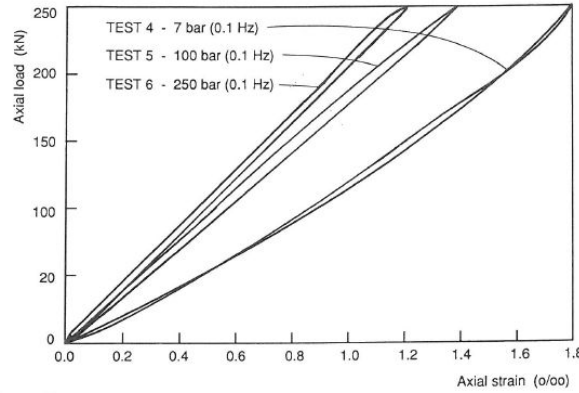


Figure 8.9: Axial elongation behaviour of a 4" pipe. Loading frequency = 0.1 Hz, [Skallerud, 1991a]

area. During installation and shut-down conditions where the pipe bore may be exposed to external overpressure, the tensile armour will be in compression, even if the effective tension is positive. This may lead to radial gaps followed by radial or transverse buckling of the tensile wires, leading to overall torsion instability. For deep water pipe designs, anti-buckling tapes may be applied on the outside of the outer tensile armour to limit the radial motions and formation of gaps. The instability failure mode was reported by Bectarte and Coutarel [Bectarte and Coutarel, 2004] describing both bird caging (radial failure) and lateral buckling. Test procedures for lateral buckling were described that included the effect of cyclic bending. A computer model was also mentioned, but no details with respect to methods or results were given. The methods used to validate the pipe capacity with respect to this failure mode include laboratory testing, Deep water Immersion Performance (DIP) testing and mathematical models. Reference is given to Section 8.6.

Bending and torsion in the wire due to axial wire loads

The change in lay angle induced by the beam deformation quantities also leads to small changes in the curvature of the wire about the weak axis of the wire and torsion. These quantities can be approximated by [Sævik, 1992]:

$$\omega_1 = \frac{\sin^3 \alpha \cos \alpha}{R} \epsilon_p - \frac{\sin^3 \alpha \cos \alpha}{R^2} u_3 + \cos^4 \alpha \tau_p \quad (8.17)$$

$$\omega_2 = -\frac{\sin^2 \alpha \cos^2 \alpha}{R} \epsilon_p + \frac{\sin^2 \alpha \cos^2 \alpha}{R^2} u_3 + (2 \sin \alpha \cos^3 \alpha + \sin^3 \alpha \cos \alpha) \tau_p \quad (8.18)$$

where ω_1 represents the change in torsion and ω_2 is the change in normal curvature. As noted above, the contribution from the above quantities can normally be neglected

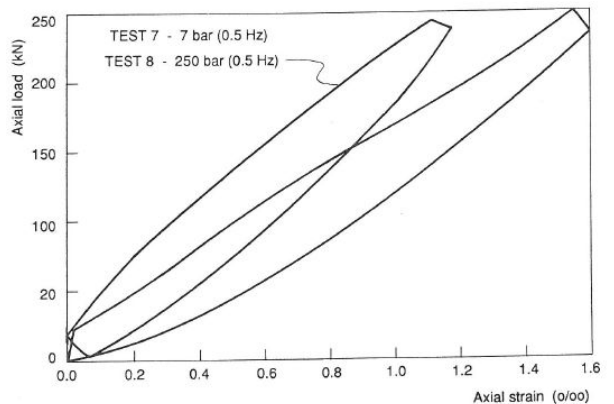


Figure 8.10: Axial elongation behaviour of a 4" pipe. Loading frequency = 0.5 Hz, [Skallerud, 1991a]

due to the small tensile armour cross-section and the limited overall axial strain allowed for in flexible pipes. It should, however, be noted that for torsion unbalanced structures consisting of large helical elements, the contribution is significant and should be included. The above equations have been compared to FE analysis and are considered valid as long as the helix lay angle is not significantly altered.

The above expressions have been compared to results from FE analyses and are considered valid as long as the helix lay angle is not significantly altered.

Bending stresses induced by axial wire loads at end fittings

Axisymmetric loads is associated with small changes in the initial lay angle. In the end fitting where the wires are terminated, this change in lay angle may be restrained. In the case of restraint, this will give rise to local bending stresses, [Thorsen, 2011]. Longitudinal stresses due to bending will add to the total axial stress and this may possibly constitute a danger when it comes to fatigue of the pipe, specially if it is reasonable to believe that metal to metal contact occurs.

In the unloaded configuration the angle between the tensile armour wires and the longitudinal axis of the pipe (the lay angle) is α_0 , see Figure 8.11.

As the pipe is axially strained, the curve which the wires follow must change. If no end restraints are present, the change in lay angle would be the same at all points along the wire, and the wire would assume a path like the red one in the figure. The new lay angle is denoted α_1 . The displacement pattern (α_1) and wire strain (ϵ_{11}) is only possible when no end restraints are present. The wire is in fact fixed at the end fitting, meaning that the lay angle must remain at α_0 at the end fitting and gradually increase towards α_1 as one moves away from the end. This is illustrated in Figure 8.11 with a blue line. Therefore the *actual* change in lay angle is introduced as the variable $\eta(X^1)$, meaning that the new lay angle at any point along the wire is given as $\alpha_0 - \eta(X^1)$ which in the limit reaches the

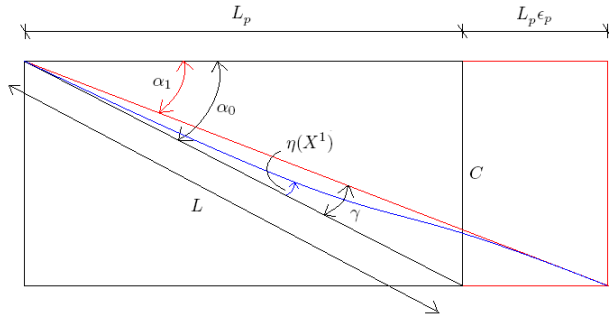


Figure 8.11: Definitions related to the wire behaviour at end fitting, [Thorsen, 2011]

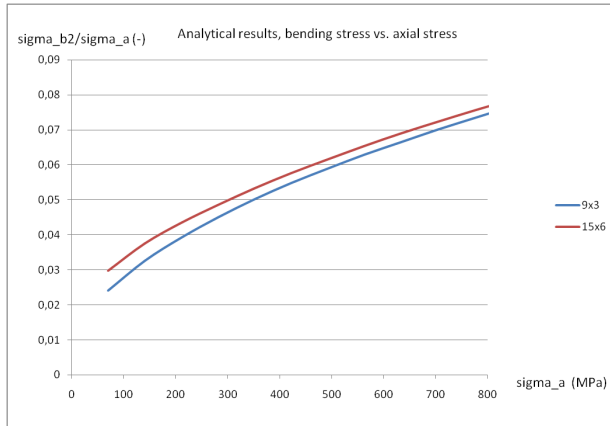


Figure 8.12: Analytical results for the ratio between bending and axial stress., [Thorsen, 2011]

change in lay angle γ . For the no friction case, the local bending stress about the wire strong axis can be approximated as [Thorsen, 2011]:

$$\sigma_{11}^{M3} \simeq 1.73E\gamma \cos \alpha \epsilon_p^{0.5} \quad (8.19)$$

where σ_{11}^{M3} is defined in Figure 8.5(a) and γ is the change in lay angle. Eq. 8.19 has been used to calculate numerical values for a wide range of pipe strain. The calculations have been performed assuming standard steel properties and the results are shown in Figure 8.12, where the ratio between local bending stress and axial stress are shown for two different wire dimensions. The blue line shows results for a wire of width 9 mm and thickness 3 mm, while the red line shows a larger wire of width 15 mm and thickness 6 mm. The radius of the pipe is 0.1 meters and the lay angle is 35° in both cases.

As seen in the figure, the bending component grows larger relative to the axial stress as the stress increases, and the bending stress exceeds 6 % of the axial stress for an axial stress above 500 MPa. The rate of increase in bending stress is relatively large at low strain levels, but it does however decay as the axial stress increase. Even so, the relative magnitude of bending stress continues to increase. It is also observed that the two curves

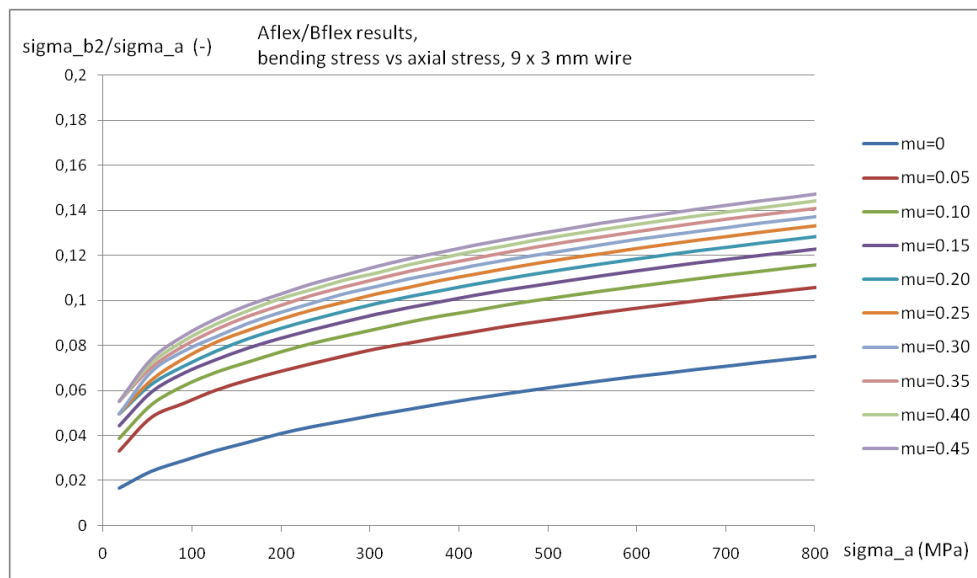


Figure 8.13: FE results for end fitting bending stress, 9 x 3 mm wire, [Thorsen, 2011]

in the figure are located very close to each other despite the relatively large differences in wire dimensions.

A major limitation of the analytical model is the assumption of zero friction. Friction will restrain the wire motion and force the wire into the new lay angle over shorter length. FE analyses have been carried out to investigate the effect of friction in a single wire [Thorsen, 2011] for wire dimensions 9 x 3 mm wire and 15 x 6 mm. The results are presented in Figure 8.13 and Figure 8.14.

As seen, the friction greatly increases the bending stress at the end fitting and for a two layered structure, one may experience a localized bending stress of approximately 16 % of the axial stress if the pure axial stress is 400 MPa. This is significant, and should be considered in fatigue evaluations of the armour wires if significant dynamic tension occurs. It is however noted that all the above calculations rests on the assumption that the armour wires are fully fixed at the end fitting. The accuracy of this assumption depends on the end fitting construction, and more detailed analyses taking the end fitting behaviour into the calculations should be performed in the general case.

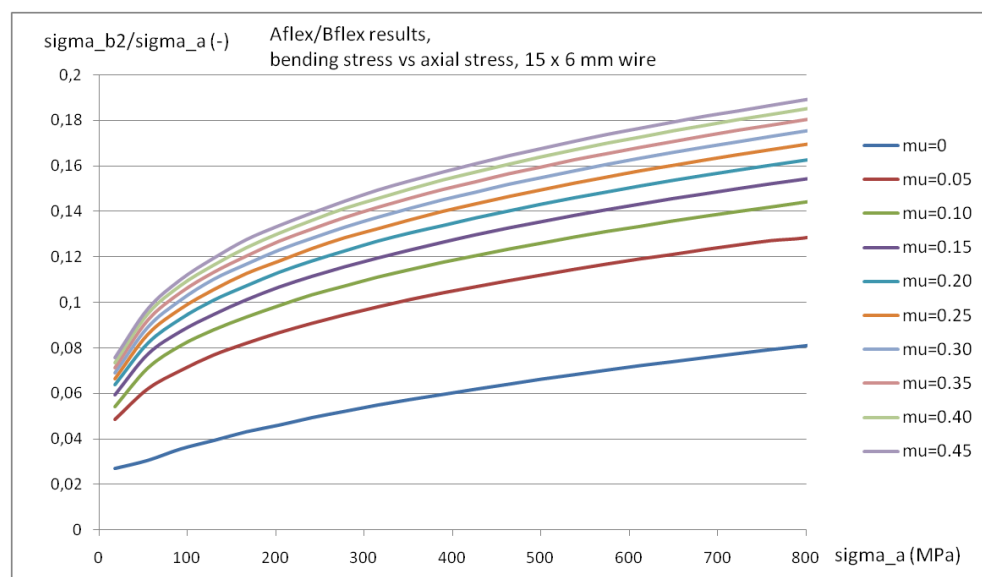


Figure 8.14: FE results for end fitting bending stress, 15 x 6 mm wire, [Thorsen, 2011]

8.4.3 Torsion

Excessive torsion may give lock-up of the wires causing "birdcaging" or structural damage to the pipe. This is not a very likely failure mode under normal operational conditions where the torsional loads are small. However, there have been cases of excessive torsion during pipe installation, which have caused failure in the pipe. An axial tensile force will prevent torsional damage. This positive effect is normally taken into account by verifying the torsional strength for a tensile force not greater than the minimum axial force predicted from the dynamic analysis of the riser system. The torsional resistance from all N_a resisting layers must equal to the torsional moment M_t given as:

$$\sum_{i=1}^{N_a} n_j \sigma_{11j} A_t R_j \sin \alpha_j = M_t \quad (8.20)$$

The major contribution to the torsional resistance comes from the helically wound tensile armours, which leads to the following formula for a quick evaluation of the stresses in the tensile layers:

$$\sigma_{11} = \frac{M_t}{RnA_t \sin \alpha} \quad (8.21)$$

where n is the total number of wires in the armouring layers, A_t is the cross section area of each wire and R is the mean radius of the armouring layers. Again, two tensile armour layers with equal but opposite lay angles have been assumed. By combining Eq. 8.21 and Eq. 8.13, disregarding the ϵ_p and u_3 components, the following expression may be used for an approximate evaluation of the torsional stiffness of the pipe

$$GI_t = nA_t E R^2 \sin^2 \alpha \cos \alpha = E 2\pi R^3 t_{tot} F_f \sin^2 \alpha \cos^2 \alpha \quad (8.22)$$

The above formulas assume that all layers remain in contact. It should be pointed out that there is an asymmetry in the torsional stiffness. When the pipe is twisted, gaps will tend to occur between the layers as one layer will tend to move outwards and the other inwards. The presence and location of these gaps therefore depends on the direction of the applied moment, the load condition and the pipe design (A 55° degree structure will behave different from a standard 35° structure). Considering a standard 35° structure and load cases dominated by tension and internal pressure, the tensile armour will be squeezed against the pressure armour and the torsion stiffness will be high. In cases where axial compression occurs, eg. during installation, the tensile armour will be supported by the soft outer sheath/anti-buckling tape and the torsion stiffness will be lower.

Experimental studies of the torsional behaviour of a 4" Technip pipe are reported [Skallerud, 1991a]. The pipes exhibit torsional behaviour which is similar to the axial behaviour shown in Figure 8.9, although the hysteresis is less dependent on the load frequency, the latter most likely being caused by friction induced in the pressure armour and due to the relative rotation between layers. Since friction effects are sensitive to the gap conditions, the torsion damping will vary with the load condition. However, the results showed that a linear stiffness relation can be assumed between torque and torsion as for the axial load case.

8.4.4 Internal and external pressure

Bursting of a pipe by excessive internal pressure can occur if the pipe is not properly designed, or if the maximum internal pressure is considerably underestimated. However, if the internal pressure is known this failure mode is not likely to occur, see Section A3. The design pressure includes operating pressure and allowances for surges or other factors affecting the internal pressure. This should be combined with atmospheric external pressure. For selection of design parameters, see [API, 2008b].

When a pipe is subjected to internal pressure the load will be carried by the tensile and pressure armour layers. The equilibrium between stresses and radial forces may be expressed by the following equation:

$$\sum_{j=1}^{N_a} \frac{n_j \sigma_{11j} A_j \sin^2 \alpha_j}{R_j} \frac{1}{\cos \alpha_j} = 2\pi(p_{int} R_{int} - p_{ext} R_{ext}) \quad (8.23)$$

where N_a is the number of pressure resisting layers. The first term on the left hand side is related to the axial force in the wires which when multiplied by the normal curvature gives the radial line load, as in Eq. 8.9, whereas the $\frac{1}{\cos \alpha_j}$ term describes the length difference between an unit segment length along the pipe and the helix. A good approximation is to assume that the plastic sheaths transmit pressure, i.e. there is no pressure differential through the plastic layers. The interlocked carcass does not carry any part of the internal pressure. Consequently, the pressure resisting layers are the pressure spiral wire layers and the cross-wound armour layers, with the pressure spiral wire layers taking the major role.

Eq. 8.23 and Eq. 8.1 may be combined to arrive at the following expression for the tensile armour contribution to burst pressure resistance:

$$p_h = \frac{t_{tot}}{R} F_f \sigma_u \sin^2 \alpha \quad (8.24)$$

where t_{tot} is the total thickness of the double tensile armour layers, R is the mean radius of the helical armour layers and σ_u is the ultimate tensile strength of the layer. Eq. 8.11 may be used to derive the following expression for the tensile armour contribution to end cap pressure resistance:

$$p_a = 2 \frac{R}{R_{int}^2} t_{tot} F_f \sigma_u \cos^2 \alpha \quad (8.25)$$

In the case of no zeta or back-up pressure layer, the stress in the helical armours alone must balance the hoop and end cap effects of the internal pressure, i.e. $p_h = p_a$. Assuming $R_{int} \sim R$, this gives $\tan^2 \alpha = 2$, or $\alpha = 54.7^\circ$. This is the "neutral" or "balanced" lay angle at which there is no tendency for the helical armour to change shape under load. Since a pipe is usually reinforced by several layers, the balanced angle will depend on the relative amount of steel in the helical armour layers and the pressure layers. The optimum lay angle is then typically $35 - 40^\circ$, cf. [Nielsen et al., 1990b]. The contribution to burst pressure

resistance from the pressure layers, p_p may be obtained from the following expression:

$$p_p = \sum_{j=1}^{N_p} \frac{t_j}{R} F_{fj} \sigma_{uj} \quad (8.26)$$

where t_j denote the thickness of pressure spiral wire layer number j and R is the mean radius of the N_p pressure layers, respectively. The fill factor F_{fj} applies for pressure spiral wire layer j . The total hoop pressure resistance is then obtained by summing the contribution from each layer as:

$$p_{hoop} = p_p + p_h \quad (8.27)$$

The burst pressure is then given by the smallest of p_{hoop} and p_a i.e. hoop and axial resistance:

$$p_b = \min(p_{hoop}, p_a) \quad (8.28)$$

In pipe design, the lay angle is usually chosen to give equal burst resistance in the axial and hoop directions. The procedure for burst pressure calculations, described above, is quite simple and straightforward. Experimental results, reported by [Chen et al., 1992], show that the above procedure gives quite reliable estimates of burst pressure. The average deviation from test results was reported to be within 3%, and with a maximum deviation of 7-8%.

8.5 Behaviour in bending

8.5.1 General

The bending behaviour of flexible pipes is a more complex phenomenon to analyse than the axisymmetric load case. The flexural response shows a pronounced hysteresis behaviour. This is illustrated by the moment/curvature relation in Figure 8.15. The hysteresis behaviour of nonbonded pipes may be explained by the internal slip mechanism. Such pipes have a number of helical reinforcing layers, which tend to slip relative to each other when the pipe is bent. This is particularly the case for the two crosswound tensile layers. When the curvatures are small, slip is prevented by the internal friction between the layers, giving a high initial tangent stiffness, EI_s , corresponding to the sum of contributions from all layers when assuming plane surfaces remain plane as for standard beam theory. The moment needed to overcome the friction forces, M_f , is called the friction moment. M_f depends on the contact pressure between pipe layers, and consequently on the loads applied to the pipe. When the friction moment is exceeded, the curvature varies linearly with the moment variation. The slope of this line corresponds to the elastic bending stiffness EI_e represented by the sum of contributions from elastic bending of the plastic layers and each individual wire. This stiffness is rather low and the main part of it is due to the stiffness of the plastic sheaths. It should also be noted that when the direction of the curvature is changed, the change in moment has to exceed twice the friction moment before reversed slip behaviour occurs.

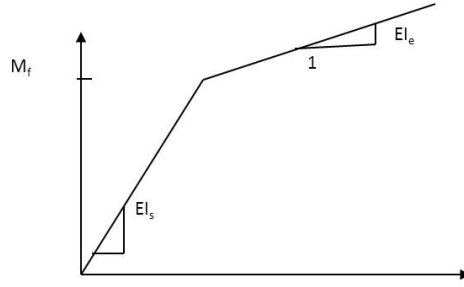


Figure 8.15: Typical moment curvature relation for non-bonded flexible pipe

8.5.2 Minimum bend radius

Excessive bending can lead to local buckling destruction of the pipe as the interlocking elements or helical armour elements interfere and touch each other as well as plastic layer overstraining. [API, 2008b] defines the minimum bend radius from the concepts of minimum storage radius, ρ_s , and the minimum locking radius, ρ_l , needed to cause unlocking of the interlocked layers where a primary requirement is that ρ_s is always greater than ρ_l . Different safety factors are then applied based on the load type and condition to prevent damage when the pipe is bent in dynamic, static, installation and storage configurations.

The locking radius at which contact occurs between elements within the different helical layers, may be computed when the layer geometry is known. Figure 8.16 shows the relevant geometric quantities for both the tensile armour and the interlocked profiles used in the pressure armour. The locking radius is found considering the bending strain needed to close the gap at the tensile or compressive sides of the pipe. For the interlocked profiles, this can be formulated at the compressive side where shortening occurs as:

$$\frac{L_p}{n} \frac{R}{\rho_l} = \frac{L_p}{n} - \frac{b_{min}}{\sin \alpha} \quad (8.29)$$

and at the tensile side where elongation occurs;

$$\frac{L_p}{n} \frac{R}{\rho_l} = \frac{b_{max}}{\sin \alpha} - \frac{L_p}{n} \quad (8.30)$$

For the tensile armour, the compressive side applies resulting in:

$$\rho_l = \frac{R}{1 - F_f} \quad (8.31)$$

The locking radius for the pipe is taken to be the largest ρ_l for all helical layers. In order to maintain integrity of the plastic layers, this is governed by the maximum allowable strain, see [API, 2008b]. This gives the following limit for the bending radius of the plastic layer:

$$\rho_\epsilon = \frac{R}{\epsilon_{lim}} \quad (8.32)$$

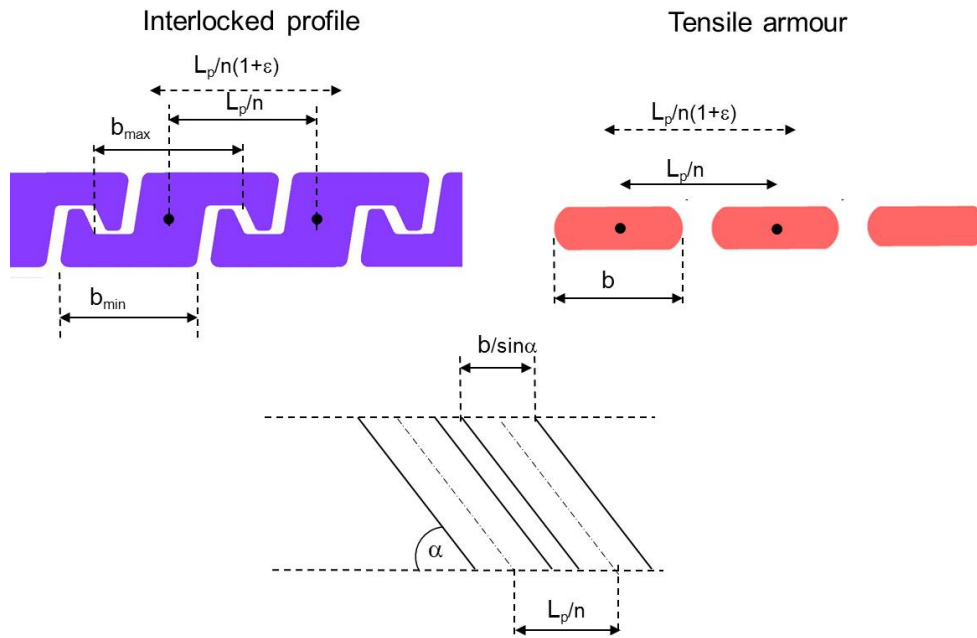


Figure 8.16: Geometrical properties of armour layers relevant for minimum radius prediction

The minimum bend radius is established from considering both ρ_e and ρ_l and including relevant safety factors as specified in [API, 2008b].

8.5.3 Stresses and stress resultants related to the tensile armour

As stated above, the static reference stress level in the tensile armour is given by the mean static effective tension and associated internal and external pressures. This gives a mean axial stress and associated contact pressures that governs the friction moment. In a flexible riser the tension and external pressure will vary along its length, hence the friction moment will also change along the riser. Further, due to the differences in contact pressure between layers, the response in terms of dynamic stresses due to bending induced by floater motion and hydrodynamic loads will be different between layers. Hence, the nature of dynamic stresses will be characterized by both variation between layers and along the length of a flexible riser.

For the tensile armour layers, the dynamic stresses will consist of an axial friction stress associated to the slip between layers, axial stresses from dynamic tension and local torsion and bending stresses resulting from the components of global curvature along each wire.

Local wire bending stresses in tensile armour

In the stressed state, the local bending behaviour can be described by assuming that each wire follows an assumed path along the curved pipe surface and application of differential

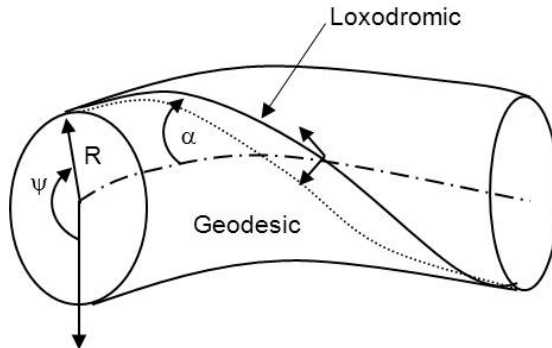


Figure 8.17: Definition of curve paths

geometry. With regard to which path each wire will follow, there are two assumptions that have been commonly used, see [Feret et al., 1986] and [Sævik, 1993] and Figure 8.17:

- The *Geodesic*
- The *Loxodromic*

The loxodromic curve represents the curve that would represent the initial path of each wire on the circular cylinder as if the path was fixed relative to the surface. The geodesic represents the shortest distance between two points, respectively on the tensile and compressive sides of the pipe along the same helix. It has no transverse curvature and both longitudinal and transverse slip relative to the loxodromic is needed to reach the geodesic path as illustrated in Figure 8.17.

As a result of bending, shear forces will build up between each wire and the pipe until slip starts. Due to the relative large axial stiffness of each wire, longitudinal slip is enforced to eliminate the length difference between the compressive and tensile sides of the pipe. However, based on the work by Sævik [Sævik, 1993], the transverse wire displacements towards the geodesic will be restrained by transverse friction forces. Hence, the dynamic bending torsion and curvature in each wire, ω_{ip} , will be somewhere between the solution given by the above limit curves. If no slip is assumed, the loxodromic curve applies and the torsion and curvature quantities can be determined with reference to Figure 8.18 as:

$$\omega_{1p} = \sin \alpha \cos^3 \alpha \cos \psi \beta_2 \quad (8.33)$$

$$\omega_{2p} = -\cos^4 \alpha \cos \psi \beta_2 \quad (8.34)$$

$$\omega_{3p} = (1 + \sin^2 \alpha) \cos \alpha \sin \psi \beta_2 \quad (8.35)$$

where β_2 is the global curvature at the cross-section centre and ψ is the angular coordinate starting from the lower side of the pipe, see Figure 8.18.

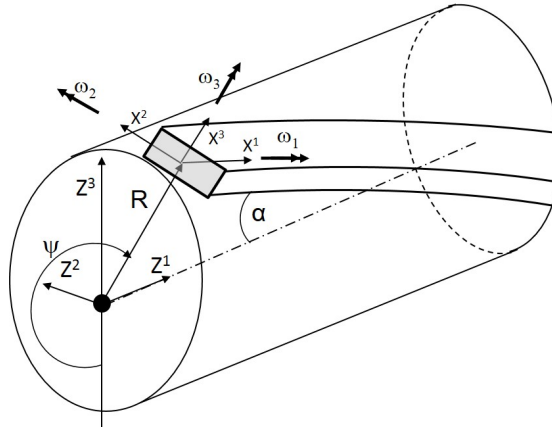


Figure 8.18: Definition of curvature quantities

However, since longitudinal slip is unavoidable, this will change the curvature quantities even if no transverse slip occurs. If no axial friction is assumed, the longitudinal relative displacement is given by:

$$u_1 = R^2 \frac{\cos^2 \alpha}{\sin \alpha} \sin \psi \beta_2 \quad (8.36)$$

which then changes the above torsion and the weak axis curvature into:

$$\omega_{1p} = 2 \sin \alpha \cos^3 \alpha \cos \psi \beta_2 \quad (8.37)$$

$$\omega_{2p} = -\cos^2 \alpha \cos 2\alpha \cos \psi \beta_2 \quad (8.38)$$

where it is noted that the transverse curvature ω_{3p} (bending about strong axis of the flat wire) is unaffected.

The corresponding quantities along the geodesic curve which assumes both longitudinal and transverse slips are , [Sævik, 1992]:

$$\omega_{1p} = -\sin \alpha \cos \alpha \left[\frac{1}{\sin^2 \alpha - 3} \right] \cos \psi \beta_2 \quad (8.39)$$

$$\omega_{2p} = -3 \cos^2 \alpha \cos \psi \beta_2 \quad (8.40)$$

$$\omega_{3p} = 0 \quad (8.41)$$

The slip towards the geodesic also involves a transverse slip component in addition to the longitudinal component in Eq. 8.36:

$$u_2 = \frac{R^2}{\tan \alpha} \left[\frac{\cos^2 \alpha}{\sin \alpha} + 2 \sin \alpha \right] \sin \psi \beta_2 \quad (8.42)$$

Moment-curvature behaviour and associated friction stresses

As noted above, the pipe initially behaves as a rigid pipe according to Navier's hypothesis during increased bending. At a certain point, however, the shear stress at the neutral axis of bending will exceed the shear capacity governed by friction and slip will occur between layers. With reference to Figure 8.18, considering plane deformation only i.e. $\beta_2 \neq 0$, the axial force Q_1 in the wire of cross-section area A_t before slip is given by:

$$Q_1 = -EA_t \cos^2 \alpha R \cos \psi \beta_2 \quad (8.43)$$

The associated shear force q_1 per unit length along the wire needed to fulfil the plane surfaces remain plane condition is obtained by differentiating the above equation with respect to the length coordinate X^1 and applying the relation $\psi = \frac{\sin \alpha}{R} X^1$:

$$q_1 = EA_t \cos^2 \alpha \sin \alpha \sin \psi \beta_2 \quad (8.44)$$

where the maximum is found at the pipe neutral axis of bending as for standard beam theory. The shear stress increases until the maximum possible shear stress q_{1c} is obtained:

$$q_{1c} = \mu(q_3^I + q_3^{I+1}) \quad (8.45)$$

where μ is the friction coefficient and the index I refers to the inner and outer surfaces of the wire. The critical curvature β_{2c} is then found by equating q_1 and q_{1c} as:

$$\beta_{2c} = \frac{\mu(q_3^I + q_3^{I+1})}{EA_t \cos^2 \alpha \sin \alpha} \quad (8.46)$$

and the stress at the outer fibre of the pipe at this stage is:

$$\frac{\mu(q_3^I + q_3^{I+1})R}{\sin \alpha A_t} \quad (8.47)$$

which is noted to be a factor $\pi/2$ less than the value found by equilibrium assuming full slip along the quarter pitch helical path.

Assuming harmonic helix motion and no end effects, an arbitrary cross-section can be divided into two zones as illustrated in Figure 8.19 where one part of the cross-section will be in the slip domain (Region II), whereas the other will still be in the stick-domain (Region I). Considering one quarter of the cross-section and at the tensile side (the upper right part of Figure 8.19), the transition between these two regions can be defined by the angle ψ_0 :

$$\frac{\psi_0}{\sin \psi_0} = \frac{\beta_2}{\beta_{2c}} \quad (8.48)$$

where β_2 represents the actual curvature of the cross-section at any stage beyond slip. At this stage, the stress distribution along Region II in the considered cross-section quarter can be expressed by:

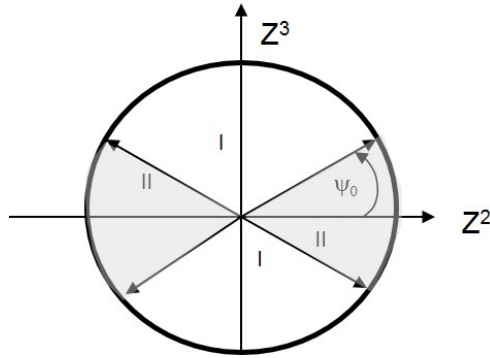


Figure 8.19: Cross-section slip zone

$$\sigma_{11}(\psi) = \frac{\mu(q_3^I + q_3^{I+1})R}{\sin \alpha A_t} \psi \quad (8.49)$$

whereas the stress in Region I can be expressed by:

$$\sigma_{11}(\psi) = E \cos^2 \alpha R \beta_2 (\sin \psi - \sin \psi_0) + \frac{\mu(q_3^I + q_3^{I+1})R}{\sin \alpha A_t} \psi_0 \quad (8.50)$$

where it is noted that at full slip $\psi = \psi_0 = \frac{\pi}{2}$, the cross-section stress reaches its full value given by:

$$\sigma_{11} = \frac{\pi}{2} \frac{\mu(q_3^I + q_3^{I+1})R}{\sin \alpha A_t} \quad (8.51)$$

The associated bending moment can be found by integration, utilizing symmetry and considering the layer as a thin shell layer with thickness t as:

$$\begin{aligned} M = 4F_f \cos^2 \alpha & \left[\int_0^{\psi_0} \frac{\mu(q_3^i + q_3^{i+1})}{\sin \alpha A_t} \psi \right. \\ & \left. + \int_{\psi_0}^{\frac{\pi}{2}} E \cos^2 \alpha \beta_2 (\sin \psi - \sin \psi_0) + \frac{\mu(q_3^I + q_3^{I+1})}{\sin \alpha A_t} \psi_0 \right] R^3 \sin \psi t d\psi \end{aligned} \quad (8.52)$$

From the above, the start slip bending moment contribution from each layer is found to be:

$$M_c = \frac{R^2 \mu(q_3^I + q_3^{I+1}) n}{2 \tan \alpha} = F_f \frac{\pi R^3 \cos^2 \alpha \mu(q_3^I + q_3^{I+1})}{b \sin \alpha} \quad (8.53)$$

whereas the full slip bending moment from the same layer is determined to be:

$$M_f = \frac{2R^2 \mu(q_3^I + q_3^{I+1}) n}{\pi \tan \alpha} = F_f \frac{4R^3 \cos^2 \alpha \mu(q_3^I + q_3^{I+1})}{b \sin \alpha} \quad (8.54)$$

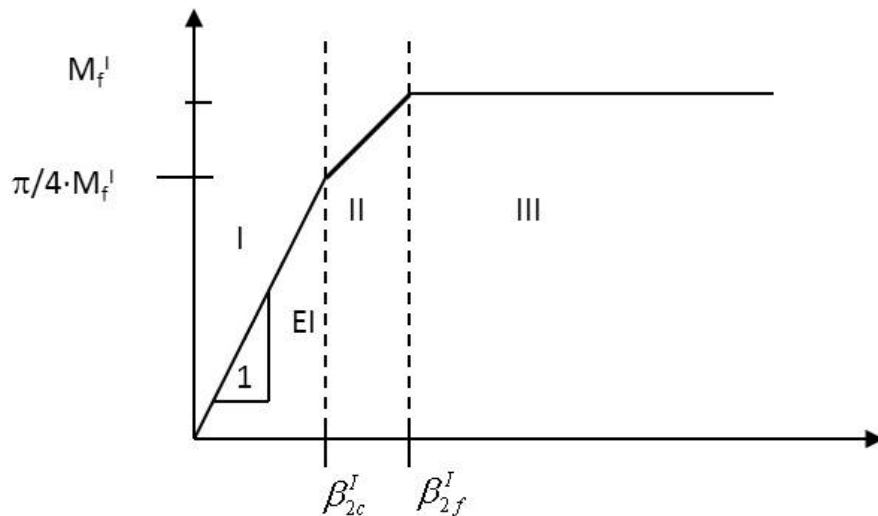


Figure 8.20: Moment curvature contribution from each layer

It is noted that the difference between these two moment values is a factor $\frac{\pi}{4}$ which is in agreement with the value obtained when comparing the initial and full yield bending moments for a steel pipe having a perfect elastic-plastic material characteristic.

By application of Eq. 8.48 and Eq. 8.52 a moment curvature diagram can be constructed for each layer as illustrated in Figure 8.20. This diagram represents the friction contribution to the moment curvature relation from each tensile armour layer and can be represented as a three-linear function. The contact pressure will vary between layers and the total moment curvature diagram will therefore include a sum of three-linear relations, one for each layer. However, since the transition to start slip to end slip is small in terms of curvature increase, the diagram can be approximated as sum of bi-linear relations and the contribution from one tensile armour layer to the bending stiffness before slip can be found by dividing the slip bending moment of Eq. 8.53 with the slip curvature in Eq. 8.46. The bending stiffness contribution from friction in each layer can then be written as:

$$\begin{aligned}\beta_2 &\leq \frac{4}{\pi} \beta_{2c} : EI_s = F_f \cos^4 \alpha \pi R^3 t \\ \beta_2 &> \frac{4}{\pi} \beta_{2c} : EI_s = 0\end{aligned}\quad (8.55)$$

This gives the following total bending stiffness relation for the flexible pipe:

$$EI = EI_e + \sum_{i=1}^{N_t} F_{fi} \cos^4 \alpha_i \pi R_i^3 t_i f(\beta_2, \beta_{2ci}) \quad (8.56)$$

where f is a function that is 1 for $\beta_2 \leq \beta_{2ci}$ and 0 for $\beta_2 > \beta_{2ci}$ for each layer i . It is noted that for dynamic loading the slip curvature range will be twice the amplitude

limits described above. EI_e represents the sum of elastic contributions from the plastic layers and local wire bending. The local wire bending contribution is also influenced by the wire tension which increases the geometric stiffness against bending. By assuming the loxodromic curve representation for the tensile armour, the following expression may be applied to estimate EI_e :

$$\begin{aligned} EI_e = & \sum_{j=1}^{N_{pl}} \frac{\pi}{4} E_j [(R_j^o)^4 - (R_j^i)^4] \\ & + \frac{1}{2} \sum_{j=1}^{N_t} n_j [G_j I_{1j} 4 \sin^2 \alpha_j \cos^5 \alpha_j + E_j I_{2j} \cos^3 \alpha_j \cos^2 2\alpha_j + E_j I_{3j} \cos \alpha_j (1 + 2 \sin^2 \alpha_j + \sin^4 \alpha_j)] \\ & + \sum_{j=1}^{N_t} F_{fj} \sigma_{11j} \pi R_j^3 t_j [9 \cos^4 \alpha_j \sin^2 \alpha_j + 6 \cos^6 \alpha_j + \frac{\cos^8 \alpha_j}{\sin^2 \alpha_j} + \frac{\cos^4 \alpha_j}{\sin^2 \alpha_j} + 4] \end{aligned} \quad (8.57)$$

Since, the behaviour of the plastic layers is sensitive to temperature and the geometric stiffness and slip limit depend on pressure and tension, several moment-curvature relations may have to be used in strength calculations, depending on the condition to be evaluated.

It is also to be noted that the above model is based on the assumption that no significant end effects are present, i.e. the curvature takes place away from the end fitting where each wire is anchored. In cases where this is not the case, more advanced formulations based on individual wire modelling using general or specialized FE softwares, may be needed.

For most cases, however, the moment-curvature based model presented above have proven to give good stress and fatigue estimates for the tensile armour as compared to test data, see [Sævik, 2011].

Influence of shear deformations in the tape layers

If the tensile armour is supported by thick plastic layers, shear deformations might occur. If that is the case, plane surfaces no longer remain plane before the slip begins. The shear stress between the wire and the antiwear layer will then be governed by the inherent shear deformations and the tape material shear modulus. This is illustrated in Figure 8.21

By equilibrium, the following differential equation can be formulated along the wire:

$$\frac{EA_t \sin \alpha}{R} u_{1,11} - ku = -ku_{1p} \quad (8.58)$$

where u_{1p} is the displacement corresponding to plane surfaces remain plane from Eq. 8.36 and k is the shear stiffness parameter defined by:

$$k = G \frac{b}{t} = \frac{E_p b}{2(1+\nu)t} \quad (8.59)$$

where E_p is the Young's modulus of the plastic layer. By only considering the particular solution, the following solution is obtained for the slip curvature:

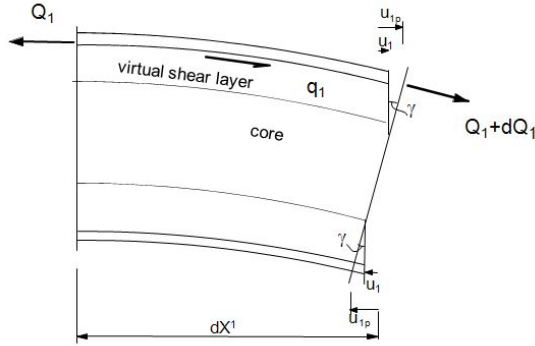


Figure 8.21: Shear deformation model

$$\beta_{2c} = \left[1 + \frac{\sin^2 \alpha E A_t}{k R^2}\right] \frac{\mu(q_3^I + q_3^{I+1})}{E A \cos^2 \alpha \sin \alpha} \quad (8.60)$$

It is seen that the k parameter will cause the slip curvature to increase, hence reducing the stress in the stick domain at a given curvature.

In [Skallerud, 1991a] and [Skallerud, 1991b] the results from testing two 4 inch pipes in bending at variable pressures were presented. The inner tensile armour in the two pipes were respectively supported by 1.5 mm and 2 mm antiwear layers and in the latter case the two armour layers were separated by another 2 mm antiwear layer. The results from these tests are presented together with the results obtained by the BFLEX software, [Sævik, 2010] in Figure 8.22. The model includes using both the plane surfaces remain plane assumption in Eq. 8.46 and the shear slip model in Eq. 8.60 given above. The initial straight line illustrates the pre-slip bending stiffness calculated analytically from Eq. 8.56. It is seen that the shear model seems to describe the slip transition better than the plane surfaces remain plane model. However, the plane surfaces remain plane model will be conservative in a fatigue calculation and since the resulting stress is sensitive to the k parameter selected, a large number of model tests are needed in order to provide sufficient confidence level in the shear interaction model.

8.5.4 Stresses related to the pressure armour

With respect to bending stresses in the pressure armour, there are two significant contributions to consider with reference to Figure 8.2:

1. Bending induced longitudinal σ_{11} stresses in the hoop direction.
2. Stresses introduced in the cross-section plane, primarily σ_{22} , σ_{23} and σ_{33} stresses.

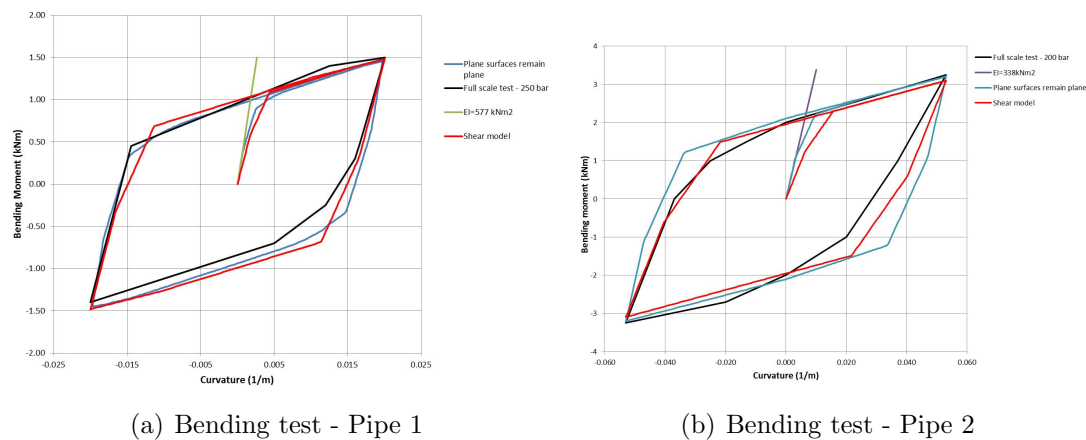


Figure 8.22: Correlation between model and bending tests, [Skallerud, 1991a] and [Skallerud, 1991b]

Longitudinal stresses

Due to the large lay angle and interlocked nature of the pressure armour, the relative displacements and associated longitudinal friction stresses introduced by bending will be insignificant and can be neglected. Further by studying Eq. 8.33-Eq. 8.35, the only first order term in $\cos \alpha$ is found for the transverse curvature in Eq. 8.35. Hence, in terms of bending fatigue calculations it is common practice to only include this term with respect to local elastic bending of each wire.

The Carcass and the pressure spiral wires act to keep the cross-section circular. During bending, however, ovalization and membrane stresses will be introduced due to the following effects with reference to Figure 8.23:

1. The reaction forces due to the support from bending restrictors, bend stiffeners or other external structures termed the *Tension and shear force differential effect*.
2. The bending moment itself termed the *Bending moment effect*.
3. The shear stresses resulting from the variation of contact pressure in the tensile armour, termed the *Shear stress membrane effect*.

With respect to the *Tension and shear force differential effect*, the reaction line load q resulting from plane pipe bending about the Z^2 axis in Figure 8.4 can be described by standard beam theory as:

$$q = EI \frac{\delta Q}{\delta Z_1} + T\beta_2 \quad (8.61)$$

where Q is the shear force, T is the effective tension and β_2 is the global curvature. The line load q results in an intensity w and the resulting ovalization bending stresses can be estimated by using the circular ring formula of Table 9.2 in [Young and Budynas, 2002].

The *Bending moment effect* comes primarily from the plastic layers and the tensile armour due to friction and elastic bending. The bending stresses in these layers in combination with global curvature gives an harmonic squeeze load intensity w given by:

$$w = \frac{M}{\pi R^2} \cos \psi \beta_2 \quad (8.62)$$

where M is the total bending moment. This effect will act to increase the ovalization.

The *Shear stress membrane effect* does not cause additional ovalization bending stresses. However, realising that the friction stress introduced by bending in the tensile armour will cause an increased tensile stress and contact pressure at the tensile side and a subsequent reduction at the compressive side, this must be balanced by simultaneous variation in the pressure armour hoop stresses to fulfil equilibrium at any section in the hoop direction. This requires that the variation in contact pressure is balanced by shear stress and normal stresses at the tensile/pressure armour interface. This will not result in additional ovalization bending moments, however, at the tensile side there will be a reduction in the hoop stress (reduction in the axial force and the longitudinal stress) and at the compressive side there will be an increased hoop stress in the pressure spiral wire. An illustration of the longitudinal stress variation resulting from the above effects is seen in Figure 8.24

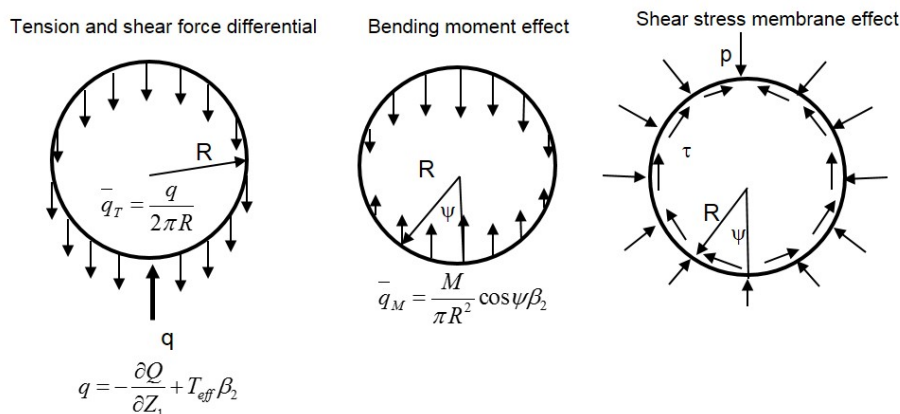


Figure 8.23: Physical effects related to ovalisation

Stresses in the cross-section plane

As noted in Section 8.2 the interlocked nature of the pressure spiral wire causes stresses in the cross-section plane will occur due to the axi-symmetric loads, primarily σ_{22} , σ_{23} and σ_{33} stresses with reference to Figure 8.2. During bending, the pressure spiral wires are forced into the overall pipe curvature. This causes two effects relevant with respect to dynamic variation and fatigue:

1. At the tensile and compressive sides each winding will be forced to move relative to each other
2. At the same sides the nubs and valleys will be opened or closed in order to accomodate the overall pipe curvature

The first of the above effects will cause friction to be mobilised at the metal interfaces giving rise to variations in the σ_{22} and σ_{23} components. The second effect will primarily cause variations in the σ_{33} and σ_{23} components. As illustrated in Figure 8.25 for the Z-spiral this can be looked upon as a thick cantilever beam exposed to a pair of varying point loads. Since the length/height ratio of the beam is small, shear stresses are important and so also are the local geometries in terms of the profile curve radii with respect to stress concentrations. These stresses are therefore more difficult to describe by analytical methods.

8.6 Buckling

8.6.1 Collapse

Excessive external pressure may lead to collapse of the pipe. Collapse usually involves flattening of the pipe which impedes the flow through it. However, this is not considered to be a critical failure mode since the design depth is usually well defined. This is also

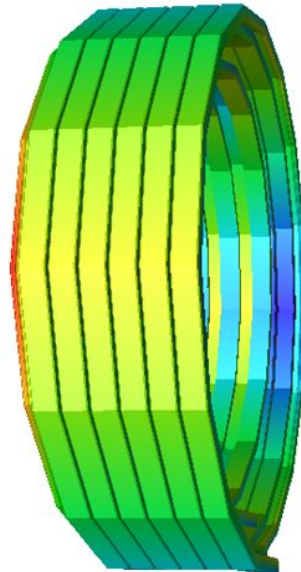


Figure 8.24: Longitudinal stress variation in pressure spiral wire

reflected in design recommendations for flexible pipes, where the safety factor is normally smaller than for bursting strength, see [API, 2008b]. The ultimate depth rating is to be verified for atmospheric internal pressure. When a pipe is subjected to external pressure, the loads are carried by the helical pressure layers and the interlocked carcass, all having a lay angle close to 90° . However, the collapse pressure given by the producers is often taken as the collapse strength of the interlocked carcass, disregarding the contribution from the other pressure spiral wire with regard to pressure load sharing. This is based on the pessimistic view that the outer sheaths may have been damaged in such a way that the external pressure acts directly on the inner plastic sheath. Therefore the interlocked carcass is normally designed to carry the full external pressure alone, however, the contribution in terms of bending stiffness support in the hoop direction from the other pressure layers is normally included.

The external pressure needed to initiate carcass collapse can be calculated based on the method by Timoshenko [Timoshenko and Gere, 1963]. The Timoshenko approach is based on considering the bending moment in a steel ring having an initial imperfection characteristic described by the function $R\delta_0 \cos 2\psi$, see Figure 8.27, where δ_0 represents the initial ovality either caused by manufacturing tolerances or bending loads. This definition of δ_0 is consistent with the API definition $(D_{max} - D_{min})/(D_{max} + D_{min})$. According to API [API, 2008a], if specific information about the actual carcass is not available, the initial ovality to be used for collapse calculations should not be less than 0.002.

If no gaps are present between the pressure armour layer, the elastic buckling pressure of the carcass may be determined as the sum of contributions from the carcass and the

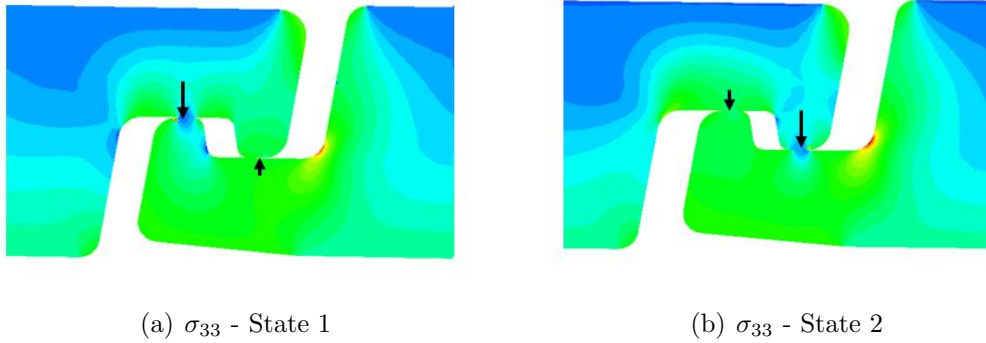


Figure 8.25: Variation in σ_{33} during a bending load cycle

pressure armour layers as:

$$p_{cr} = \sum_{i=1}^{N_p} \frac{3EI_{eq}^i}{R^3} \quad (8.63)$$

where R is the radius of the carcass and EI_{eq}^i is the equivalent ring bending stiffness of each layer per unit length of pipe. For a cylinder:

$$EI_{eq} = \frac{Et^3}{12(1-\nu^2)} \quad (8.64)$$

where ν is the Poisson's ratio. For the carcass and the pressure layers:

$$EI_{eq} = Kn \frac{EI_{2'}}{L_p} \quad (8.65)$$

where n is the number of tendons in the layer, L_p is the pitch and $I_{2'}$ is the smallest inertia moment. For the non-symmetric carcass and Z-shaped profiles the weakest axis will be the X^2' in Figure 8.7 and being obtained as:

$$I_{2'} = \frac{I_3 + I_2}{2} - \frac{1}{2} \sqrt{(I_3 - I_2)^2 + 4I_{32}^2} \quad (8.66)$$

K is a factor that depends on the lay angle and the moment of inertia in the section. For massive cross-sections $K \approx 1$.

The equivalent stiffness may also be determined from a static ring test carried out on a piece of the carcass. Such a test consists of measuring the deformation δ of an interlocked carcass subjected to a radial force F as shown in Figure 8.26. The equivalent ring bending stiffness may then be determined from the following relation:

$$\frac{EI_{eq}}{R^3} = \left(\frac{\pi}{4} - \frac{2}{\pi}\right) \frac{F}{\delta} \quad (8.67)$$

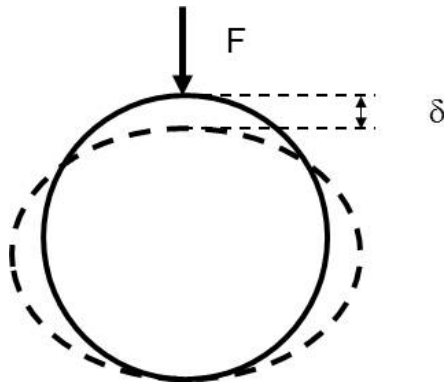


Figure 8.26: Ring stiffness test

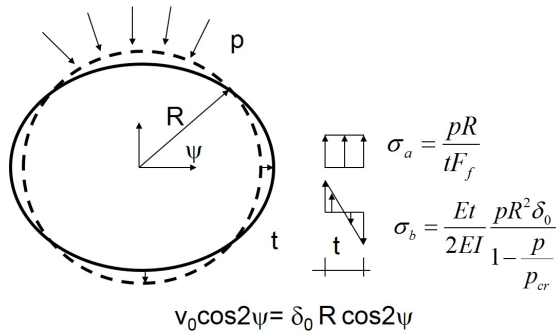


Figure 8.27: Timoschenko collapse model

The maximum bending moment introduced by the combined action of external pressure and the eccentricity parameter u_0 can then be found from:

$$M_{\max} = pR \frac{u_0}{1 - \frac{p}{p_{cr}}} \quad (8.68)$$

which has a direct analogy to Euler buckling analysis of imperfect beams. Collapse is assumed to occur when the outer fibre stress from bending and hoop stress in the carcass reaches the yield stress of the carcass material. Generally, if a residual stress σ_r occurs in the outer fibre, the yield stress σ_f will be reduced to an effective available yield stress σ_{fe} as:

$$\sigma_{fe} = \sigma_f - \sigma_r \quad (8.69)$$

The residual stress can be calculated based on assuming that the cross section is fully plastified at constant ultimate stress σ_u during manufacturing and that elastic unloading occurs to zero moment. In that case, the residual stress can be calculated as:

$$\sigma_r = \sigma_u \frac{W_p}{W_e} - \sigma_u \quad (8.70)$$

where W_p is the plastic area moment and W_e is the elastic area moment.

Collapse will then occur when:

$$\sigma_{fe} = \frac{tEpRu_0}{2EI_{eq}(1 - \frac{p}{p_{cr}})} + \frac{pR}{tF_f} \quad (8.71)$$

where t is the overall radial thickness of the carcass and the carcass fill factor F_f is determined from Eq. 8.2. The above leads to the following second order equation to determine the collapse pressure p :

$$p^2 - \left(\frac{F_f t \sigma_{fe}}{R} + p_{cr} \left(1 + \frac{Et^2 F_f R \delta_0}{2EI_{eq}} \right) \right) p + \frac{p_{cr} \sigma_{fe} t F_f}{R} = 0 \quad (8.72)$$

where it is noted that if it can be assumed that there is full contact between the carcass and the other pressure spiral wires, EI_{eq} will be the sum of contributions from the carcass and the other pressure spiral wires. According to Chen et.al. [Chen et al., 1992] if the gap between the carcass and the other spiral wires in a 6" flexible pipe is greater than 2.5 mm, the support effect from the other spiral wires can be neglected and the EI_{eq} will be determined by the carcass contribution alone. This may result in a significantly reduced external pressure collapse capacity.

If the pipe is exposed to bending and external reaction forces, this will increase the ovality δ_0 and thus reduce the capacity.

8.6.2 Tensile armour buckling

General

During installation and shut-down conditions where the pipe bore is exposed to external overpressure, the tensile armour will be in compression, even if the effective tension is positive. This may lead to local radial and transverse buckling of the tensile wires, leading to overall torsion instabilities. This failure mode was reported by Bectarte and Coutarel [Bectarte and Coutarel, 2004] including both bird caging (radial failure) and lateral buckling. Test procedures for lateral buckling were described that included the effect of cyclic bending. A computer model was also mentioned, but no details with respect to methods or results were given. The methods used to validate the pipe capacity with respect to this failure mode included laboratory testing, Deep water Immersion Performance (DIP) testing and mathematical models.

With respect to mathematical models Tan et al. described the behaviour of tensile armour wires under compression [Tan et al., 2006]. A strain energy approach for modelling the buckling and post-buckling behaviour of the wires is outlined, but no expressions or results were presented. However, some test results were presented stating that lateral buckling of the wires was observed under cyclic bending and wet annulus conditions. Vaz and Rizzo [Vaz and Rizzo, 2011] presented a finite element (FE) model, studying the influence of friction, interlayer contact conditions and anti-buckling tape capacity on the collapse load behaviour under pure external pressure loading but no bending, identifying

four different modes of failure, depending on the amount of friction and the properties of the anti-buckling tape. Based on FE analysis Brack et.al. [Brack et al., 2005] pointed out the importance of radial gaps, interlayer friction and the torsional resistance from the anti-buckling tape with respect to the axis of individual wire buckling. Østergard et. al [Østergaard et al., 2011] presented a model that was capable of describing the coupling between the individual wire buckling and overall global behaviour for combined external pressure and bending loads, however, assuming zero friction to provide conservative estimates of the buckling load. Sousa et.al. [de Sousa et al., 2012] presented correlation studies between FE analysis and full scale testing describing the coupling between wire buckling and bird caging failure.

With reference to the above, the buckling process my be divided into two different modes:

- Radial buckling
- Lateral buckling

Radial buckling

The radial failure mode is also known as *bird-caging*, and was first observed in 1989 [Bectarte and Coutarel, 2004]. This failure mode can occur as an interaction process having contributions from the following physical effects:

1. Failure of supporting layer (anti buckling tape) as a result of the outward squeeze pressure from underlaying layers.
2. Elastic buckling without tape failure.
3. Yield failure of the wires

where the latter will be the most likely one to occur.

The first mode above is not really a buckling failure, it is simply triggered by the loss of support. When the ultimate strength of the anti buckling tape is exceeded, a sudden radial expansion of the tensile armour layers will take place. The second mode is a true buckling phenomenon which is quite similar to buckling of a straight beam on an elastic foundation.

When the annulus is flooded, there is nothing but the layers on the outside of the tensile armour to restrain radial expansion. Thereby, it is the anti buckling tape alone that must carry the radial pressure due to expansion of the tensile armour, and it is the ultimate strength of the anti buckling tape that will determine the critical external pressure.

The external pressure leads to a compressive load which further will give a contact pressure acting on the anti buckling tape, see Figure 8.29(a). By considering the hoop stress in the thin tape layer and assuming that the tensile armour and tape lay radii are approximately the same, the external axial force needed to trigger this failure mode P_{b1} of a two layered structure can be estimated as:

$$P_{b1} = \frac{R}{\tan^2 \alpha} \left[\frac{n_t \sigma_{ut} A_t \sin^2 \alpha_t}{\cos \alpha_t R_t} + 2\pi E_s \epsilon_{ut} t_s \right] \quad (8.73)$$

where R is taken as the mean radius of the tensile armour layers, ϵ_{ut} is the ultimate strain of the anti buckling tape, E_s is the sheath Young's modulus, σ_{ut} is the tape ultimate stress, n_t is the number of tape filaments, A_t is the cross-section area of the tape filament, α_t is the tape lay angle, t_s is the sheath thickness and R_t is the tape radius.

The second radial failure mode is an elastic buckling mode, as also noted by [Vaz and Rizzo, 2011], where the armour wires deflect radially in a sinusoidal pattern. The solution to a similar problem, which is buckling of a straight beam on an uniform elastic support is described in [Søreide, 1985]. The critical load can also be found based on curved beam theory and will include contributions from bending of the wire and the straining of the elastic foundation. In this case, the foundation is the anti buckling tape/outer sheath, and their stiffness will be a governing factor. In the analyses performed here, it is assumed that each wire behaves equally, meaning that there is no interaction between wires. The total number of wires are taken into account by scaling the stiffness of the supporting tape. Hence, the buckling load may be determined by looking at a single wire.

The elastic foundation stiffness c will have contributions from both the anti-buckling tape and the outer sheath. The spring stiffness contribution from the outer sheath c_1 is found from considering one wire width's contribution to the hoop stiffness found as:

$$c_1 = \frac{q_2}{u_2} = \frac{2\pi}{n} \frac{E_s t_s}{R} \cos \alpha \quad (8.74)$$

where t_s is the sheath thickness, E_s is the sheath Young's modulus and n is the number of armour wires. For the antibuckling tape, the corresponding radial stiffness parameter c_2 is determined to be:

$$c_2 = \frac{q_2}{u_2} = \frac{n_t}{n} \frac{E A_t \sin^4 \alpha_t}{R^2} \frac{\cos \alpha}{\cos \alpha_t} \quad (8.75)$$

where $E A_t$ is the tape's axial stiffness, α_t is the tape lay angle and n_t is the number of tape plies.

As the tensile armour wire is restrained from deflecting inwards due to the large stiffness of the underlying layers, it is assumed that it only deflects outwards. A possible buckling shape is shown in Figure 8.28.

By assuming a sinusoidal buckling shape:

$$u = u_0 \sin \frac{m\pi X^1}{l} \quad (8.76)$$

the critical buckling load $Q_{1,cr}$ of one single wire can be expressed by using the Principle of Minimum Potential Energy and assuming straight beam theory as:

$$Q_{1,cr} = \pi^2 E I_2 \left(\frac{m}{l} \right)^2 + \frac{c}{\pi^2} \left(\frac{l}{m} \right)^2 \quad (8.77)$$

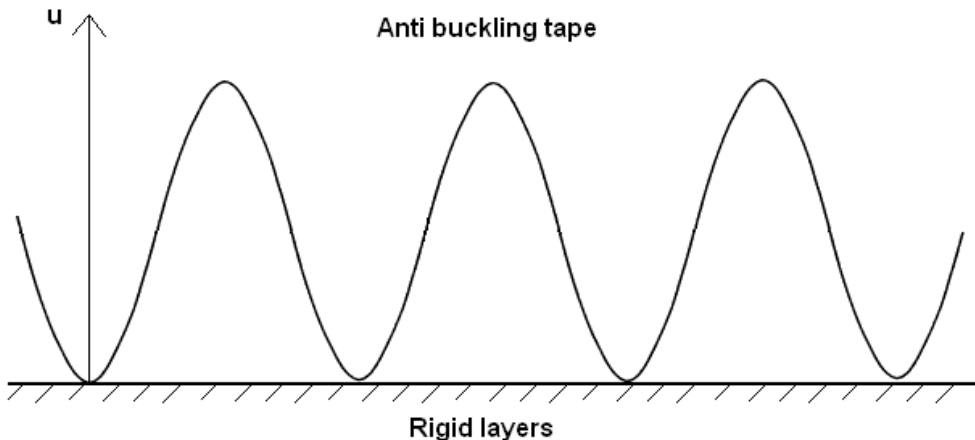


Figure 8.28: Assumed radial buckling shape

It is seen that the elastic buckling load depends strongly upon $\frac{m}{l}$, the number of half waves per unit length. The critical load will be the lowest possible, and may be found graphically by plotting the solution for different $\frac{m}{l}$ or by differentiating Eq. 8.77 with respect to $\frac{m}{l}$, which in terms of the minimum axial force in each wire needed to cause buckling gives:

$$Q_{1,cr} = 2\sqrt{EI_2c} \quad (8.78)$$

where n is the number of armour wires.

Finally, the axial load capacity including the contribution from all wires can be obtained from Eq. 8.78 as:

$$P_{b2} = n \cos \alpha Q_{1,cr} \quad (8.79)$$

The axial force leading to wire yield failure is calculated as:

$$P_{b3} = n \cos \alpha \sigma_y A \quad (8.80)$$

where σ_y is the yield stress of the wire having a cross-section area A .

Intuitively, the critical radial buckling axial force may be taken to be the smallest of the quantities P_{b1} , P_{b2} , P_{b3} from Eq. 8.73, Eq. 8.79 or Eq. 8.80. However, since it is reasonable to believe that there will be interaction between these modes of failure, an interaction formula is proposed to determine the resulting axial load that governs radial failure P_{rad} :

$$\frac{1}{P_{rad}} = \frac{1}{P_{b1}} + \frac{1}{P_{b2}} + \frac{1}{P_{b3}} \quad (8.81)$$

Three flexible pipe specimens were tested by Sousa et.al. [de Sousa et al., 2012] under axial compression until tape failure. The main characteristics of the test pipe are summarised in Table 8.1, where it is noted that the specimens were exposed to a constant compressive axial force until radial failure occurred.

The developed formulas describing radial failure are sensitive to which assumptions that are applied. With respect to the radial capacity failure as formulated in Eq. 8.73, the tape will dominate independent of whether or not the sheath is participating in the displacement process. Using Eq. 8.73, the corresponding axial force capacities are 1020 kN for the no outer sheath case and 1110 kN by including both layers. On the other hand, the sheath will influence the radial stiffness and the results obtained according to Eq. 8.79. In Table 8.2 the result from using the above equations are demonstrated with respect to assuming full or no interaction between the tape and the outer sheath. In the table the values have been normalized with respect to the average capacity encountered during the tests of 256 kN. It is seen that the straight beam assumption gives conservative results. The number of halfwaves per diameter is found to be around two, which appears to be in good agreement with the observations from the picture shown for the actual failure [de Sousa et al., 2012].

Table 8.1: FLEXIBLE PIPE DATA FROM DE SOUSA ET.AL.

Part	Parameter	4" Riser
Inner tensile layer	Outer diam. (m)	0.136
	Lay angle (deg)	35.0
	Wire size (mm)	2 x 7
	Num. of wires	47
Outer tensile layer	Outer diam. (m)	0.138
	Lay angle	-35.0
	Wire size (mm)	2 x 7
	Num. of wires	48
Steel properties	Yield str. (MPa)	1260
	E-mod. (GPa)	205
	Poisson's ratio	0.3
Anti-birdcaging tape	Outer diam. (m)	0.1384
	Lay angle (deg)	84.0
	Tape size (mm)	0.6 x 150
	Measured Young's modulus (MPa)	14900
	Measured ultimate stress (MPa)	313
	Num. of windings	2
	Ultimate stress (MPa)	144
Outer sheath	Outer diam. (m)	0.1484
	Yield stress (MPa)	20
	Young's modulus (MPa)	750
	Thickness (mm)	5.0

Table 8.2: ANALYTICAL BUCKLING FORCE VERSUS DE SOUSA ET.AL. RESULTS

Assumption	\bar{P}_2	\bar{P}_3	\bar{P}_4	$\frac{D}{L}$	\bar{P}_2^*
SB	1.24	4.33	5.36	2.14	0.82
Tape+Sheath					
SB Tape	1.04	3.98	5.36	2.13	0.72

Lateral buckling

As shown in Figure 8.29 there are two fundamental different conditions in terms of available friction acting to resist the buckling process: the intact outer sheath condition and the damaged outer sheath condition where the damaged outer sheath condition is consistent with the assumption made with respect to carcass design, see Sub-section 8.6.1. As a result of the end cap force, the two tensile armour layers will be squeezed against the anti-buckling tape creating a gap between the tensile armour layers and the pressure spiral wire. If the anti buckling tape is sufficiently strong to prevent radial buckling, the wire has only one way to go, and that is sideways. The friction forces available to resist buckling is smallest for the inner layer, hence the inner layer will loose its axial load capacity first. The buckling process will therefore be initiated in the inner layer. As the axial load capacity is reduced in the inner layer, this must be compensated by a loss in the axial compression forces in the outer layer as well to keep the cross-section in torsion balance. Hence the pipe must rotate in the same direction as the lay angle of the outer layer. Anti buckling tapes that are wound in the outer layer lay direction will therefore contribute to circumvent this behaviour by providing additional radial support acting to maintain some of the overall axial and torsion stiffness. When exposed to cyclic loading, a certain plastic rotation will, however, take place during each cycle until overall torsion failure of the cross-section occurs.

Under the assumption of no friction, a conservative estimate of the buckling pressure can be obtained from the curved beam differential equation as:

$$P_{lat} = P_1 = n \frac{\cos \alpha}{R^2} [GJ \sin^4 \alpha + (4EI_2 + EI_3 - GJ) \sin^2 \alpha \cos^2 \alpha] \quad (8.82)$$

The results from Eq. 8.82 has been compared to the test and analytical results obtained by [Østergaard, 2012] for three different pipe dimensions, see Table 8.3. It is noted that these tests were based on cyclic bending and simulating the end-cap force only, i.e. assuming damaged outer sheath condition. The test value reported in the table is further taken as the largest axial force that did not cause a grow in overall torsion deformation of the test specimen during repeated cyclic bending. It is seen that the proposed model is well correlated with the Østergaard model. The effect of friction is to increase the buckling capacity. The cyclic tests done by Østergaard shows that the maximum compressive load that can be allowed without ultimately causing pipe damage when exposed to cyclic loading is a factor 1.7-1.9 higher than the value predicted by the above equation assuming no friction.

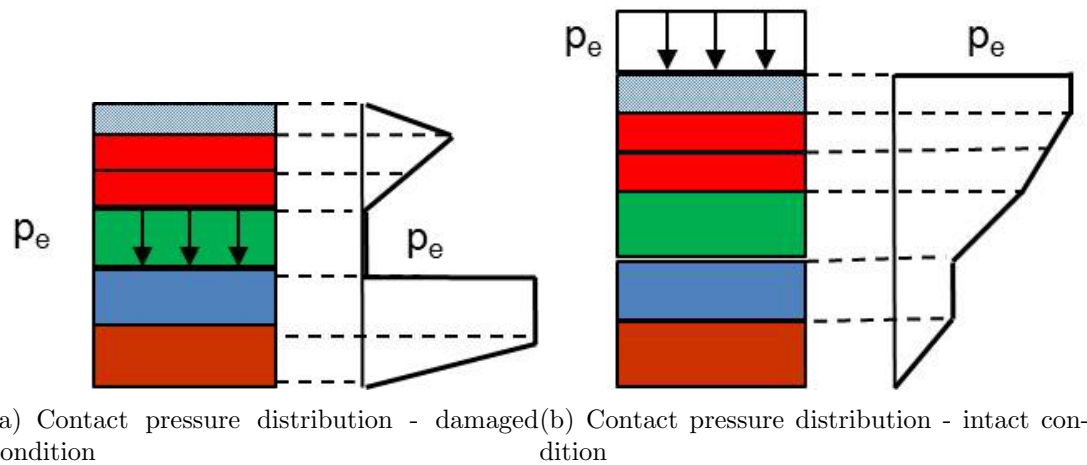


Figure 8.29: Contact pressure distributions for pipe exposed to external pressure during intact and damaged outer sheath conditions, red = tensile armour, green = pressure spiral wire, yellow= carcass, blue = plastic layer, rubber blue=antibuckling tape

Table 8.3: COMPARISON BETWEEN LATERAL BUCKLING LOADS

Case	[Østergaard, 2012] model (kN)	Proposed model (kN)	Test result (kN)
6 inch pipe	100	93	160
8 inch pipe	256	226	400
14 inch pipe	157	139	269

Wire buckling capacity

An estimate of the buckling load is then obtained as the minimum of P_{lat} and P_{rad} .

Chapter 9

Global finite element analysis

9.1 General

In the following, the tensor concept will be applied as it enables describing the stress and strain components and the related mathematical operations on them in a compact way. A scalar is a 0th order tensor (a quantity), a vector is a 1st order tensor (quantity and direction) and the stress tensor is a 2nd order tensor (quantity, direction and surface), because we need to keep track of both direction and which surface the stress components acts on. As an example σ_{11} in Figure 9.3 works on surface X_1 in the direction of X_1 . The tensor is denoted by a bold symbol $\boldsymbol{\sigma}$ and in the two-dimensional case it is written as:

$$\boldsymbol{\sigma} = \sigma_{11}\mathbf{I}_1\mathbf{I}_1 + \sigma_{12}\mathbf{I}_1\mathbf{I}_2 + \sigma_{21}\mathbf{I}_2\mathbf{I}_1 + \sigma_{22}\mathbf{I}_2\mathbf{I}_2 \quad (9.1)$$

where \mathbf{I}_i represents the base vectors along axes X_i in Figure 9.3. The component form of the Cauchy stress tensor is written σ_{ij} and in the general case the indices i and j each goes from 1 to 3 and whenever convenient these replaces letters such as x, y and z with respect to denoting scalar components in 3 dimensions.

It is noted that the stress tensor includes $3 \times 3 = 9$ components and that is also the case for the associated strain tensor $\boldsymbol{\epsilon}$. Thus the constitutive relation (material law) linking stress to strain in the general case includes 81 components ($3 \times 3 \times 3 \times 3 \times 3 = 81$) and therefore represents a 4th order tensor, each component being described by 4 base vectors and denoted \mathbf{C} .

The double product ":" between two second order tensors results in a scalar, whereas the single dot product "·" between the same tensors results in a new second order tensor.

Only systems with orthonormal (orthogonal and unit length) base vectors will be considered i.e.:

$$\begin{aligned} \mathbf{I}_i \cdot \mathbf{I}_j &= \delta_{ij} \\ \delta_{ij} &= 1 \text{ when } i = j \\ \delta_{ij} &= 0 \text{ else} \end{aligned} \quad (9.2)$$

where δ_{ij} is the Kroenecker delta [Borisenko and Tarapov, 1968].

9.2 Basics of the finite element method

FEM as applied in structural mechanics basically relies on three fundamental concepts:

- A kinematics description
- A material law
- A variation or energy principle

The kinematics is related to the relation between displacements and strain and will depend on which kinematic effects that need to be described. For beams, the basic assumption is that equilibrium is obtained by longitudinal stresses along the axis of the beam. Hence, a description of the longitudinal strain versus element node displacement and rotations are needed. In the 3D case, this means 3 displacements and 3 rotations in each element node.

The material law applicable for steel pipelines are either elastic by means of Hooke's law or elastic-plastic material models linking strain to stress along the pipe. Non-linear elastic (one to one relation between strain and stress, i.e. no hysteresis) in combination with elastic-plastic models applied in simplified spring models can further be used to describe complex pipe-soil interaction behaviour in a simplified way, enabling efficient engineering calculations.

The energy principle referred to herein is based on the Principle of Virtual Displacements *PVD*. The principle originates from the differential equation describing equilibrium of an infinitesimal element, however, by transforming this description into an integral carried out over an element of *finite size*. This is done by first multiplying the differential equation by a *virtual displacement* field $\delta\mathbf{u}$ and then integrate over the volume of the element to find the total work done within the element volume. Further by application of Green's theorem (integration by parts on general form) the integral can be transformed to describe equilibrium between external and internal forces, however, in an integrated sense. These steps are described in the following.

Green's theorem states that the volume integral of the divergence of vector field \mathbf{a} can be written as:

$$\int_V \nabla \cdot \mathbf{a} dV = \int_S \mathbf{n} \cdot \mathbf{a} dS \quad (9.3)$$

which originates from:

$$\int_V \frac{\delta}{\delta x_i} (...) dx_1 dx_2 dx_3 = \int_S (...) dS_i = \int_S (...) n_i dS \quad (9.4)$$

Application of Green's theorem for the vector field $\mathbf{a} = \boldsymbol{\sigma} \cdot \delta\mathbf{u}$, where $\boldsymbol{\sigma}$ is the two dimensional stress tensor, then results in:

$$\begin{aligned}\int_V \nabla \cdot (\boldsymbol{\sigma} \cdot \delta\mathbf{u}) dV &= \int_S \mathbf{n} \cdot \boldsymbol{\sigma} \cdot \delta\mathbf{u} dS \\ \int_V \nabla \cdot \boldsymbol{\sigma} \cdot \delta\mathbf{u} + \boldsymbol{\sigma} : \delta\nabla\mathbf{u} dV &= \int_S \mathbf{n} \cdot \boldsymbol{\sigma} \cdot \delta\mathbf{u} dS \\ \int_V \nabla \cdot \boldsymbol{\sigma} \cdot \delta\mathbf{u} dV &= -\boldsymbol{\sigma} : \delta\boldsymbol{\epsilon} dV + \int_S \mathbf{t} \cdot \delta\mathbf{u} dS\end{aligned}\quad (9.5)$$

where $\mathbf{t} = \mathbf{n} \cdot \boldsymbol{\sigma}$ represents the traction on the volume surface and $\nabla\mathbf{u} = \boldsymbol{\epsilon}$ represents the natural strain tensor.

Starting with differential equilibrium of an infinitesimal element including volume and inertia forces, this can be expressed as:

$$\nabla \cdot \boldsymbol{\sigma} + \mathbf{f} - \rho\ddot{\mathbf{u}} = 0 \quad (9.6)$$

where $\boldsymbol{\sigma}$ is the natural stress tensor defined as force divided by area in the deformed configuration (the physical stress), $\boldsymbol{\epsilon}$ is the natural strain tensor referring to the deformed configuration, ρ is the corresponding material density, \mathbf{f} is the related volume force vector field and \mathbf{u} is the displacement vector field. Since the equilibrium equation is valid in any deformed configuration, the volume and surface quantities V and S also refers to the deformed configuration. Multiplying by the virtual displacement field, taking the volume integral and application of Green's theorem as stated in Eq. 9.16, the integrated equilibrium can be stated as:

$$\begin{aligned}\int_V (\nabla \cdot \boldsymbol{\sigma} + \mathbf{f} - \rho\ddot{\mathbf{u}}) \cdot \delta\mathbf{u} dV &= 0 \\ \int_V \boldsymbol{\sigma} : \delta\boldsymbol{\epsilon} dV + \int_V \rho\ddot{\mathbf{u}} \cdot \delta\mathbf{u} dV - \int_V \mathbf{f} \cdot \delta\mathbf{u} dV - \int_S \mathbf{t} \cdot \delta\mathbf{u} dS &= 0\end{aligned}\quad (9.7)$$

The virtual displacement vector field $\delta\mathbf{u}$ is also referred to as the *test function* in the literature, see [Belytschko et al., 2001]. It is noted that the above procedure reduces the differential order, i.e. the differential equation has been transformed into its *weak form* [Belytschko et al., 2001] as it only describes equilibrium of the finite element in an integrated way. The appropriate boundary conditions at the element boundaries have been expressed in terms of surface integrals. Hence, by introducing the weight function expressed as a sum of interpolation functions that fulfills the natural kinematic and mechanical boundary conditions at the finite element boundaries, *integrated equilibrium* on element level is enforced. However, the solution within the element volume may be poor even if the integrated equilibrium is obtained. This was one of the lessons learnt during the *Sleipner* accident [Jakobsen, 1994], where one of the factors causing failure was too coarse meshing for calculating shear stresses. This is directly related to the nature of the finite element method governed by Eq. 9.7. The importance of performing mesh sensitivity tests during FEM based engineering calculations is therefore emphasised.

By introducing the material law (constitutive relation) into Eq. 9.7, the PVD expression being basis for the stiffness matrix assuming small displacements and linear material behaviour is obtained as:

$$\int_V \boldsymbol{\epsilon}^T : \mathbf{C} : \delta \boldsymbol{\epsilon} dV + \int_V \rho \ddot{\mathbf{u}} \delta \mathbf{u} dV - \int_V \mathbf{f} \cdot \delta \mathbf{u} dV - \int_S \mathbf{t} \cdot \delta \mathbf{u} dS = 0 \quad (9.8)$$

It is noted that the displacement field used in $\delta \mathbf{u}$ might not be the same as the one used to obtain $\boldsymbol{\epsilon}$. In that case the stiffness matrix will not be symmetric. In practise, the same interpolation functions are therefore applied as this will reduce the equation system and speed up the equation solver.

With regard to continuity requirements, the displacement field need to fulfill C^0 continuity, i.e. the strain field is piece-wise continuous so that the integrals in Eq. 9.7 and Eq. 9.8 are finite.

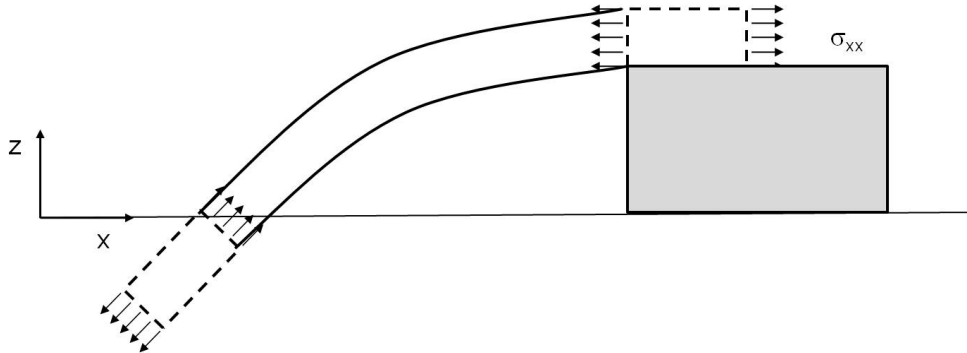


Figure 9.1: Horizontal and sloped infinitesimal element during S-lay

9.3 Non-linear effects

Pipelines and risers are long and slender structures where the structural behaviour include non-linear effects related to:

- Large displacements
- Non-linear pipe-soil interaction forces
- Non-linear material behaviour
- Non-linear hydrodynamic loading
- Variable boundary conditions
- Transient temperature and pressure loads due variable fluid flow conditions

The effect of large displacements is illustrated by considering e.g. the S-lay process where the pipe both undergoes large displacements and rotations from it's way from the lay vessel until it reaches the sea floor. The stress quantity σ_{11} referred to the global X_1 -axis and applicable for describing horizontal equilibrium of an infinitesimal element at the lay vessel need to be combined with terms describing the transformation into the sloped configuration, to describe the same equilibrium for the sloped element. This is because the stresses obviously decomposes into both X_1 and X_2 -components in the sloped configuration, as illustrated in Figure 9.1. This requires a stress measure that enables describing the rigid body motion from the horizontal to the sloped position, i.e. small displacement theory no longer suffice and we need to introduce a stress measure that is *objective* with respect to its reference, i.e. the stress should refer to the same physical stress component in the cross-section whatever rigid body motion.

The steel material behaves elastic-plastic when the strain exceeds the proportional limit. Due to the combined action of hoop stresses from internal/external pressure and

longitudinal stresses from external and internal loads, the stress state is in nature two-dimensional and hence, two-dimensional elastic-plastic material models need to be used.

The soil may behave plastic (clay) or as a Mohr-Coulomb (friction) material (sand). From a pipe structural response point of view, the effect of initial penetration on the soil resistance need to be considered together with the non-linear soil behaviour. In practise, the soil is modelled by springs that are described by a simplified non-linear spring characteristic that are based on e.g. a combination of one dimensional elastic-plastic and hyper-elastic (non-linear elastic) material models capturing the most important effects. The spring concept may also be based on more advanced material models in both the horizontal and vertical directions, see e.g. [Sotberg et al., 1994], [Carr et al., 2006], [DNVGL, 2010a] and [Aubeny et al., 2006].

The hydrodynamic loads include drag-forces that are proportional to the square of the relative velocity between the water and the pipe. In the case of wave induced current velocities, the force will also include higher order Fourier components.

The pipe undergoes different phases (empty, waterfilled, hydrotest and operation) that are characterised by differences in pipe weight. In addition, the pipeline ends may need to be connected to other structures after installation. This gives variable boundary conditions both in terms of soil and end restraint forces.

Finally, the fluid flow will introduce transients both during start-up and shut-down conditions. This may give rise to pipeline walking phenomena for short flowlines, where the pipe may move towards the cool end as a result of repeated start-up and shut-downs, see [M. Carr and Bruton, 2006] and [Chaudhury, 2010].

In order to capture all of the above effects in a consistent way, non-linear finite element analysis is needed. Therefore, following the development of computer technology, general purpose non-linear finite element codes such as ABAQUS and ANSYS have become increasingly popular within the industry to resolve pipeline design issues. More recently the tailor-made code SIMLA has been developed enabling integrated route planning and pipeline design analysis throughout all phases of installation and operation [Sævik, 2008], [Sævik et al., 2004], [Sævik, 2008], [Passano et al., 2008] and [Klæbo et al., 2008].

Most non-linear codes are founded on the same basis in terms of continuum mechanics and in the following, related issues that are of special importance for pipelines and slender structures will be elaborated in some detail. This also includes description of finite elements of special relevance.

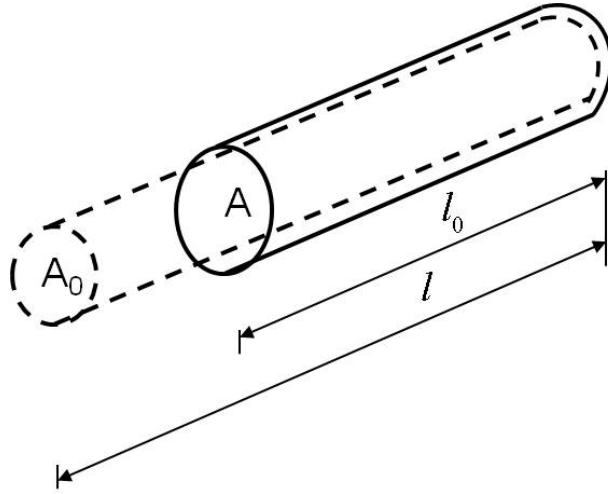


Figure 9.2: Deformed and undeformed configurations

9.4 Strain and stress measures

The *natural strain* tensor ϵ and the *Cauchy* stress tensor σ refer to the deformed volume as shown for the uniaxial case in Figure 9.2::

The Cauchy stress simply represents the true physical stress determined from the force and associated deformed area as:

$$\sigma_{11} = \frac{P}{A} \quad (9.9)$$

and the associated natural strain component is determined from integration along with the deformation process as:

$$\epsilon_{11} = \int_{l_0}^l \frac{dl}{l} = \ln\left(\frac{l}{l_0}\right) \quad (9.10)$$

However, no information on how the deformation of the body took place is yet included in this stress measure. This means that for the element prestressed to σ_{11}^0 in Figure 9.3 and thereafter undergoing a rigid body rotation of $\frac{\pi}{2}$, the scalar components will still refer to the base coordinate system (without introducing a stress measure that is able to describe arbitrary motions).

Hence, by assuming a 2-dimensional stress state and expressing the scalar components on matrix format, the Cauchy stress components before and after deformation would read:

$$\begin{bmatrix} \sigma_{11}^0 & 0 \\ 0 & 0 \end{bmatrix} \Rightarrow \begin{bmatrix} 0 & 0 \\ 0 & \sigma_{11}^0 \end{bmatrix} \quad (9.11)$$

During analysis of large deformation problems, however, we want to measure the same physical stress components along the principle cross-section axes throughout the entire

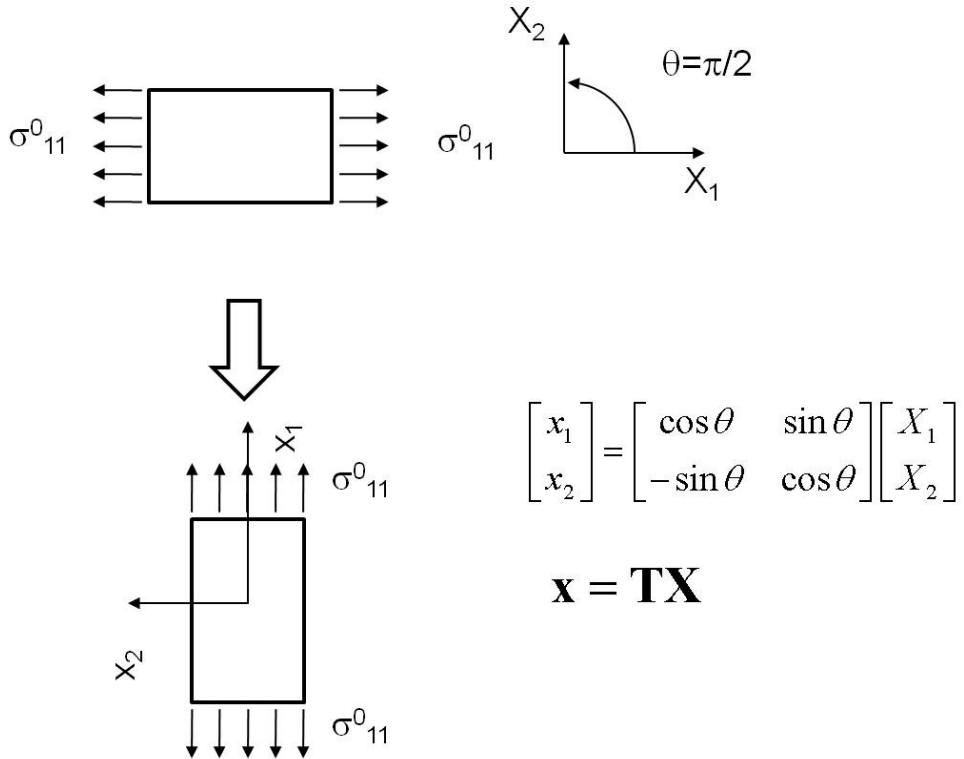


Figure 9.3: Prestressed element undergoing rigid body rotation

deformation process. This may be done by introducing the *2nd Piola Kirchoff stress tensor* \mathbf{S} and the *Green strain tensor* \mathbf{E} which both refer to the initial undeformed configuration. The Green strain tensor is established by considering the change in length dS of the line segment connecting two material particles P and Q into length ds in the deformed configuration as shown in Figure 9.4 and defined by:

$$ds^2 - dS^2 = 2d\mathbf{X} \cdot \mathbf{E} \cdot d\mathbf{X} \quad (9.12)$$

The 3×3 deformation gradient tensor is further defined as:

$$d\mathbf{x} = \mathbf{F} \cdot d\mathbf{X} \quad (9.13)$$

It is noted that no if no strains are introduced, \mathbf{F} only describes rigid body motion as the transformation between two coordinate systems, i.e. it specialises into the ordinary orthonormal transformation matrix, i.e. $\mathbf{T} = \mathbf{F}$ and in that case $\mathbf{F}^{-1} = \mathbf{T}^T$

The above gives:

$$ds^2 - dS^2 = d\mathbf{x} \cdot d\mathbf{x} - d\mathbf{X} \cdot d\mathbf{X} = d\mathbf{X} \cdot \mathbf{F}^T \cdot \mathbf{F} \cdot d\mathbf{X} - d\mathbf{X} \cdot d\mathbf{X} \quad (9.14)$$

and

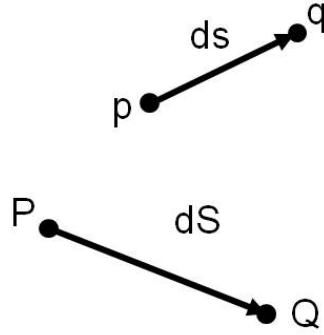


Figure 9.4: The deformation of the line segment P-Q

$$\mathbf{E} = \frac{1}{2}(\mathbf{F}^T \cdot \mathbf{F} - \mathbf{1}) \quad (9.15)$$

The component form can be expressed in terms of displacement components as:

$$\begin{aligned}
 E_{ij} \mathbf{I}_i \mathbf{I}_j &= \frac{1}{2} \left(\frac{\partial x_j}{\partial X_i} \mathbf{I}_i \mathbf{I}_j \cdot \frac{\partial x_k}{\partial X_l} \mathbf{I}_k \mathbf{I}_l - \delta_{ij} \mathbf{I}_i \mathbf{I}_j \right) \\
 &= \frac{1}{2} \left(\frac{\partial(X_j + u_j)}{\partial X_i} \mathbf{I}_i \mathbf{I}_j \underbrace{\cdot \frac{\partial(X_k + u_k)}{\partial X_l} \mathbf{I}_k \mathbf{I}_l}_{-\delta_{ij}} - \delta_{ij} \mathbf{I}_i \mathbf{I}_j \right) \\
 &= \frac{1}{2} \left(\frac{\partial(X_j + u_j)}{\partial X_i} \mathbf{I}_i \frac{\partial(X_j + u_j)}{\partial X_l} \mathbf{I}_l - \delta_{ij} \mathbf{I}_i \mathbf{I}_j \right) \\
 &= \frac{1}{2} \left(\frac{\partial(X_k + u_k)}{\partial X_i} \frac{\partial(X_k + u_k)}{\partial X_j} \mathbf{I}_i \mathbf{I}_j - \delta_{ij} \mathbf{I}_i \mathbf{I}_j \right) \quad (9.16) \\
 &= \frac{1}{2} \left(\frac{\partial(X_k + u_k)}{\partial X_i} \frac{\partial(X_k + u_k)}{\partial X_j} - \delta_{ij} \right) \mathbf{I}_i \mathbf{I}_j \\
 &= \frac{1}{2} \left(\delta_{ij} + \frac{\partial u_k}{\partial X_i} \frac{\partial X_k}{\partial X_j} + \frac{\partial X_k}{\partial X_i} \frac{\partial u_k}{\partial X_j} + \frac{\partial u_k}{\partial X_i} \frac{\partial u_k}{\partial X_j} - \delta_{ij} \right) \mathbf{I}_i \mathbf{I}_j \\
 &= \frac{1}{2} \left(\frac{\partial u_j}{\partial X_i} + \frac{\partial u_i}{\partial X_j} + \frac{\partial u_k}{\partial X_i} \frac{\partial u_k}{\partial X_j} \right) \mathbf{I}_i \mathbf{I}_j
 \end{aligned}$$

For the uniaxial case (bar element) the result can be obtained by only studying the change in element length as:

$$E_{11} = \frac{l^2 - l_0^2}{2l_0^2} \quad (9.17)$$

In order for the Green strain and 2nd Piola Kirchoff stress measures to describe the same amount of work as the Cauchy stress and natural strain we must have:

$$\int_V \boldsymbol{\sigma} : \delta \boldsymbol{\epsilon} dV = \int_{V_0} \boldsymbol{S} : \delta \boldsymbol{E} dV_0 \quad (9.18)$$

Considering mass balance:

$$\rho V = \rho_0 V_0 \quad (9.19)$$

Further by noting that the natural strain can be expressed by the Green strain by the transformation:

$$\delta \boldsymbol{E} = \boldsymbol{F}^T \cdot \delta \boldsymbol{\epsilon} \cdot \boldsymbol{F} \quad (9.20)$$

we can write:

$$\int_V \boldsymbol{\sigma} : \delta \boldsymbol{\epsilon} dV = \frac{\rho_0}{\rho} \int_{V_0} \boldsymbol{\sigma} : (\boldsymbol{F}^{-T} \cdot \delta \boldsymbol{E} \cdot \boldsymbol{F}^{-1}) dV_0 = \quad (9.21)$$

$$\frac{\rho_0}{\rho} \int_{V_0} (\boldsymbol{F}^{-1} \cdot \boldsymbol{\sigma} \cdot \boldsymbol{F}^{-T}) : (\delta \boldsymbol{E}) dV_0 = \int_{V_0} \boldsymbol{S} : \delta \boldsymbol{E} dV_0 \quad (9.22)$$

and then:

$$\boldsymbol{S} = \frac{\rho_0}{\rho} \boldsymbol{F}^{-1} \cdot \boldsymbol{\sigma} \cdot \boldsymbol{F}^{-T} \quad (9.23)$$

which in the uniaxial case gives:

$$S_{11} = \frac{Al}{A_0 l_0} \frac{l_0}{l} \cdot \sigma_{11} \cdot \frac{l_0}{l} = \frac{A\sigma_{11}}{A_0} \frac{l_0}{l} \quad (9.24)$$

Since the strains are based on the change in length described as the squared sum of components in Eq. 9.12 (as in Pythagoras), rigid body motions will not contribute to the measured strains. Further, by noting that in that case, the deformation gradient \boldsymbol{F} specialises into the transformation matrix \mathbf{T} defined in Figure 9.3 and by application of Eq. 9.23, the components of \boldsymbol{S} are obtained as:

$$\begin{bmatrix} 0 & -1 \\ 1 & 0 \end{bmatrix} \begin{bmatrix} 0 & 0 \\ 0 & \sigma_{11}^0 \end{bmatrix} \begin{bmatrix} 0 & 1 \\ -1 & 0 \end{bmatrix} = \begin{bmatrix} \sigma_{11}^0 & 0 \\ 0 & 0 \end{bmatrix} \quad (9.25)$$

Hence, the 2nd Piola Kirchhoff stress tensor is seen to be objective with respect to its reference, i.e. it is capable of describing the same physical stress component, whatever, rigid body motion. The Green strain and the 2nd Piola Kirchhoff stress tensor therefore represent a convenient basis for analysis of structures undergoing large rigid body motions such as pipelines and risers. It is noted that since the stress measure refers to the initial volume, input material curves in the form of true (Cauchy) stress and natural strain should be transformed into consistent format before use. This is normally not a big issue since the maximum strain allowed for in such structures are in the range 1-2% and the associated volume and area changes are small.

It should, however, be noted that the above applies for global analysis for design checks. In order to simulate the entire cross-section collapse process, large strains may be involved and in that case similar formulations that are based on the Cauchy stress and natural strain concept are more suited.

9.5 Non-linear finite element methods

9.5.1 Equilibrium equation

With reference to Eq. 9.8 equilibrium in terms initial volumes, Green strain and 2nd Piola Kirchoff stress can be expressed as:

$$\int_V \mathbf{S} : \delta \mathbf{E} dV_0 + \int_V \rho_0 \ddot{\mathbf{u}} \cdot \delta \mathbf{u} dV_0 - \int_V \mathbf{f}_0 \cdot \delta \mathbf{u} dV_0 - \int_S \mathbf{t}_0 \cdot \delta \mathbf{u} dS_0 = 0 \quad (9.26)$$

where subscript 0 refers to the initial state. Internal/external pressure can be handled based on thin shell theory which means that the pressure will always act normal to the surface and only act on the deformed surface area expressed as $(1+E_{11}+E_{22})dS_0$. Since the load will change as a result of the structure's deformation, it is said to be *non-conservative*. One of the consequences of the appearance of the so called load correction stiffness matrix, which is un-symmetric [Mathisen, 1990].

9.5.2 Non-linear Finite Element Formulations

In non-linear structural analysis there are several possible formulations::

1. The Total Lagrangian formulation (TL)
2. The Corotated Total Lagrangian formulation (CTL)
3. The Updated Lagrangian formulation (UL)
4. The Corotated Updated Lagrangian formulation (CUL)

In TL and CTL the independent variables are the Lagrangian coordinates, X^k , fixed to the material point P and the time t . The Green strain tensor in combination with the 2nd Piola Kirchoff stress is applied, always referring back to the initial undeformed configuration. In TL all quantities are developed from the initial global reference coordinate system and using the full expressions for the quadratic terms in the Green strain tensor resulting from Eq. 9.12. This means that the components of stress will represent the same physical quantity throughout deformation. Higher order terms may be neglected when forming the stiffness matrix, however, fairly complicated expressions result both for stiffness and equilibrium forces.

CTL originates from the early work by [Bergan, 1971] and as opposed to the former this method requires a local coordinate system attached to each element from which the element deformations and forces are referred. This is illustrated in Figure 9.5. Rigid body motions are removed and the strains are calculated relative to the attached element system. The transformation matrix between the local element and global systems \mathbf{T} need to be continuously updated for each element to allow transformation from/to the global system. This is avoided in TL, however, to the cost of lengthy stress and stiffness matrix

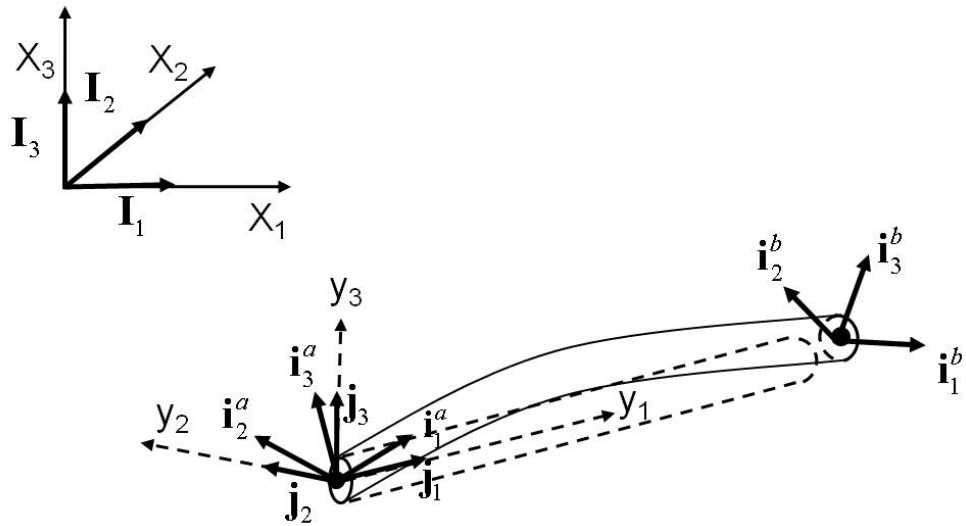


Figure 9.5: 3D beam element in CTL formulation

expressions needed to capture large motions (e.g. the information contained in \mathbf{T} for CTL). In many cases (as for risers and pipelines), the displacements relative to the local system can be assumed small and the higher order components of the Green strain tensor can be neglected both when updating the stiffness matrix and the stresses. This eases finite element implementation. However, since the 2nd Piola Kirchoff stress refers back to the initial volume, TL and CTL are not suited for large strain problems where e.g. the stress-strain curve must be based on the deformed area.

In UL and CUL the independent variables are the spacial coordinates x^k that at time t had position X^k at $t = 0$. The natural stain and the Cauchy stress tensor are used both referring to the last deformed state. This allows large deformation problems to be analysed, however, a vector description allowing the element to deform is needed. This requires significant computational efforts specially for CUL. CUL is therefore rarely referred to in the literature.

TL, CTL and UL have been successfully used in many non-linear problems; see e.g. [Søreide, 1989], [Levold, 1990], [Hibbit et al., 1970], [McMeeking et al., 1975], [Oden, 1972], [Bathe, 1982], [Bergan, 1971], [Søreide, 1973] and [Mattiaison, 1983]. Note that the formulations are theoretically equivalent if no approximations are introduced.

CTL is well suited for analysis of slender structures undergoing moderate strains and is applied as basis for RIFLEX [Fylling et al., 1995], BFLEX [Sævik, 2010], USAP [Sævik and Gjøsteen, 2010] and SIMLA [Sævik, 2008]. The element reference system do not deform, however, it follows the element throughout whatever rigid body motion. This is obtained by rigidly connecting a base vector system to each node and updating the position and orientation of this base vector system from the assumption of small incremental rotation at each load step, see [Argyris, 1982].

In Figure 9.5 the beam element reference system \mathbf{j}_i is obtained by combining the tangent vector connecting the two nodes at the updated coordinate position with the current orientation of the element end node base vectors \mathbf{i}_i^a and \mathbf{i}_i^b . The element rotational deformation at each end is then measured from the relative difference between the \mathbf{i}_i^a , \mathbf{i}_i^b and \mathbf{j}_i systems. The axial strain is computed directly from Eq. 9.17 whereas bending deformation is calculated by first eliminating rigid body motion and then measure the deformation relative to the attached element system. Large displacements and rigid body motions are hence taken care of by continuously updating the element end nodes orientation and end coordinate positions followed by subsequent transformations between the local systems and global system.

In order to solve the non-linear equations incremental and iterative solution procedures are needed. This requires the stiffness matrix to be expressed on incremental form. This is obtained by studying the virtual work in an infinitesimal increment Δ as follows, where only static terms are included and volume forces are neglected to illustrate the principle:

$$\int_V \mathbf{C} : (\mathbf{E} + \Delta\mathbf{E}) : \delta(\mathbf{E} + \Delta\mathbf{E}) dV_0 - \int_S (\mathbf{t}_0 + \Delta\mathbf{t}_0) \cdot \delta\mathbf{u} dS_0 = 0 \quad (9.27)$$

By subtracting the relevant terms of Eq. 9.26 from Eq. 9.27, neglecting higher order terms in Δ and by assuming that the difference between two neighbouring equilibrium states is small, the following expression for the incremental equation (applicable for the non-linear equation solution procedure) is obtained:

$$\int_V \mathbf{C}_T : \Delta\mathbf{E} : \delta\mathbf{E} dV_0 + \int_V \mathbf{S} : \delta\Delta\mathbf{E} dV_0 - \int_S \Delta\mathbf{t}_0 dS_0 = 0 \quad (9.28)$$

where \mathbf{C}_T represent the tangential material law valid for the next increment, see 9.5.3. Eq. 9.28 gives the incremental equilibrium equation to be used as basis for the tangential stiffness needed in the iterative solution procedure. The first term gives the material stiffness matrix, whereas the second term is often referred to as the geometric stiffness matrix. However, a more precise definition is the initial stress matrix as it has nothing to do with geometry, rather the effect of the present stress level with respect to an increment in displacement.

For the CTL formulation rigid body motions are eliminated and higher order terms in \mathbf{E} may be neglected since the deformation is small relative to the attached element coordinate system.

9.5.3 Material law - Plasticity for metals

Pipelines are long and slender structures that can be described by beam theory, i.e. only longitudinal stresses govern equilibrium. This rests on the assumption that the deformations in the cross-section plane are small which will be valid in most practical design cases. However, the effect of internal and external pressure with respect to the longitudinal strain and material yielding need to be taken into account. This in combination with the findings

of Section 6.3.1, noting that the stress resultant need to be based on integration of the entire area including the pressurised section, implies that special taylor made beam elements considering these effects are needed, hereafter termed *pipe* elements. Assuming elastic material behaviour, the two-dimensional version of Hooke's law assuming plane stress (no constraints in the 3-direction) reads:

$$\begin{bmatrix} S_{11} \\ S_{22} \\ S_{12} \end{bmatrix} = \frac{E}{1-\nu^2} \begin{bmatrix} 1 & \nu & 0 \\ \nu & 1 & 0 \\ 0 & 0 & \frac{1-\nu^2}{2(1+\nu)} \end{bmatrix} \begin{bmatrix} E_{11} \\ E_{22} \\ E_{12} \end{bmatrix} \quad (9.29)$$

For pipe elements the simplification is further introduced that the hoop (circumferential) stress S_{22} is known by thin shell theory, hence the hoop strain E_{22} can be calculated directly and no extra degrees of freedom are needed to describe the hoop effect. This means that we can represent the pipeline by beam degrees of freedom describing the longitudinal stress state only.

However, since, plastic strains are allowed to occur for pipelines, the effect of material softening beyond the stress proportionality limit needed to be included. This requires application of plasticity theory for metals which is based on the following principles:

1. The total strain can be divided into one elastic and one plastic component:

$$\boldsymbol{E} = \boldsymbol{E}^e + \boldsymbol{E}^p \quad (9.30)$$

2. The elastic strain can always be calculated by the elastic material law (stated for 2 dimensions and plane stress in Eq. 9.29):

$$\boldsymbol{E}^e = (\boldsymbol{C}^e)^{-1} : \boldsymbol{S} \quad (9.31)$$

3. The plastic strain is calculated based on:

- (a) A yield criterion
- (b) A flow rule
- (c) A hardening rule

The yield criterion for metals can be expressed in terms of the Von Mises stress criterion on the form.

$$\begin{aligned} \sqrt{S_{11}^2 + S_{22}^2 + S_{33}^2 - S_{11}S_{22} - S_{22}S_{33} - S_{11}S_{33} + 3S_{12}^2 + 3S_{13}^2 + 3S_{23}^2} - H(\bar{\boldsymbol{E}}^p) &= 0 \\ \bar{\boldsymbol{S}} - H(\bar{\boldsymbol{E}}^p) &= 0 \\ \sqrt{\frac{3}{2} \boldsymbol{S}' : \boldsymbol{S}' - H(\bar{\boldsymbol{E}}^p)} &= 0 \\ f(\boldsymbol{S}', \bar{\boldsymbol{E}}^p) &= 0 \end{aligned} \quad (9.32)$$

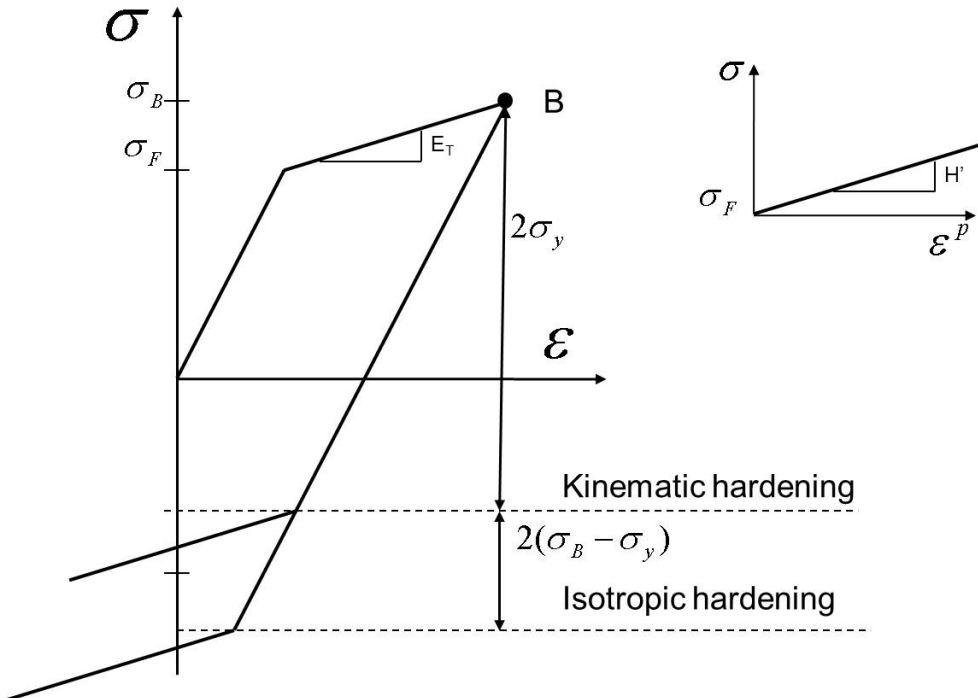


Figure 9.6: Illustration of kinematic and isotropic hardening for the uni-axial case

where \mathbf{S}' represents the deviatoric stress defined by:

$$\mathbf{S}' = \mathbf{S} - \frac{1}{3} S_{ii} \quad (9.33)$$

and $\bar{\mathbf{E}}^p$ is the equivalent plastic strain used to describe material hardening defined by:

$$\bar{\mathbf{E}}^p = \sqrt{\frac{2}{3} \mathbf{E}^p : \mathbf{E}^p} \quad (9.34)$$

H is a hardening function describing how the yield stress develops after the yielding starts to occur, see Figure 9.6

The consistency condition is further introduced to ensure that the stress value is always kept on the yield surface, which by including the effect of strain hardening can be expressed by:

$$df = \nabla_{\mathbf{S}} f : d\mathbf{S} + \frac{\partial f}{\partial \bar{\mathbf{E}}^p} d\bar{\mathbf{E}}^p = \nabla_{\mathbf{S}} f : d\mathbf{S} + H' d\bar{\mathbf{E}}^p = 0 \quad (9.35)$$

The flow rule is normally based on Drucker's postulate for a stable material, where the following must be satisfied:

1. The yield surface is convex, so that the surface normal points outwards.

2. The plastic strain increment is parallel to the yield surface normal
3. The plastic strain increment is a linear function of the stress increment.

The above requirements can be summarised into:

$$dE_{ij}^p = d\lambda \frac{\partial f}{\partial S_{ij}} = d\lambda \frac{3}{2} \frac{S'_{ij}}{\bar{S}} \quad (9.36)$$

where $d\lambda$ is a scaling factor.

By application of Eq. 9.30, Eq. 9.31, Eq. 9.35 and Eq. 9.36, the tangential constitutive equation for the elasto-plastic material based on the multiaxial Von Mises yield surface assumption is obtained as:

$$dS_{ij} = \underbrace{\left[C_{ijkl}^e - \alpha 3G \frac{S'_{ij} S'_{kl}}{S_e^2 \left(1 + \frac{H'}{3G} \right)} \right]}_{D_{ijkl}} dE_{kl} \quad (9.37)$$

where:

$$\alpha = 1 \quad \text{if} \quad \frac{\partial f}{\partial \mathbf{S}} : \Delta \mathbf{S} \geq 0 \quad \text{and} \quad f = 0 \quad (9.38)$$

$$\alpha = 0 \quad \text{if} \quad \frac{\partial f}{\partial \mathbf{S}} : \Delta \mathbf{S} < 0 \quad \text{or} \quad f < 0 \quad (9.39)$$

$$(9.40)$$

The hardening rule describes the hardening of the material after plastic deformation starts. During unloading two descriptions are often applied:

1. Kinematic hardening – the distance between the yield limit points never exceeds 2*yield stress.
2. Isotropic hardening where the material *remembers* the hardening prior to unloading.

These two principles are illustrated in Figure 9.6. Most metals behave somewhere between these two approaches and the application may determine which of them to be used. The kinematic hardening give raise to the so-called *Bauschinger effect*. This means that the yield capacity during unloading is less than it was initially. If the application allows no yielding during reversed loading, this must be considered. In some cases, the strength is recovered if reversed plastic deformation can be allowed. In this case isotropic hardening may be used.

Example 9.5.1 One dimensional plasticity - How to obtain incremental strain-stress relationship

Yield criterion:

$$f = \sigma - \sigma_F = 0$$

Flow rule:

$$\sigma_F = H(\varepsilon^p)$$

Apply consistency condition:

$$df = \frac{\partial f}{\partial \sigma} d\sigma - \frac{\partial \sigma_F}{\partial \varepsilon^p} d\varepsilon^p = \frac{\partial f}{\partial \sigma} d\sigma - H' d\varepsilon^p = 0$$

where a constant hardening parameter H' has been assumed, see Figure 9.6.

Then applying the assumption that the plastic strain increment is parallel to the yield surface normal, i.e. the strain increases in the same direction as the stress:

$$d\varepsilon^p = d\lambda \frac{\partial f}{\partial \sigma} = d\lambda \cdot 1$$

The consistency condition then gives:

$$d\varepsilon^p = \frac{d\sigma}{H'}$$

which combined with the elastic material law and the decomposition into two strain components gives:

$$d\sigma = E \left(1 - \frac{E}{H' + E}\right) d\varepsilon = E_T d\varepsilon$$

Example 9.5.2 The following example is made to illustrate the effect of kinematic and isotropic hardening as well as the effect of having a 2-dimensional stress state in terms of reducing the moment capacity of the cross section. The pipe selected is a 711.2 mm inner diameter (ID) pipe with a diameter to thickness ratio (D/t) of 20. The pipe is modelled with 2 elements along the pipe axis and it is fixed in translation except for the longitudinal direction of the right end (free to slide). At each end, a positive and negative, prescribed rotation is applied to give a constant curvature with an outer fibre strain amplitude of 0.3 %. The steel material selected is X65 with a Specified Minimum Yield Stress (SMYS) at 0.5% strain of 448 MPa. The model and material curve is illustrated in Figure 9.7 (a) and Figure 9.7 (b). The numerical integration carried out to calculate the stress resultants and stiffness matrix is based on having 16 integration points over the cross-section and at 3 Lobatto sections along the pipe, i.e. altogether 48 intergation points along each finite element.

The results in terms of bending moment versus curvature comparing isotropic and kinematic hardening is shown in Figure 9.8 (a). A significant capacity reduction is seen on the compressive side when applying the kinematic hardening rule. This is referred to as the Bauschinger effect in the literature.

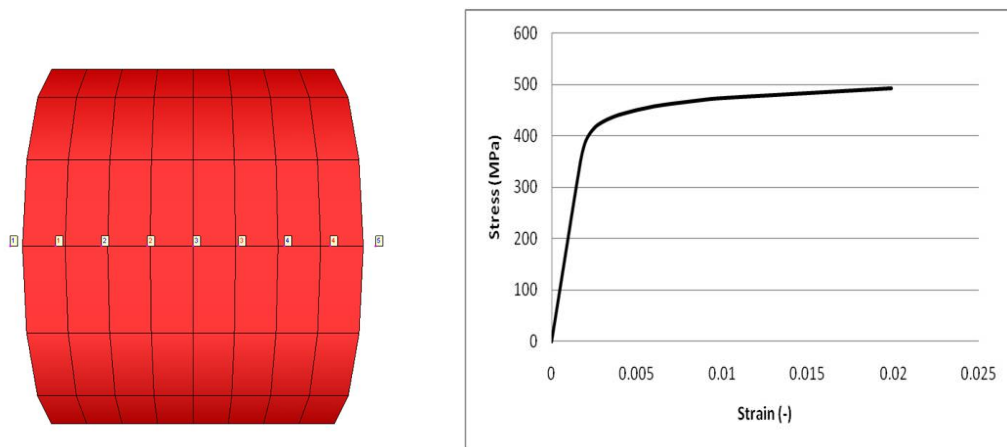


Figure 9.7: FEM model and material curve

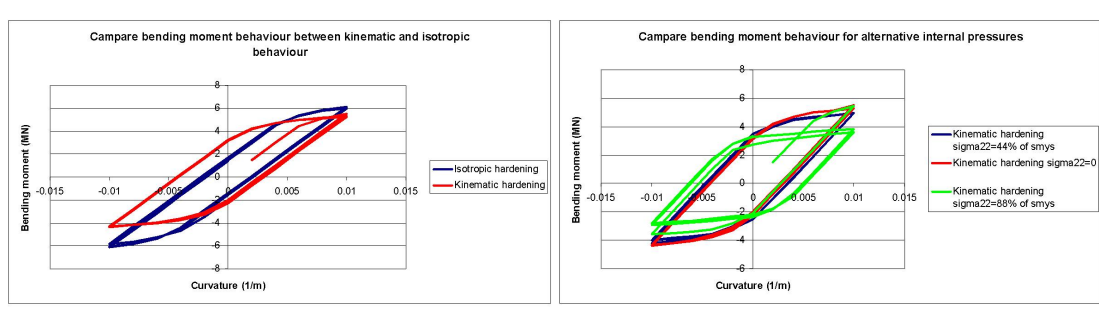


Figure 9.8: The effect of applying alternative hardening models and internal pressures on the moment capacity

For the kinematic hardening case, the effect of applying internal pressure resulting in a hoop stress of 44 % and 88 % of the yield stress are shown. It is seen that for the 88 % case, there is a significant moment capacity reduction.

9.5.4 Solution techniques

General

The basic principle of all structural analysis is to ensure equilibrium between external forces and the internal reaction , mass and damping forces. For the static case we write:

$$\mathbf{g}(\mathbf{R}_{ext}, \mathbf{r}) = \mathbf{R}_{ext} - \mathbf{R}_{int} = \lambda \mathbf{R}_{ref} - \mathbf{R}_{int} = \mathbf{0} \quad (9.41)$$

where \mathbf{R}_{int} represent the vector of internal element reaction forces which is a function of the displacements \mathbf{r} and \mathbf{R}_{ext} represents the external load vector often represented by a reference vector \mathbf{R}_{ref} and a user defined scalar function $\lambda(t)$. There are alternative ways of solving the above equations including standard load incrementation methods and advanced automatic or semi-automatic procedures.

Standard load incrementation methods

For the standard method, the load increments are normally user controlled by means of the reference value for the load \mathbf{R}_{ref} and the associated non-linear scalar function (load history) λ noted above and as defined in Eq. 9.41. The standard load incrementation methods may be combined with the following solution procedures:

1. Euler-Cauchy incrementation without equilibrium iterations
2. Incrementation with Newton-Raphson iteration
3. Incrementation with modified Newton-Raphson iteration

The Euler-Cauchy incrementation procedure is illustrated in Figure 9.9. The load is incremented in steps and the stiffness matrix is updated at the end of each step. Since the displacement increment is a result of the stiffness at the start of the increment, there will be a deviation between the external load and the the internal element forces due to the change in stiffness within the increment. This deviation will tend to increase when applying more increments, i.e. by moving along the force-displacement curve between two equilibrium states I and II as illustrated in Figure 9.9.

The only way of reducing the deviation by applying this procedure would be by reducing the increment size. A more accurate method would, however, be by performing iterations to close the gap between the internal and external forces at each load step. One way of doing this is by performing a Newton-Raphson iterative procedure at each load step. The Newton-Raphson method is based on utilizing the tangent to the function g as illustrated in Figure 9.10 for the one-dimensional case as:

$$r^{i+1} = r^i - \frac{g(r)}{\tan \theta} = r^i - \frac{g(r)}{\frac{\partial g}{\partial r}} \quad (9.42)$$

where i is the iteration number. In the multidimensional case:

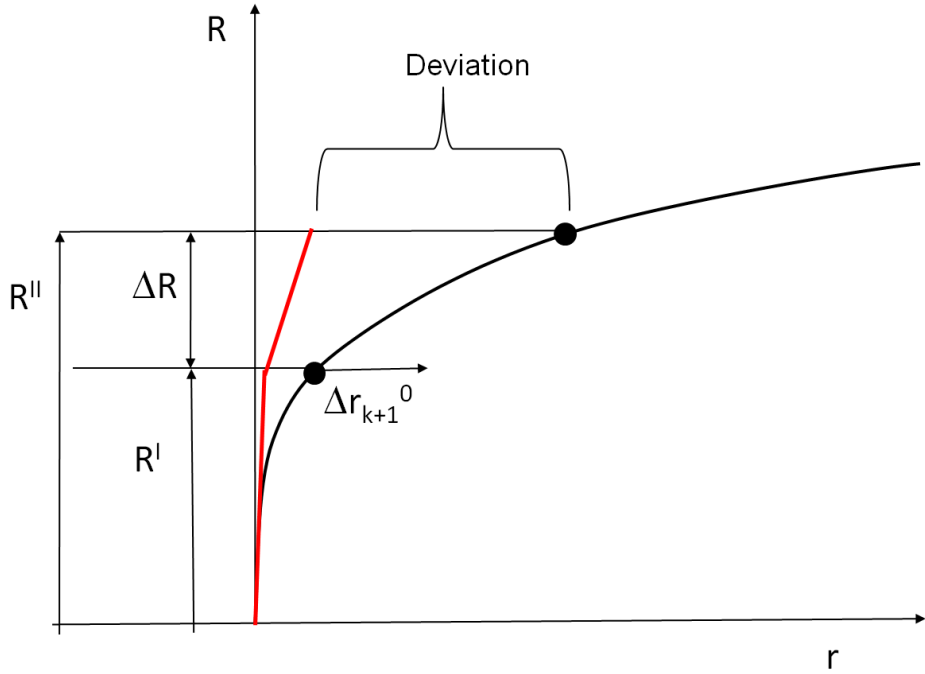


Figure 9.9: Illustration of Euler-Cauchy incrementation procedure

$$\mathbf{r}^{i+1} = \mathbf{r}^i - \frac{\mathbf{g}(\mathbf{r})}{\frac{\partial \mathbf{g}}{\partial \mathbf{r}}} \quad (9.43)$$

which means:

$$\Delta \mathbf{r} = -\frac{\mathbf{g}(\mathbf{r})}{\frac{\partial \mathbf{g}}{\partial \mathbf{r}}} \quad (9.44)$$

and from Eq. 9.43:

$$\frac{\partial}{\partial \mathbf{r}} \mathbf{g}(\mathbf{R}_{ext}, \mathbf{r}) = \frac{\partial}{\partial \mathbf{r}} (\mathbf{R}_{ext} - \mathbf{R}_{int}) = 0 - \frac{\partial \mathbf{R}_{int}}{\partial \mathbf{r}} = -\mathbf{K}_T \quad (9.45)$$

and hence:

$$\Delta \mathbf{r}^{i+1} = \mathbf{K}_T^{-1,i} (\mathbf{R}_{ext,k+1} - \mathbf{R}_{int,k}^i) \quad (9.46)$$

where the tangential stiffness matrix \mathbf{K}_T and the vector of internal forces \mathbf{R}_{int} both are functions of the state of deformation. The index k means load step number, i.e. $k+1$ means equilibrium state II and k means state I referring to the figure. During the full Newton-Raphson iteration \mathbf{K}_T is updated for each iteration, see Figure 9.11 (a). Alternatively, \mathbf{K}_T is updated at each load step only, which is termed *modified Newton-Rapshon* iteration, see Figure 9.11 (b). In that case more iterations will be needed, however, this has to be measured against the savings related to not updating \mathbf{K}_T for each iteration.

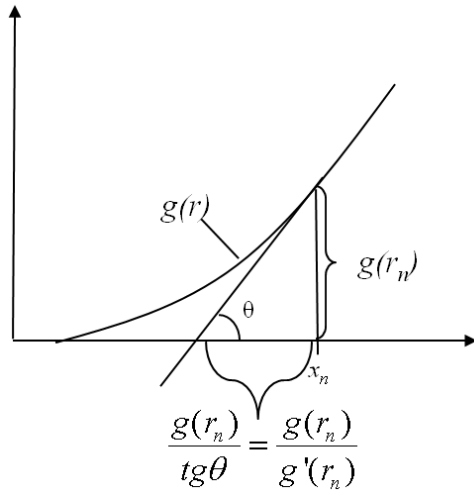


Figure 9.10: The concept of Newton-Raphson iteration

Advanced solution procedures

In many cases the structural behaviour may include different kinds of instability phenomena where the system stiffness get singular and the structural capacity of carrying loads actually reduces as a function of deformation. Such behaviour is illustrated in Figure 9.12.

In order to enable a structural analysis to be successfully completed throughout the response space for the 5 last examples of Figure 9.12, where the structural capacity actually reduces as the deformation increases, requires the external load to be automatically adjusted to the internal reaction forces of the structure. This requires special algorithms of which arc length methods have become standard in most computer codes. The main essence of arc length methods is that the load scaling parameter λ used in Eq. 9.41 become unknown and need to be automatically adjusted to fulfil constraints with regard to how large displacements that can be accepted for each increment. The deviation a between the distance along the load displacement space obtained for one increment and a predefined length Δl should be zero, which can be formulated as:

$$a = \Delta \mathbf{r}^T \Delta \mathbf{r} + \Delta \lambda^2 \psi^2 \mathbf{R}_{ref}^T \mathbf{R}_{ref} - \Delta l^2 = 0 \quad (9.47)$$

where ψ is a scaling parameter (e.g. obtained from the response experienced by the system up to now) transforming the force increment into displacements. In the following the symbol Δ refers to the load /displacement increment which during subsequent iterations changes by an amount denoted δ until it reaches it's final value for each load step. At any equilibrium state completed by successful iterations we have:

$$\mathbf{g}(\lambda, \mathbf{r}) = \lambda \mathbf{R}_{ref} - \mathbf{R}_{int} = \mathbf{0} \quad (9.48)$$

As noted above when moving into a new equilibrium state we first carry out a trial

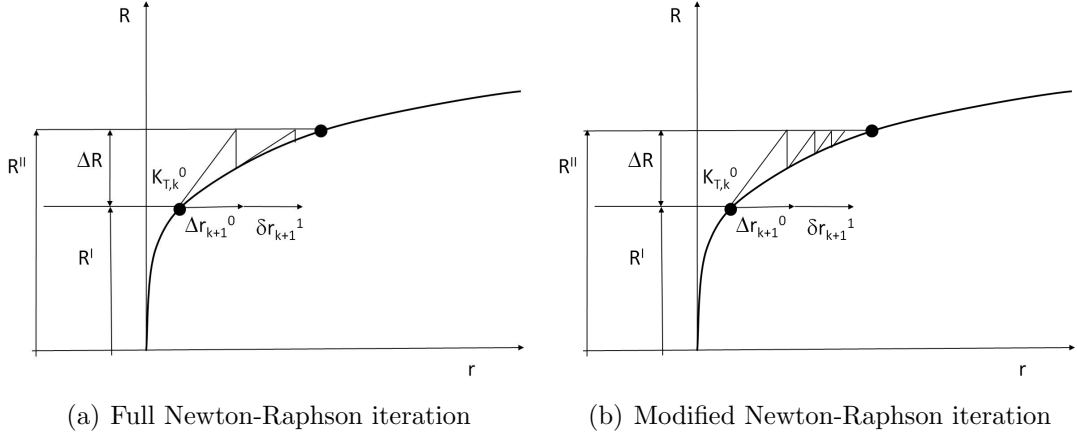


Figure 9.11: Illustration of the Newton-Raphson iterative procedure

increment and then perform subsequent iterations. The change in \mathbf{g} from the old value denoted by subscript 0 to its new target value (that always should be zero) denoted by n can be expressed by a Taylor serie, only including the first order terms as:

$$\mathbf{g}_n = \mathbf{g}_0 + \frac{\partial \mathbf{g}}{\partial \mathbf{r}} \delta \mathbf{r} + \frac{\partial \mathbf{g}}{\partial \lambda} \delta \lambda = \mathbf{g}_0 - \mathbf{K}_T \delta \mathbf{r} + \mathbf{R}_{ref} \delta \lambda = 0 \quad (9.49)$$

and in the same way by differentiation of Eq. 9.47:

$$a_n = a_0 + 2\Delta \mathbf{r}^T \delta \mathbf{r} + 2\Delta \lambda \delta \lambda \psi^2 \mathbf{R}_{ref}^T \mathbf{R}_{ref} = 0 \quad (9.50)$$

By combining these two equations, the change in $\delta \mathbf{r}$ and $\delta \lambda$ can be solved as a function of the initial increment as:

$$\begin{bmatrix} \delta \mathbf{r} \\ \delta \lambda \end{bmatrix} = - \begin{bmatrix} -\mathbf{K}_T & \mathbf{R}_{ref} \\ 2\Delta \mathbf{r}^T & 2\Delta \lambda \psi^2 \mathbf{R}_{ref}^T \mathbf{R}_{ref} \end{bmatrix}^{-1} \begin{bmatrix} \mathbf{g}_0 \\ a_0 \end{bmatrix} \quad (9.51)$$

However, since this equation system is either symmetric or banded, more efficient methods such as *linear arc length methods* are normally applied. These are obtained by rearranging Eq. 9.50 into:

$$-\frac{a_0}{2} = \Delta \mathbf{r}^T \delta \mathbf{r} + \Delta \lambda \delta \lambda \psi^2 \mathbf{R}_{ref}^T \mathbf{R}_{ref} \quad (9.52)$$

where a_0 is the old value of the arch length mismatch. If a_0 is set to zero, the Ramms's and Riks-Wempner's methods as illustrated in Figure 9.13 are obtained. In Ramm's method the increment used as basis for the equation is updated during iteration which means that the iterative change is orthogonal to the secant change. In Riks-Wempner's method the initial predictor increment is used and the iterative change is always normal to this.

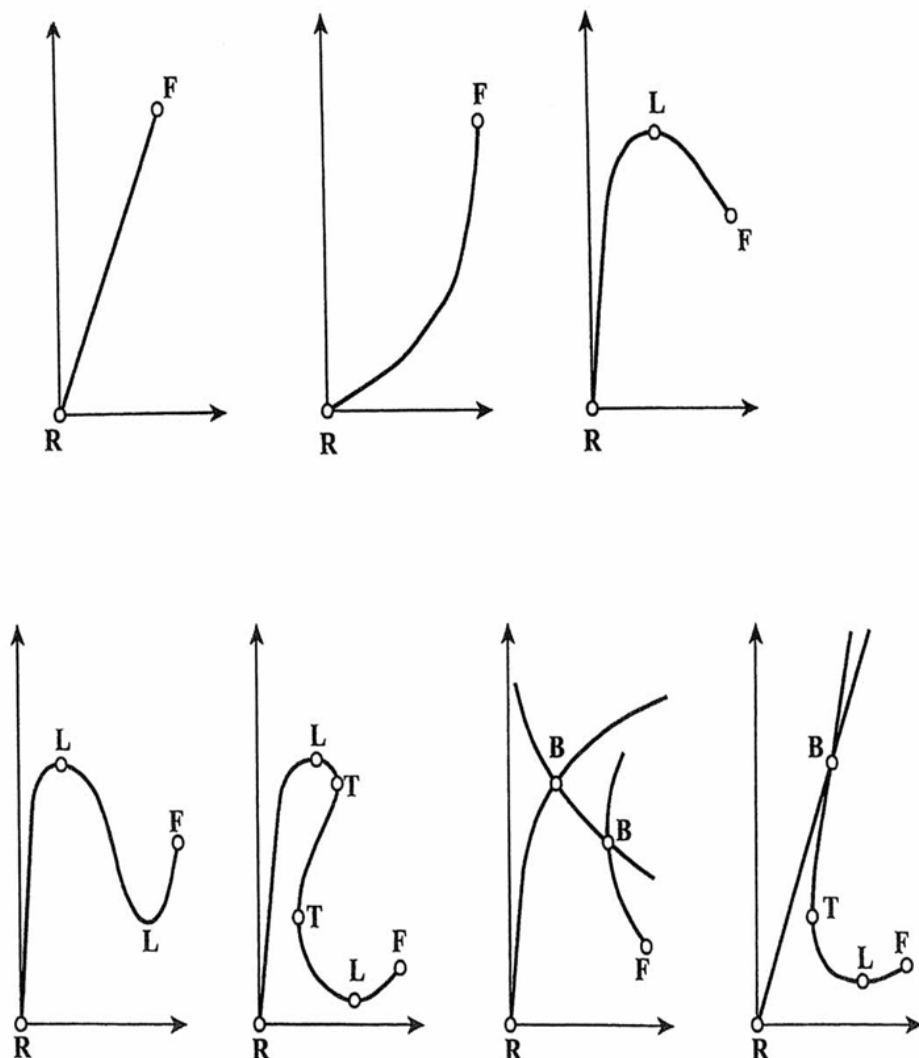


Figure 9.12: Illustration of different response characteristics

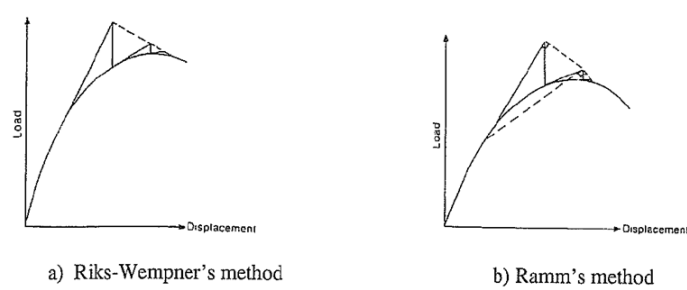


Figure 9.13: Illustration of Ramm's and Riks-Wempner's arc length methods

Non-linear Dynamic Analysis

In pipeline design both static and dynamic analysis need to be performed.

Nonlinear dynamic problems cannot be solved by modal superposition and therefore direct time integration of the equation of motion is necessary. This can be performed either by an explicit method or an implicit method.

$$\mathbf{r}_{k+1} = f(\ddot{\mathbf{r}}_k, \dot{\mathbf{r}}_k, \mathbf{r}_k, \mathbf{r}_{k-1}, \dots) \quad (9.53)$$

Explicit methods can typically be expressed as in Eq. 9.53. Here the displacement at the next time step will be determined based only on information from the current time step and previous steps. Explicit methods are conditionally stable and therefore very small time steps must be used. If these methods are formulated in terms of lumped mass and lumped damping matrices it is not necessary to solve a coupled equation system in the time march. This results in very small computational efforts per time step. In analysis of impulse type response it is necessary to use small time steps in order to achieve sufficient accuracy. Therefore explicit methods are typically used in explosion and impact analysis.

$$\mathbf{r}_{k+1} = f(\ddot{\mathbf{r}}_{k+1}, \ddot{\mathbf{r}}_k, \dot{\mathbf{r}}_{k+1}, \dot{\mathbf{r}}_k, \mathbf{r}_k, \dots) \quad (9.54)$$

As expressed in Eq. 9.54 the displacements in an implicit method depend on quantities at the next time step, together with information from the current step. Since implicit methods use information at the next time step they will have better numerical stability than explicit methods. The various implicit methods differ in connection with how the acceleration is assumed to vary between the time steps and at which time the equilibrium equation is fulfilled. By for instance assuming constant average acceleration between the time steps the result will be an unconditionally stable method. This means that numerical stability is provided regardless of the time step size. In case of long analysis durations it is beneficial to use such methods. When implicit methods are used it is necessary to solve a coupled equation system at every time step, and hence they will become uneconomical if short time steps are unavoidable due to accuracy. In case of nonlinear systems the guarantee of unconditional stability does not hold, but in practical cases this is not considered to be an issue [Langen and Sigbjørnson, 1979].

In a dynamic analysis the response of high frequency modes is of little interest and are described with less accuracy than the lower modes. Therefore it is desirable to remove these modes and at the same time describe the lower modes with good accuracy. It can be shown that increasing the damping ratio or introducing Rayleigh-damping in the well known Newmark- β method will damp out mainly the medium modes, leaving lower and higher modes almost unaffected [Mathisen, 1990]. Higher modes can however be damped out by numerical damping. In the Newmark- β method numerical damping can be introduced at the cost of reducing the accuracy from 2nd order to 1st order. The drawback of reduced accuracy can however be eliminated by applying the implicit HHT- α method proposed by Hilbert, Hughes and Taylor. The HHT- α method will damp out high frequency modes and at the same time retain 2nd order accuracy [Mathisen, 1990].

Equilibrium Iteration

The solution obtained in the incremental procedure proposed in Eq. 9.41 will in general not fulfill the equilibrium requirement as drift-off will take place. Therefore, equilibrium iterations according to Eq. 9.46 need to be carried out according to a preset criterion.

The equilibrium iterations can be formulated as a Newton-Raphson iteration scheme and when equilibrium is achieved, the right-hand side of Equation 9.46 will vanish. The iteration algorithm is terminated by means of a vector norm when equilibrium at a given tolerance level is achieved. Such a norm can for instance be based on total displacements as given below [Mathisen, 1990]:

$$\|\delta \mathbf{r}_{k+1}^{i+1}\| < \epsilon_D \|\mathbf{r}_{k+1}^{i+1}\| \quad (9.55)$$

$$\|\mathbf{r}_{k+1}^{i+1}\| = \frac{1}{N} \sqrt{\sum_{j=1}^N (r_j^{i+1})^2} \quad (9.56)$$

$$\|\delta \mathbf{r}_{k+1}^{i+1}\| = \|\mathbf{r}_{k+1}^{i+1}\| - \|\mathbf{r}_{k+1}^i\| \quad (9.57)$$

In the tolerance criteria given in Eq. 9.55 the accuracy of the solution is governed by the ϵ_D -parameter. Reasonable values for the ϵ_D -parameter is usually in the order of 10^{-2} to 10^{-6} [Mathisen, 1990].

Sensitivity studies of the tolerance parameters should always be carried out to ensure that the numerical algorithm produces result with sufficient accuracy.

9.5.5 Example non-linear static analysis algorithm

A schematic outline of the numerical procedure applied in a non-linear finite element program based on *CL* is given below where N_s is the number of time steps, N_e is the maximum number of allowed iterations, N_{de} is the number of degrees of freedom for each element, N_n is the number of nodes and N_d is the total number of degrees of freedom in the system.

1. LOAD STEP LOOP - $I = 1, N_s$ ($t = I \cdot \Delta t$)

(a) NEWTON RAPHSON ITERATION LOOP - $J = 1, N_i$

i. Build global tangential stiffness matrix \mathbf{K}_T and load increment $\Delta \mathbf{R}$

Element loop $i = 1, N_e$

A. Build element stiffness matrix \mathbf{k}_{Ti} , (dimension $N_{de} \times N_{de}$). In the plastic material case, this procedure includes numerical integration at discrete points along each element.

B. Calculate element load vector (dimension N_{de}) as $\Delta \mathbf{S}_i = \mathbf{S}_i^{ext}(t + \Delta t) - \mathbf{S}_i^{int}(t)$

C. Transform \mathbf{k}_{Ti} into global system by the operation $\mathbf{T}_i^T \mathbf{k}_{Ti} \mathbf{T}_i$. \mathbf{T}_i is a $(N_{de} \times N_{de})$ transformation matrix unique for each element i and expressed by the 3×3 transformation matrix that applies for each element end node. During deformation this matrix need to be updated based on the nodal transformation matrix \mathbf{T}_j^n (dimension $3 \times 3 \times N_n$).

D. Transform $\Delta\mathbf{S}_i$ into global system by the operation $\mathbf{T}_i^T \Delta\mathbf{S}_i$

E. Add \mathbf{k}_{Ti} into the global tangential stiffness matrix \mathbf{K}_T and $\Delta\mathbf{S}_i$ into $\Delta\mathbf{R}$

ii. **Solve the linear equation system $\mathbf{K}_T \Delta\mathbf{r} = \Delta\mathbf{R}$.**

iii. **Update nodal quantities**

A. Update displacements in all degrees of freedom (N_d)

B. Update coordinates of all nodal points (N_n)

C. Update the nodal point transformation matrix \mathbf{T}_j^n ($3 \times 3 \times N_n$)

iv. **Update element quantities**

Element loop $i = 1, N_e$

A. Update the element end displacements \mathbf{v}_i

B. Update the stress and strain state within the elements. In the case of non-linear material behaviour this involves numerical integration over a specified number of integration points.

C. Update the Element transformation matrices \mathbf{T}_i

v. Calculate convergence parameters according to Eq. 9.55

vi. Decide upon whether to iterate once more or go to the load step loop depending on the criteria specified by the user.

(b) **END ITERATION LOOP**

2. **END TIME INTEGRATION LOOP**

9.6 Description of important finite elements for pipeline structural analysis

9.6.1 Pipe Elements

For beams, the load is carried by longitudinal stresses only. Further, for long and slender structures, shear deformations can be neglected and the Bernoulli-Euler assumption apply. This means that the shear forces can no longer be obtained from the material law but need to be found by equilibrium considering the bending moment gradient along the element.

Further by assuming Navier's hypothesis that plane surfaces remain plane after deformation, the motion of an arbitrary point P in the cross shown in Figure 9.14 (a) can be described by displacement quantities for the centreline only (u_0, v_0, w_0 in combination with the torsion rotation θ_x). It is noted that if shear deformations were to be taken into account, additional unknowns related to the cross-section rotation θ_y and θ_z would be introduced. The displacements of the point P may now be expressed in terms of the local coordinates x, y, z in the cross section as:

$$\begin{aligned} u_x(x, y, z) &= u_{x_0} - yu_{y_0,x} - zu_{z_0,x} \\ u_y(x, y, z) &= u_{y_0} - z\theta_x \\ u_z(x, y, z) &= u_{z_0} - y\theta_x \end{aligned} \quad (9.58)$$

Using Eq. 9.16, and introducing indices $x - y - z$ in stead of $1 - 2 - 3$, the longitudinal Green strain can be expressed as:

$$\begin{aligned} E_{xx} &= \frac{1}{2}(u_{x,x} + u_{x,x} + u_{k,x}u_{k,x}) \\ &= u_{x,x} + \frac{1}{2}u_{x,x}^2 + \frac{1}{2}u_{y,x}^2 + \frac{1}{2}u_{z,x}^2 \\ &\simeq u_{x_0,x} - yu_{y_0,xx} - zu_{z_0,xx} + \frac{1}{2}(u_{y_0,x}^2 + u_{z_0,x}^2) + \theta_{,x}(yu_{z_0,x} - zu_{y_0,x}) + \frac{1}{2}\theta_{,x}^2(y^2 + z^2) \end{aligned} \quad (9.59)$$

The above includes the terms related to coupling between longitudinal strain and torsion whereas the terms related to $\frac{1}{2}u_{x,x}^2$ are neglected to avoid numerical problems related to self-straining. Both terms are usually small, however, in order to be able to accurately predict torsion buckling due to residual plastic strains in the stinger during installation, the torsion coupling terms should be included.

The total and incremental equilibrium equations are then obtained by applying Eq. 9.26 and Eq. 9.28 in combination with the material laws, either elastic (Eq. 9.29) or plastic (Eq. 9.37), and the appropriate displacement interpolation functions. Linear interpolation is normally used in the axial direction, whereas cubic interpolation is used in the transverse direction. This means that the axial strain is constant whereas the curvature terms are

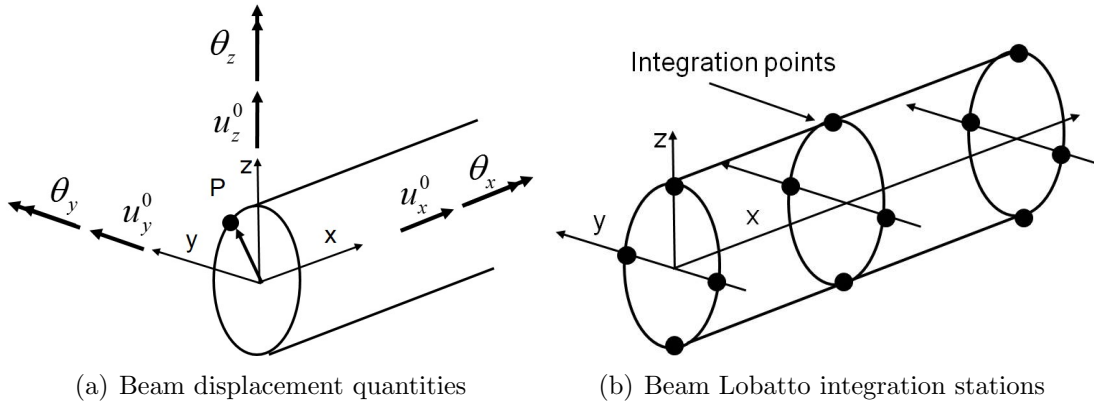


Figure 9.14: 3D beam non-linear element

linear. For the plastic material case, the stiffness matrix and equilibrium forces need to be evaluated by numerical integration and the material model need to include memory parameters at each point to capture the hysteresis effect. These need to be stored in each integration point and the integration need to be carried out both over the cross-section and along the pipe element. This is visualised in Figure 9.14(b) where 3-point Lobatto integration (3 stations along element) with 4 integration points over the cross-section has been assumed. 3 point Lobatto integrates exactly polynomials of order $2n - 2 = 4$ where n is the number of integration stations along the element. Alternatively, 3 point Gauss integration integrates exactly polynomials of order $2n - 1 = 5$. However, one advantage of Lobatto integration is that the integration stations include the element ends. Further, by noting that the stiffness matrix is calculated based on Eq. 9.28, the highest order terms will be quadratic (curvature*curvature) and 3 point Lobatto is hence sufficient in this case.

The effect of internal and external pressure is included by means of the relevant terms in Eq. 9.26 and the Poisson's effect resulting from the applied material law. For elastic behaviour the Poisson's ratio of steels is in the range of 0.3. During plastic deformation, however, this increases to 0.5 and the material then basically behave incompressible as water.

It is noted that in order to predict strains in the plastic domain, the representation of correct bending moment at each cross-section become important. This requires a minimum number of integration points over the cross-section, normally at least 16. Convergence studies should be carried out to ensure convergence in terms of strain level. It is noted that numerical integration is time consuming with a factor of at least 10 compared to elastic analysis.

9.6.2 Seabed contact element

The seabed contact element is used to describe contact between the pipe and the seabed. The seabed is considered as a contact surface and the pipe is considered as a cylinder with

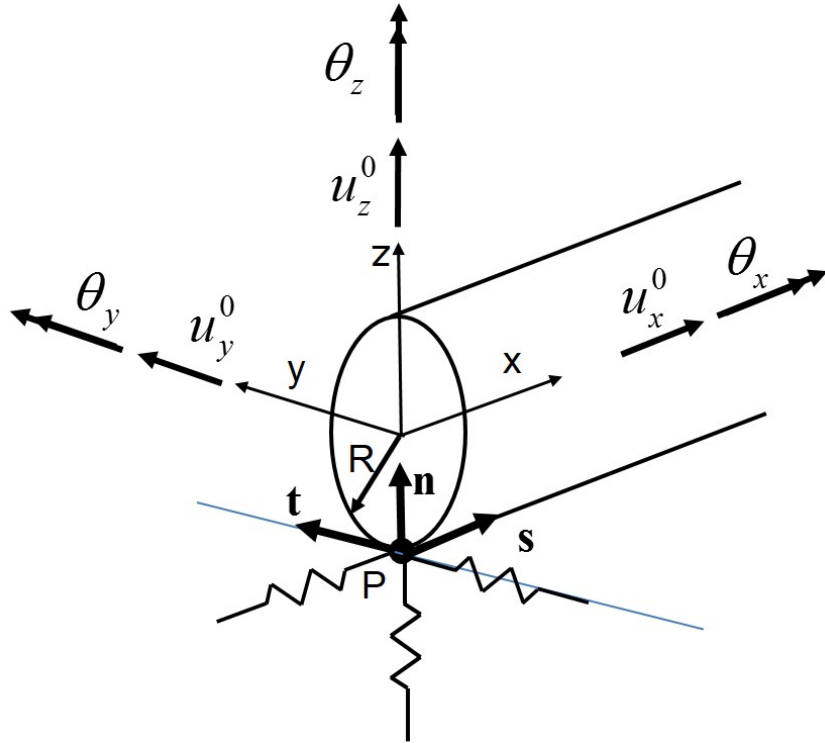


Figure 9.15: The 3D seabed contact element

radius R . Whenever, contact is obtained, a spring is introduced at the pipe node. The seabed contact element therefore includes 1 node with 6 DOFs. Further, as long as the two bodies remain in contact, relative displacements with associated friction forces may also occur. Reference is given to Figure 9.15, where all vectors are measured in the elemental j -system.

The normal vector \mathbf{n} at the contact point is established from the seabed surface, the tangential direction \mathbf{s} is calculated from the pipe tangential direction whereas \mathbf{t} is calculated from the cross-product between these two.

After a time increment Δt , two contact conditions may occur:

1. Gap opening:

$$g = \Delta\mathbf{u} \cdot \mathbf{n} + g_0 = \Delta u_{z0} + g_0 \geq 0 \quad (9.60)$$

2. Contact:

$$g = \Delta\mathbf{u} \cdot \mathbf{n} + g_0 = \Delta u_{z0} + g_0 < 0 \quad (9.61)$$

g is the current gap at time $t + \Delta t$ in the direction of \mathbf{n} . Further, if contact has been established, relative slippage including friction work will occur when:

$$\Delta\gamma_t = \Delta\mathbf{u} \cdot \mathbf{t} = \Delta u_{y0} + R\Delta\theta_x \neq 0 \quad (9.62)$$

$$\Delta\gamma_s = \Delta\mathbf{u} \cdot \mathbf{s} \approx \Delta u_{x0} \neq 0 \quad (9.63)$$

where \mathbf{s} and \mathbf{t} are the tangent vectors obtained according to the above procedure. The rotation coupling term in the transverse direction is included to allow modelling friction due to possible rotation motion of the pipe. Such behaviour may result during pipe installation due to torsion buckling resulting from residual strains induced by the stinger during S-lay.

Whenever contact occurs, spring stiffness and forces are introduced to represent the soil reaction forces. In the vertical direction, a non-linear elastic characteristic is often applied, whereas in the tangential friction a combination of non-linear elastic and elastic-plastic material models can be applied to respectively model the geometric effect from soil penetration and friction. This is visualized in Figure 9.16. Alternatively more advanced material models may be implemented in the spring characteristics depending on the soil conditions. For clay conditions where Coulomb friction does not apply several alternative models have been proposed, depending on application, see e.g. [Sotberg et al., 1994], [Carr et al., 2006], [DNVGL, 2010a] and [Aubeny et al., 2006]

9.6.3 Roller contact element

The roller contact element may be used to describe contact between the pipe elements and the roller boxes on the stinger during e.g. S-lay installation. Contact is considered assuming the roller and pipe represented as two cylinders, A and B each governed by its radius R_A and R_B . The contact can occur at an arbitrary point between the pipe element nodes. This means that the contact element has to include 3-nodes (18 DOFs).

Whenever, contact occurs, a spring is introduced at the contact point. Further, as long as the two bodies remain in contact, relative displacements with associated friction forces will be introduced. Reference is given to Figure 9.17, where all vectors are measured in the elemental \mathbf{j} -system.

The normal vector \mathbf{n} at the contact point is established by:

$$\mathbf{n} = \frac{d\mathbf{r}^B \times d\mathbf{r}^A}{|d\mathbf{r}^B \times d\mathbf{r}^A|} \quad (9.64)$$

where $d\mathbf{r}^l = \mathbf{r}^{l2} - \mathbf{r}^{l1}$, $l = A, B$ i.e. based on the end coordinates. In order to keep track of the direction of contact the normal vector \mathbf{n} needs to be scaled by the parameter m defined by:

$$m = (\mathbf{r}^{B1} - \mathbf{r}^{A1}) \cdot \mathbf{n} \quad (9.65)$$

The other vectors defining the contact surface can now be calculated by:

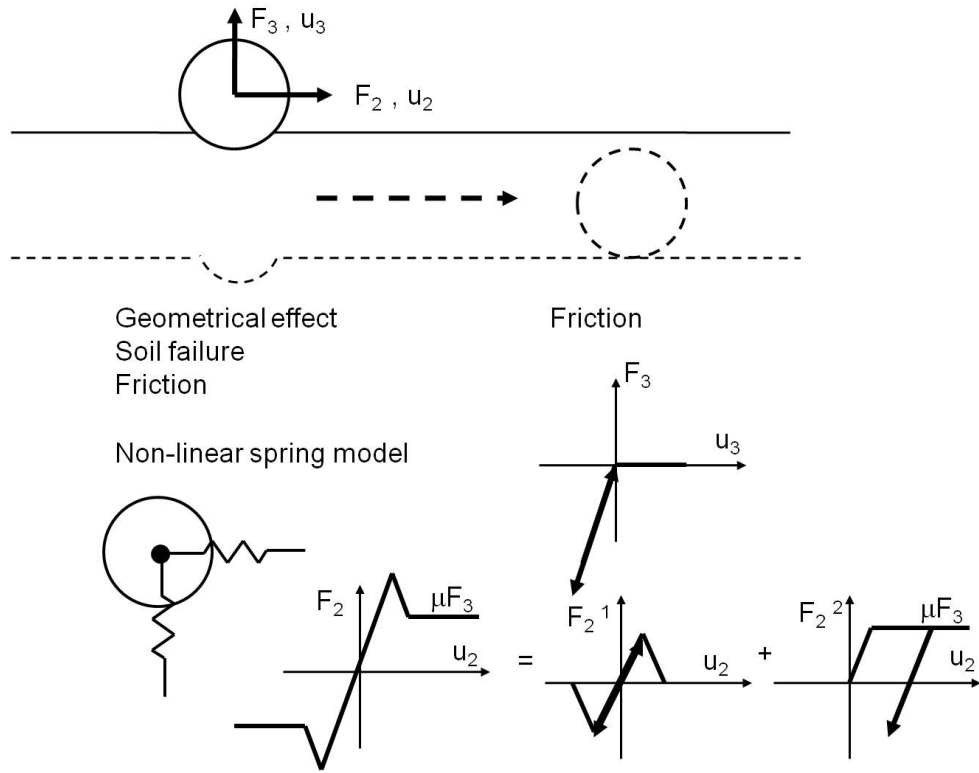


Figure 9.16: Pipe-seabed contact model

$$\mathbf{s} = \frac{d\mathbf{r}^B}{|d\mathbf{r}^B|} \quad (9.66)$$

and

$$\mathbf{t} = \mathbf{n} \times \mathbf{s} \quad (9.67)$$

The gap at the start of the increment can now be expressed by:

$$g_0 = (\mathbf{r}^{B1} - \mathbf{r}^{A1}) \cdot \mathbf{n} - R^A - R^B \quad (9.68)$$

where \mathbf{r}^{l1} , $l = A$ or B , represents the updated coordinate positions of the roller and pipe first end point. R^A and R^B is the roller and pipe radii, respectively. The non-dimensional parameters in Figure 9.17 ξ and η can further be defined by:

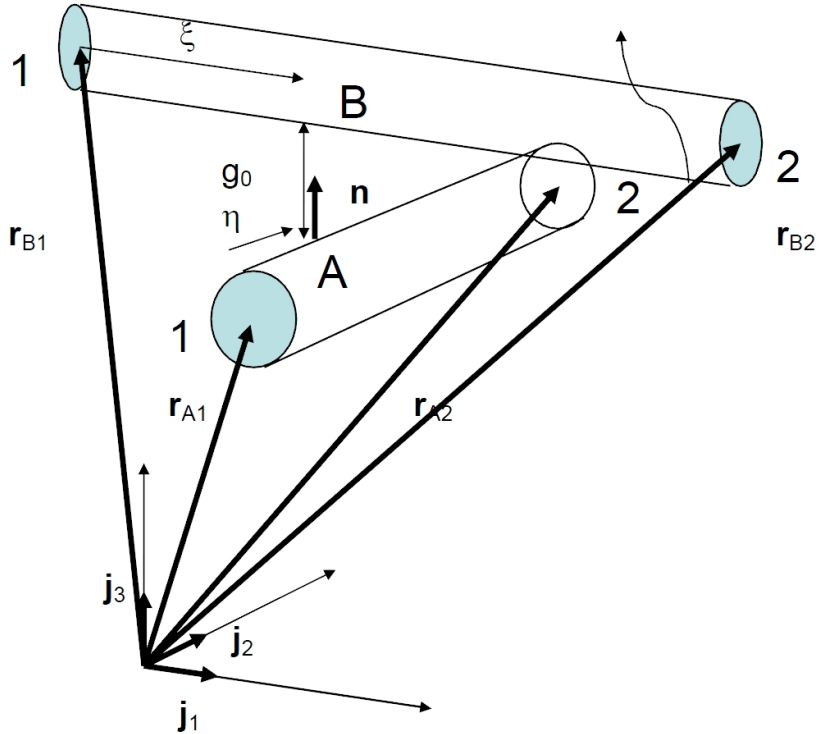


Figure 9.17: Geometrical relations for roller contact element

$$\cos \varphi = \frac{d\mathbf{r}^A \cdot d\mathbf{r}^B}{|d\mathbf{r}^A| |d\mathbf{r}^B|} \quad (9.69)$$

$$\sin \varphi = \sqrt{1 - \cos^2 \varphi}$$

$$\xi = \frac{m (d\mathbf{r}^A \times \mathbf{n}) \cdot (\mathbf{r}^{B1} - \mathbf{r}^{A1})}{\sin \varphi |d\mathbf{r}^A \times \mathbf{n}| |d\mathbf{r}^B|}$$

$$\eta = \frac{m (d\mathbf{r}^B \times \mathbf{n}) \cdot (\mathbf{r}^{B1} - \mathbf{r}^{A1})}{\sin \varphi |d\mathbf{r}^B \times \mathbf{n}| |d\mathbf{r}^A|}$$

and by assuming linear interpolation, i.e. assumming a linear interpolation of the contact force between the end nodes of the slave body, the relative motion between the two bodies at the contact point can be expressed in terms of the end displacements as:

$$\mathbf{u}_B - \mathbf{u}_A = \mathbf{u}_{B1}(1 - \xi) + \mathbf{u}_{B2}\xi - \mathbf{u}_{A1}(1 - \eta) - \mathbf{u}_{A2}\eta \quad (9.70)$$

After a time increment Δt , two contact conditions may occur:

1. Gap opening:

$$g = (\Delta \mathbf{u}_B - \Delta \mathbf{u}_A) \cdot \mathbf{n} + g_0 \geq 0 \quad (9.71)$$

2. Contact:

$$g = (\Delta \mathbf{u}_B - \Delta \mathbf{u}_A) \cdot \mathbf{n} + g_0 < 0 \quad (9.72)$$

g is the current gap at time $t + \Delta t$ in the direction of \mathbf{n} . Further, if contact has been established, relative slippage including friction work will occur when:

$$\Delta \gamma_t = (\Delta \mathbf{u}_B - \Delta \mathbf{u}_A) \cdot \mathbf{t} \neq 0 \quad (9.73)$$

$$\Delta \gamma_s = (\Delta \mathbf{u}_B - \Delta \mathbf{u}_A) \cdot \mathbf{s} \neq 0 \quad (9.74)$$

where \mathbf{s} and \mathbf{t} are the tangent vectors pointing towards body B .

Whenever contact occurs, a spring characteristic is introduced in a similar way as for the seabed contact element.

9.6.4 3 Noded Pipe-In-Pipe Contact Element

The contact between two cylinders A and B is studied, the cylinder A (body A) being located on the inside of cylinder B (body B), see Figure 9.18, where four different coordinate systems are defined:

- The global system with axes X_i and base vectors \mathbf{I}_i
- The master element system positioned at the centre of body A with axes x_i and base vectors \mathbf{i}_i
- The slave element system with origo at element node B1 of slave body B with coordinate axes y_i and base vectors \mathbf{j}_i .
- The contact point system positioned at point C on the outer circumference of the master body A with coordinate axes s_i and base vectors \mathbf{n}_i . The outward normal \mathbf{n}_3 is taken to be directed outward from the master body centre.

The position vector of the conical slave body B relative to body A is defined by the position vectors \mathbf{r}_{B1} of the slave end node B1 and \mathbf{r}_A of the master node at body A. Using matrix notation, the local base vector \mathbf{i}_- and \mathbf{j}_- systems are both defined with reference to the global system and are linked to each other by the following transformations:

$$\begin{aligned} \mathbf{j}_i &= T_{ij}^y \mathbf{I}_j & (9.75) \\ \mathbf{i}_i &= T_{ij}^x \mathbf{I}_j = T_{ij}^x T_{jk}^{yT} \mathbf{j}_k \end{aligned}$$

where T_{ij}^x and T_{ij}^y are the transformation matrices respectively between the local x_i and y_i coordinate systems and the global X_i axis system. The position vector of the contact

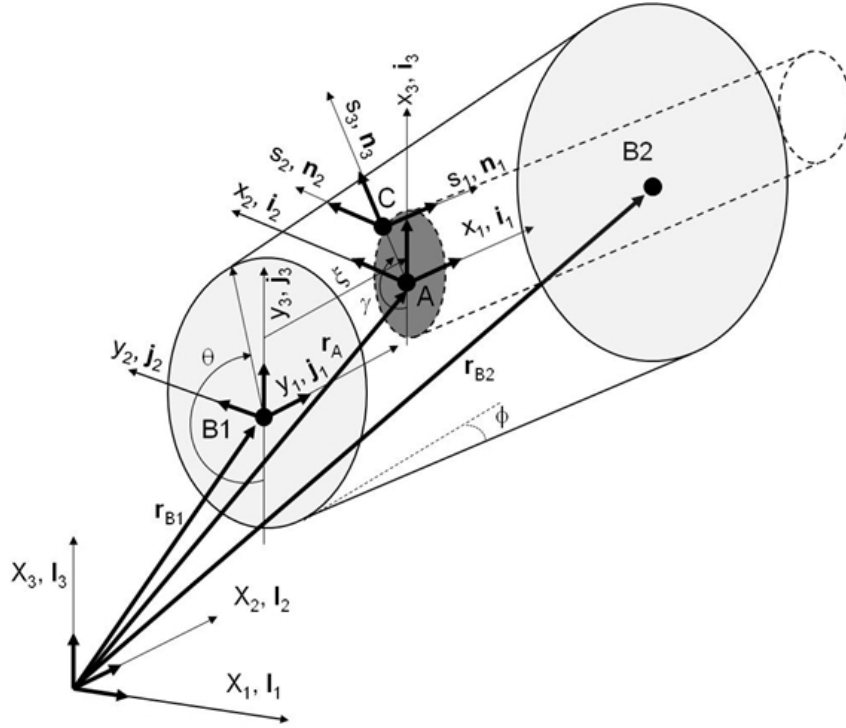


Figure 9.18: Contact element coordinate systems

point on the surface of the master cylinder surface with radius R_A and angular orientation γ can be expressed as:

$$\mathbf{r}_{CA} = \mathbf{r}_A + R_A \sin \gamma \mathbf{i}_2 - R_A \cos \gamma \mathbf{i}_3 \quad (9.76)$$

which in the slave body system can be expressed by:

$$\mathbf{r}_{CB} = \mathbf{r}_{Ba} + [R_{B1}(1 - \xi) + R_{B2}(\xi)] [\sin \theta \mathbf{j}_2 - \cos \theta \mathbf{j}_3] \quad (9.77)$$

where ξ is the dimensionless length coordinate along the slave element, R_{Bi} is the radius at element end i and θ is the angular orientation expressed in the slave system. By defining the relative vector \mathbf{a} in the slave system as:

$$\mathbf{a} = \mathbf{r}_{CA} - \mathbf{r}_{B1} = a_i \mathbf{I}_i = a_i T_{ij}^{yT} \mathbf{j}_j \quad (9.78)$$

The longitudinal position of the contact point C relative to end 1 of body B is found by:

$$\xi = \mathbf{a} \cdot \mathbf{j}_1 \cdot \frac{1}{L} \quad (9.79)$$

where L is the element length between nodes of slave body B. Contact is obtained when the gap g fulfills the following condition:

$$g = (\mathbf{r}_{CB} - \mathbf{r}_{CA}) \cdot \mathbf{n}_3 < 0 \quad (9.80)$$

The angular position of the contact point relative to the slave system is defined by:

$$\cos \theta = \frac{\mathbf{a}}{|\mathbf{a}|} \cdot -\mathbf{j}_3 \quad (9.81)$$

$$\sin \theta = \frac{\mathbf{a}}{|\mathbf{a}|} \cdot \mathbf{j}_2 \quad (9.82)$$

The radial normal vector at a given circular section along the slave element is given by:

$$\mathbf{n}_3^B = \sin \theta \mathbf{j}_2 - \cos \theta \mathbf{j}_3 \quad (9.83)$$

The orientation of the local contact point system is then established by the following procedure:

$$\mathbf{n}_1 = \mathbf{i}_1 \quad (9.84)$$

$$\mathbf{n}_2 = \frac{\mathbf{n}_3^B \times \mathbf{i}_1}{|\mathbf{n}_3^B \times \mathbf{i}_1|}$$

$$\mathbf{n}_3 = \frac{\mathbf{i}_1 \times \mathbf{n}_2}{|\mathbf{i}_1 \times \mathbf{n}_2|}$$

It is noted that since the angle γ is not known a priori an iterative procedure is needed to find the actual contact point.

Considering an increment in displacement $\Delta \mathbf{u}$ defined in the time interval $[t, t + \Delta t]$, two conditions may occur:

1. Gap opening:

$$g = (\Delta \mathbf{u}_{CB} - \Delta \mathbf{u}_{CA}) \cdot \mathbf{n}_3 + g_0 \geq 0 \quad (9.85)$$

2. Contact:

$$g = (\Delta \mathbf{u}_{CB} - \Delta \mathbf{u}_{CA}) \cdot \mathbf{n}_3 + g_0 < 0 \quad (9.86)$$

g is the current gap at time $t + \Delta t$ in the direction of \mathbf{n}_3 whereas g_0 is the gap at time t . Further, if contact has been established, increments in relative slippage will occur:

$$\Delta \gamma_1 = (\Delta \mathbf{u}_{CB} - \Delta \mathbf{u}_A) \cdot \mathbf{n}_1 \neq 0 \quad (9.87)$$

$$\Delta \gamma_2 = (\Delta \mathbf{u}_{CB} - \Delta \mathbf{u}_{CA}) \cdot \mathbf{n}_2 \neq 0 \quad (9.88)$$

where \mathbf{n}_1 and \mathbf{n}_2 are the tangent vectors defined above.

Whenever contact occurs, a spring characteristic is introduced in a similar way as for the seabed contact element.

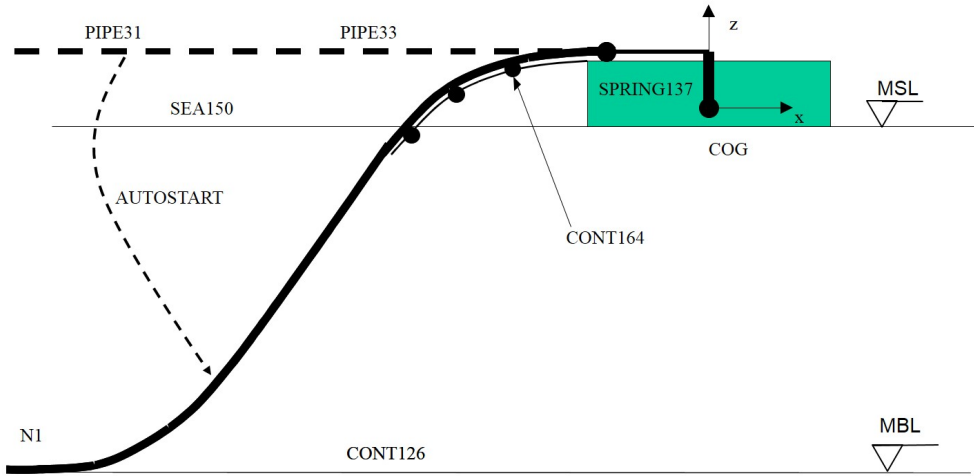


Figure 9.19: S-lay model.

9.7 The Pipeline Installation Case

9.7.1 General

In the following the pipeline installation case will be used to demonstrate which finite elements that typically need to be used for structural analysis of pipelines using the computer program SIMLA.

The analysis is carried out as an in-place irregular dynamic analysis to investigate the dynamic response of the pipeline exposed to:

- $H_s=4$ m, $T_p = 10$ s
- Current velocity 0-1m/s
- OD=1084 mm, $t = 34.1$ mm
- Water depth 250 m

This case has been selected because it is fairly complex and basically includes all elements needed to perform most engineering calculations relevant for pipelines.

9.7.2 Modelling

The model is shown in Figure 9.19.

The pipe model includes altogether 440 pipe elements ID 1-440, 340 PIPE31 linear pipe elements and 100 PIPE33 elastoplastic pipe elements. The PIPE33 elements have been introduced to allow modelling plastic strains over the stinger.

The stinger is modelled by CONT124 roller elements where the master node for all elements is the vessel COG node ID number 3001. Element eccentricity is introduced in

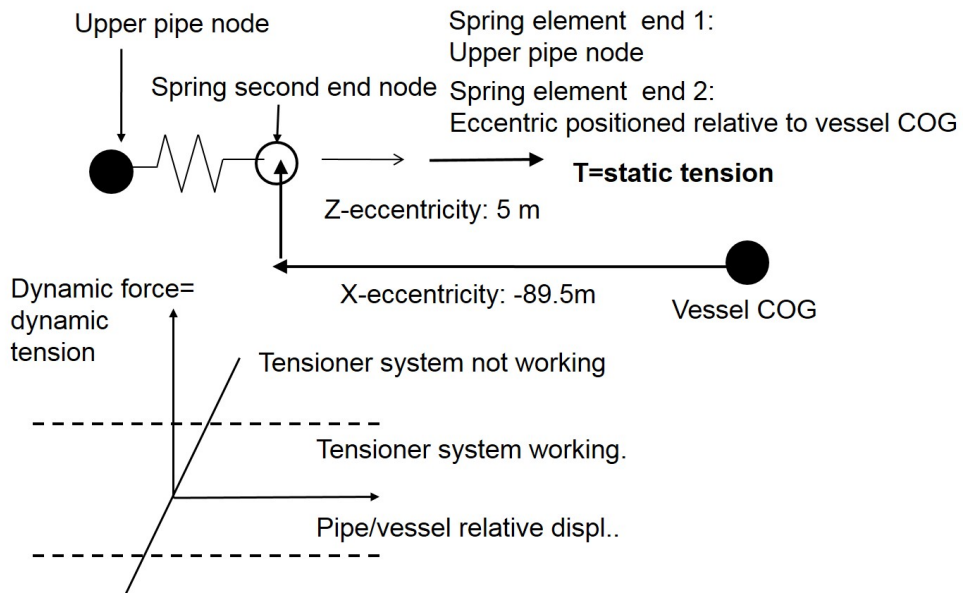


Figure 9.20: Tensioner model

these elements in order to position the roller box relative to node ID 3001. There are 16 roller elements, positioned with 10-8 m spacing. The stinger radius is 120 m and the first roller starts at angle 10 degrees. There are two vertical rollers at the last and first roller boxes to avoid transverse displacement. In order to connect the pipe end node ID 441 to the vessel and to allow tensioner modelling, one SPRING137 element is introduced, end 1 at node ID 3001 which is at the vessel COG and end 2 at pipe node ID 441. Eccentricity is introduced in the local element x-direction and at end 1 of spring element ID 3000 to ensure that the element end is positioned at the same point as node 441. The tensioner is a hydraulic machine for keeping the tension in the pipeline. It is usually designed to work at a static mean level with a *deadband* to damp out dynamic loading. Therefore, the tensioner is represented by as a mean static load and a spring with a non-linear material curve to represent the deadband, see Figure 9.20. In order to check the effect of having a not working tensioner, sensitivity analyses assuming the pipe to be fixed to the vessel were included.

There are also 200 CONT126 seabed contact elements which are connected to pipe node IDs 1-201 and 100 SEA150 elements, in order to introduce buoyancy and hydrodynamic loading for the structural elements. One SEA element is sufficient for the numeric model. For visual presentation of the wave, however, 100 elements have been selected. The CONT126 element requires that the seabed geometry is imported from a text file storing seabed geometry information.

The static analysis is done in one load step using the AUTOSTART feature that enables initiation of both J-lay and S-lay, time = 0 – 1.0s, where the gravity loading is applied in one step to the full value.

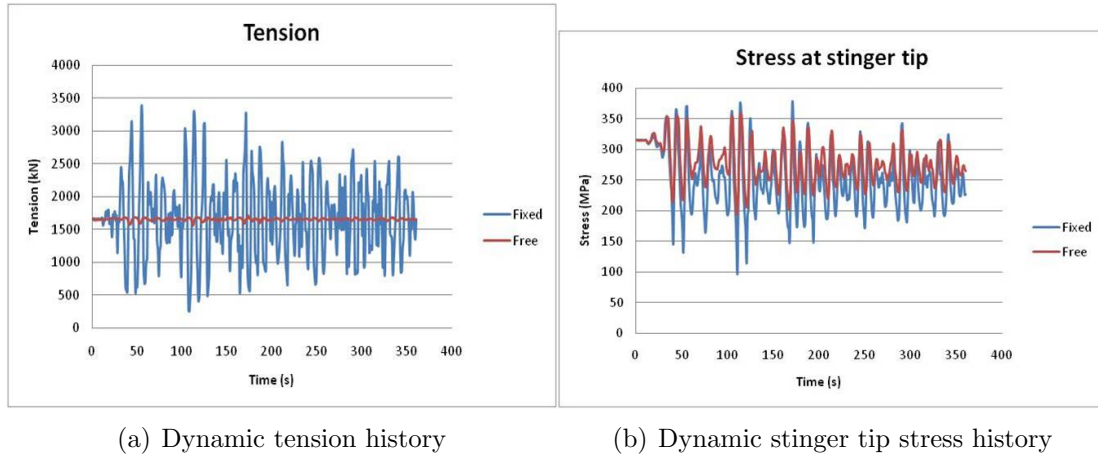


Figure 9.21: History plots - tension and stress

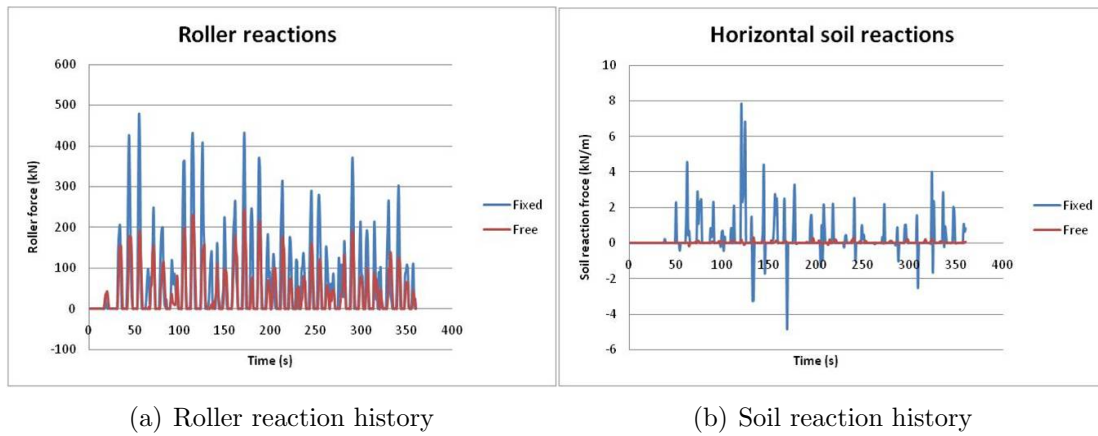


Figure 9.22: Reaction histories

The dynamic analysis is then defined from $1.1s - 120s$ with a time step length of $0.1s$.

9.7.3 Example of results

Example results are shown in Figure 9.21-Figure 9.22. The effect of keeping the pipe fixed dramatically increases the dynamic response as expected.

Chapter 10

References

Bibliography

- [API, 2008a] API (2008a). Recommended practice for flexible pipe. API, USA, 4 edition.
- [API, 2008b] API (2008b). Specification for unbonded flexible pipe. API, USA, 3 edition.
- [Argyris, 1982] Argyris, J. (1982). An excursion into large rotations. *Computer Methods in Applied Mechanics and Engineering*, 32:85–155.
- [Aubeny et al., 2006] Aubeny, C., Biscontin, G., and Zhang, J. (2006). Seafloor interaction with steel catenary risers. Technical report, A M University, Austin, Texas.
- [Bai and Bai, 2005] Bai, Y. and Bai, Q. (2005). *Subsea pipelines and risers*. Elsevier, Oxford, UK.
- [Bai et al., 1997] Bai, Y., Igland, R. T., and Moan, T. (1997). Tube collapse under combined external pressure, tension and bending. *Marine Structures*, 10(5):389 – 410.
- [Bathe, 1982] Bathe, K. (1982). *Finite Element Procedures in Engineering Analysis*. Prentince-Hall Ind.
- [Bectarte and Coutarel, 2004] Bectarte, F. and Coutarel, A. (2004). Instability of tensile armour layers of flexible pipes. In *Proc. of OMAE'2004*.
- [Belytschko et al., 2001] Belytschko, T., Liu, W., and Moran, B. (2001). *Nonlinear Finite Elements for Continua and Structures*. John Wiley & Sons.
- [Berg et al., 2009] Berg, E., Holthe, K. H., and Skallerud, B. (2009). Cyclic plasticity modelling for andes thin shell and line-spring finite elements. *J. of Applied Mechanics*, 1(1):201–232.
- [Bergan, 1971] Bergan, P. (1971). *Nonlinear Analysis of Plates Considering Geometric and Material Effects, Ph.D Dissertation*. PhD thesis, Norwegian University of Science and Technology, Trondheim, Norway.
- [Borisenko and Tarapov, 1968] Borisenko, A. and Tarapov, I. (1968). *Vector and Tensor Analysis with Applications*. Prentice-Hall, Inc.

- [Brack et al., 2005] Brack, A., Troina, L., and Sousa, J. (2005). Flexible riser resistance against combined axial compression, bending and torsion in ultra-deep water depths. In *Proc. of OMAE'2005*.
- [Carr et al., 2006] Carr, M., Sinclair, F., and Bruton, D. (2006). Pipeline walking - understanding the field layout challenges and analytical solutions developed for the safebuck jip. In *OTC, Houston, Texas*.
- [Cary, 1979] Cary, H. (1979). *Modern welding technology*. Prentice-Hall.
- [Chaudhury, 2010] Chaudhury, G. (2010). Managing unidirectional movements (walk) of hpht submarine flowlines during startup heating and shutdown cooling. In *Proc. of ISOPE-2010, Paper. no. IOPF2010-1003, Houston, Texas*.
- [Chen et al., 1992] Chen, B., Nielsen, R., and Colquhoun, R. (1992). Theoretical models for prediction of burst and collapse and their verification by testing. In *Flexible pipe technology, Int. seminar on Research and Development 18-20 February, NTH*.
- [Christensen and Baker, 1982] Christensen, P. T. and Baker, M. (1982). *Structural reliability and its application*. Springer-Verlag.
- [D.Brunton et al., 2008] D.Brunton, D.White, Carr, M., and Cheuk, C. (2008). Pipe-soil interaction during lateral buckling and pipeline walking. In *OTC, Houston, Texas*.
- [D.Brunton et al., 2006] D.Brunton, D.White, Cheuk, C., Bolton, M., and Carr, M. (2006). Pipe/soil interaction behaviour during lateral buckling. *SPE journal of projects, Facilities and Construction*, 1(3):1–9.
- [de Sousa et al., 2012] de Sousa, J., Viero, P., Magluta, C., and Roitman, N. (2012). An experimental and numerical study on the axial compression of flexible pipes. *jomae*, 134.
- [DNV, 1982] DNV (1982). Rules for submarine pipeline systems. DNV, Høvik, Norway.
- [DNVGL, 2006a] DNVGL (2006a). Recommended practice dnv-rp-f105: Free-spanning pipelines. DNVGL, Høvik, Norway.
- [DNVGL, 2006b] DNVGL (2006b). Recommended practice dnv-rp-f108: Fracture control for pipeline installation methods introducing cyclic plastic strain. DNVGL, Høvik, Norway.
- [DNVGL, 2007] DNVGL (2007). Recommended practice dnv-rp-f110: Global buckling of submarine pipelines. DNVGL, Høvik, Norway.
- [DNVGL, 2010a] DNVGL (2010a). Recommended practice dnv-rp-f109: On-bottom stability design of offshore pipelines. DNVGL, Høvik, Norway.
- [DNVGL, 2010b] DNVGL (2010b). Recommended practice dnv-rp-f204: Riser fatigue. DNVGL, Høvik, Norway.

- [DNVGL, 2012] DNVGL (2012). Offshore standard dnv-os-f101: Submarine pipeline systems. DNVGL, Høvik, Norway.
- [Faltinsen, 1990] Faltinsen, O. M. (1990). *Sea Loads on Ships and Offshore Structures*. Cambridge University Press, Cambridge CB2 2RU, UK.
- [Feret et al., 1986] Feret, J., Bournazel, C., and Rigaud, J. (1986). Evaluation of flexible pipes' life expectancy under dynamic conditions. In *OTC5230, Houston, USA*. OTC.
- [Fergestad and Løtveit, 2014] Fergestad, D. and Løtveit, S. (2014). New handbook on design and operation of flexible pipes. Technical report, Marintek.
- [Fylling et al., 1995] Fylling, I., Larsen, C., Sødahl, N., Ormberg, H., Engseth, A., Passano, E., and Holthe, H. (1995). Riflex - theory manual. Technical Report STF70-F95219, SINTEF Structural Engineering.
- [Gijjt, 1990] Gijjt, J. (1990). Upheaval buckling of offshore pipelines: Overview and introduction. In *Proc. of Offshore Technology, OTC 6487, Houston, Texas*.
- [Hibbit et al., 1970] Hibbit, H., Marcal, P., and Rice, J. (1970). A finite element formulation for problems of large strain and large displacements. *Int. J. of Solids and Structures*, 6:1069–1086.
- [ISO, 4063] ISO (4063). Welding methods. 4063.
- [Jakobsen, 1994] Jakobsen, B. (1994). The sleipner accident and its causes. *Engineering Failure Analysis*, 1(3):193–199.
- [Jiao and Kyriakides, 2009] Jiao, R. and Kyriakides, S. (2009). Ratcheting, wrinkling and collapse of tubes under axial cycling. *International Journal of Solids and Structures*, 46(1415):2856 – 2870.
- [Klæbo et al., 2008] Klæbo, F., Giertsen, E., and Sævik, S. (2008). Efficient analysis of offshore pipeline buckling on uneven seabeds. In *Proc. of OMAE'2008, ISBN: 0-7918-3821-8, Estoril, Portugal*.
- [Langen and Sigbjørnsen, 1979] Langen, I. and Sigbjørnsen, R. (1979). *Dynamisk Analyse av Konstruksjoner*. Tapir, Trondheim, Norway. In Norwegian.
- [Larsen et al., 2014] Larsen, C., Sævik, S., and Qvist, J. (2014). Design analysis. i: Handbook on design and operation of flexible pipes. In *Trondheim*, pages 155–276. Norsk Marinteknisk Forskningsinstitutt AS.
- [Levold, 1990] Levold, E. (1990). *Solid Mechanics and Material Models including Large Deformations*. PhD thesis, NTH, Trondheim, Norway.

- [M. Carr and Bruton, 2006] M. Carr, F. S. and Bruton, D. (2006). Pipeline walking - understanding the field layout challenges, and analytical solutions, developed for the safebuck jip. In *Proc. of the 2006 Offshore Technology Conference, Paper. no. OTC17945, Houston, Texas.* OTC.
- [Madsen et al., 1986] Madsen, H., Krenk, S., and Lind, N. (1986). *Methods of Structural Safety*. Prentice-Hall International, Inc., New Jersey.
- [MARINTEK, 2009a] MARINTEK (2009a). Course in the simla program system.
- [MARINTEK, 2009b] MARINTEK (2009b). Course in the uflex program system.
- [Mathisen, 1990] Mathisen, K. (1990). *Large Displacement Analysis of Flexible and Rigid Systems Considering Displacement-Dependent Loads and Non-Linear Constraints*. PhD thesis, Norwegian Institute of Technology, Trondheim, Norway.
- [Mattiason, 1983] Mattiason, K. (1983). On the co-rotational finite element formulation for large deformation problems. Technical Report Publication 83:1, Department of Structural Mechanics, Chalmers University of Technology, Gothenburg, Sweden.
- [McMeeking et al., 1975] McMeeking, R., Marcal, P., and Rice, J. (1975). Finite element formulations for problems of large elastic-plastic deformation. *Int. J. of Solids and Structures*, 11:601–661.
- [Melcher, 1987] Melcher, R. (1987). *Structural reliability. Analysis and prediction*. Ellis Horwood, Ltd.
- [Morison et al., 1950] Morison, J., O'Brien, M., Johnson, J.-E., and Shaaf, S. (1950). The force exerted by surface waves on piles. In *Petroleum Transactions, AIME 189*, pages 149–154.
- [Naess et al., 2009] Naess, A., Leira, B., and Batsevych, O. (2009). System reliability analysis by enhanced monte carlo simulation. *Structural Safety*, 31(5):349 – 355.
- [Naess and Moan, 2013] Naess, A. and Moan, T. (2013). *Stochastic Dynamics of Marine Structures*. Cambridge University Press.
- [Nes et al., 1996] Nes, H., Sævik, S., Levold, E., and Johannessen, A. (1996). Expansion control of large diameter pipelines. In *Proc. of OMAE'96, ISBN: 0-7918-1491-2, Firenze, Italy*.
- [Nielsen et al., 1990a] Nielsen, N. J. R., Pedersen, P. T., Grundy, A. K., and Lyngberg, B. S. (1990a). Design criteria for upheaval creep of buried sub-sea pipelines. *jomae*, 112(4):290–296.
- [Nielsen et al., 1990b] Nielsen, R., Colquhoun, R., and McCone, A. (1990b). Tools for predicting service life of dynamic flexible pipes. In *Proc. of European Offshore Mechanics Symposium, NTH, Trondheim*.

- [NORSOK STANDARD, M001] NORSKO STANDARD (M001). Material selection. M-001.
- [NORSOK STANDARD, M506] NORSKO STANDARD (M506). CO₂ corrosion model. M-506.
- [Nysveen et al., 2005] Nysveen, A., Kulbotten, H., and A.H. Børnes, J. L., and Høer-Hansen, M. (2005). Direct electrical heating of subsea pipelines - technology development an operating experience. In *IEEE*, pages 177–187.
- [Oden, 1972] Oden, J. (1972). *Finite Elements of Nonlinear Continua*. McGraw-Hill.
- [Østergaard, 2012] Østergaard, N. (2012). *On Lateral Buckling of Armouring Wires in Flexible Pipes*. PhD thesis, Aalborg University, Aalborg, Denmark. ISBN 87-91464-35-8.
- [Østergaard et al., 2011] Østergaard, N., Lyckeggard, A., and Andreasen, J. (2011). On lateral buckling failure of armour wires. In *Proc. of OMAE'2011 OMAE2011-49358*.
- [Passano et al., 2008] Passano, E., Gjøsteen, J., and Sævik, S. (2008). Onboard screening of forecast weather during installation. In *Proc. of OMAE'2008, ISBN: 0-7918-3821-8, Estoril, Portugal*.
- [PD6493, 1991] PD6493 (1991). Guidance on methods for assessing the acceptability of flaws in fusion welded structures. BS, UK.
- [Phifer et al., 1994] Phifer, E., Kopp, F., Swanson, R., Allen, D., and Langner, C. (1994). Design and installation of auger steel catenary risers. In *OTC-7620-MS, Offshore Technology Conference, Houston, Texas*.
- [Putot and Rigaud, 1990] Putot, C. and Rigaud, J. (1990). Upheaval buckling of buried pressurized pipelines. In *Proc. of European Seminar on Offshore Pipeline Technology, Paris, France*.
- [R.E.Hobbs, 1984] R.E.Hobbs (1984). In-service buckling of heated pipelines. *ASCE Journal of Transportation Engineering*, 110:175–189.
- [REINERTSEN, 2009] REINERTSEN (2009). Course in pipeline engineering.
- [Sævik, 1990] Sævik, S. (1990). Reliability based design against upheaval buckling. Project Work.
- [Sævik, 1992] Sævik, S. (1992). *On Stresses and Fatigue in Flexible Pipes*. PhD thesis, NTH, Trondheim, Norway.
- [Sævik, 1993] Sævik, S. (1993). A finite element model for predicting stresses and slip in flexible pipe armouring tendons. *Computers & Structures*, 46(2):219 – 230.

- [Sævik, 2008] Sævik, S. (2008). SIMLA - *Theory Manual*. MARINTEK, Trondheim, Norway.
- [Sævik, 2010] Sævik, S. (2010). BFLEX2010 - *Theory Manual*. MARINTEK, Trondheim, Norway.
- [Sævik, 2011] Sævik, S. (2011). Theoretical and experimental studies of stresses in flexible pipes. *Computers and Structures*, 89(2324):2273 – 2291.
- [Sævik et al., 1992a] Sævik, S., Berge, S., B.Skallerud, Eide, O., and Bech, A. (1992a). Fatigue test and analysis of a coflexip 4inch flexible pipe. Draft report Sintef Report STF71 F92xxx, SINTEF.
- [Sævik et al., 1992b] Sævik, S., Berge, S., Skallerud, B., Eide, O., and Olufsen, A. (1992b). Fatigue test and analysis of a 4inch flexible pipe. Final report Sintef Report STF71 F92192, SINTEF.
- [Sævik et al., 2004] Sævik, S., Giertsen, E., and Berntsen, V. (2004). Advances in design and installation analysis of pipelines in congested areas with rough seabed topography. In *Proc. of OMAE'2006, ISBN: 0-7918-4746-2, Hamburg, Germany*.
- [Sævik and Gjøsteen, 2010] Sævik, S. and Gjøsteen, J. (2010). USAP - *Theory Manual*. MARINTEK, Trondheim, Norway.
- [Sævik and Levold, 1995a] Sævik, S. and Levold, E. (1995a). High temperature snaking behaviour of pipelines. In *Proc. of ISOPE'95, ISBN: 1-880653-18-4, The Hague, Netherlands*, volume II, pages 63–71.
- [Sævik and Levold, 1995b] Sævik, S. and Levold, E. (1995b). High temperature snaking behaviour of pipelines. In *Proc. of OMAE'95, ISBN: 0-7918-1308-8, Copenhagen, Denmark*.
- [Sævik et al., 1990] Sævik, S., Søreide, T., and E.Levold (1990). PIPELINE ANALYSIS SYSTEM - PAS - *Theory Manual*. REINERTSEN Engineering, Trondheim, Norway.
- [Skallerud, 1991a] Skallerud, B. (1991a). Damping models and structural damping in a non-bonded pipe. Final report Sintef Report STF71 F91018, SINTEF.
- [Skallerud, 1991b] Skallerud, B. (1991b). Structural damping in a wellstream pipe. Final report Sintef Report STF71 F91059, SINTEF.
- [Søreide, 1973] Søreide, T. (1973). Collapse behaviour of stiffened plates using alternative finite element formulations. Technical Report Report No. 77-3, Norwegian Institute of Technology, Trondheim, Norway.
- [Søreide, 1985] Søreide, T. (1985). *Ultimate Load Analysis of Marine Structures*. Tapir, Trondheim, Norway.

- [Søreide, 1989] Søreide, T. (1989). Lecture notes on analysis of non-linear structures. Technical report, Norwegian Institute of Technology, Trondheim, Norway.
- [Sotberg et al., 1994] Sotberg, T., Holthe, K., Lund, K., and Igland, R. (1994). Pondus technical manual. Technical report, Marintek.
- [Sparks, 1984] Sparks, C. (1984). The influence of tension, pressure and weight on pipe and riser deformations and stresses. *J. of Energy Resources Technology*, 106.
- [Subsea7, 2013] Subsea7 (May 2013). Technology news from subsea 7 - may 2013.
- [Sumer and Fredsoe, 2006] Sumer, B. and Fredsoe, J. (2006). *Hydrodynamics around Cylindrical Structures*. World Scientific Publishing Company.
- [Tan et al., 2006] Tan, Z., Loper, C., Sheldrake, T., and Karabelas, G. (2006). Behavior of tensile wires in unbonded flexible pipe under compression and design optimization for prevention. In *Proc. of OMAE'2006*.
- [Thorsen, 2011] Thorsen, M. (2011). Capacity of deep water flexible risers. Master thesis, NTNU - Department of Marine Technology.
- [Timoshenko and Gere, 1963] Timoshenko, S. and Gere, J. (1963). *Theory of Elastic Stability*. McGraw-Hill.
- [Vaz and Rizzo, 2011] Vaz, M. and Rizzo, N. (2011). A finite element model for flexible armor wire instability. *Marine Structures*, (24):275–291.
- [Young and Budynas, 2002] Young, W. and Budynas, R. (2002). *Roark's Formulas for Stress and Strain*. McGraw-Hill.